THE FLOW OF A LIQUID JET IN A HOMOGENEOUS SUSPENSION

Thesis by

Christopher Vincent Chow

In Partial Fulfillment of the Requirements

for the Degree of

Doctor of Philosophy

California Institute of Technology

Pasadena, CA

1987

(submitted January 19, 1987)

ACKNOWLEDGEMENT

This thesis was written with tremendous assistance from several individuals to whom I would like to express my appreciation. Heading this group is Eric Herbolzheimer, whose support, guidance, and concern have left a lasting impression on me. As both my advisor and friend, he has made my graduate education an enriching and enjoyable experience. Next I would like to express my gratitude to Rita Mendelson for her relentless effort in preparing this manuscript. Key contributions were made to the experiments by George Griffith, who helped to design and construct the apparatus. Showing staunch support in my final drive, Howard Stone was a major help in preparing the figures and keeping me cool.

The years that I have spent at Cal Tech have been richly rewarded by the friends that I have made both inside and outside of school. Of these, none stands above Joe Leone, with whom one-on-one matches, softball and countless other events have provided me with memories that I will always cherish. Also, I thank Barry Bentley, Tony Geller, Jim Stoos, Hong-Man Chan, and Howard for their companionship and fun times in the basement of Spalding. Luckily for me, their presence made the working hours pass quickly. Lastly, my family has always been extremely important to me, and I would like to take this moment to thank my parents, Marie, Jim and Minda, Jan, Angela, and Greg for their unyielding love and support.

ABSTRACT

The theoretical and experimental work summarized in this thesis examine the flow of a vertical jet issuing into a suspension of particles. For small particle Reynolds numbers, a relative velocity (between the particle and the bulk suspension) that is a function of concentration only, and an initially homogeneous suspension, the flow field divides into regions of pure fluid and suspension, and hence, a buoyancy force is exerted on the lighter pure fluid jet. The governing two-phase flow equations are solved in different asymptotic limits to show that the jet acquires increasing plume-like characteristics as it flows downstream. A linear stability analysis on the plume-like flow solution showed that there is no critical flow parameter below which this flow is stable. The experimental work was conducted so that comparisons could be made with the theoretical predictions. The experimentally measured spreading rates of the pure fluid region agree quite well with those predicted by the theory, and verify the effect of the buoyancy force on the jet. As predicted by the stability analysis, all of the plume-like flows were unstable. Quantitative comparisons of the experimentally measured amplification rates with those predicted by the theory were inconclusive. However, the qualitative effects of buoyancy, initial jet momentum, and particle concentration in the suspension were observed to be destabilizing, as predicted by the theory.

Table of Contents

LIST OF ILLUSTRATIONS

List of Illustrations (continued)

LIST OF TABLES

CHAPTER 1

Introduction

Suspension flows are very common in industrial and natural processes. Flow in fluidized beds, sedimentation, and transport of slurries are but a few examples of flows with particulates dispersed in a fluid medium. These types of flows are generally more difficult to model than single phase flows, since the governing equations for the pure fluid are now coupled to the equations of motion for the particles through the concentration and velocity fields. Hence, in addition to the difficulties encountered in describing the flow of a single phase fluid, the analogous suspension problem is further complicated by the mathematically more difficult governing equations, as well as the addition of the particle velocity and concentration as unknowns.

The standard approach for solving suspension flow problems uses an averaged form of the Navier-Stokes equations that has removed the fluctutations in the pressure and velocity which occur over a length scale comparable to the particle size. This averaging process introduces terms into the equations which depend on the details of the flow around the particles, and for which constitutive equations must be formulated. There are many different averaging approaches, and disagreement still exists as to the correct form for these constitutive relations. However, once the governing equations are formulated, the problem is still difficult to solve because of the unknown concentration field that must be determined as part of the

solution. As a result of these complexities and confusion, there are few solutions to the governing equations for suspension flows. Furthermore, for those suspension flows which can be modeled by analytical solutions, the concentration field is homogeneous over much of the flow and can be relatively easily described.

One example of a suspension flow for which a solution has been found is the stability problem of the state of uniform fluidization. Jackson (1963) studied the unbounded flow, where the undisturbed state is represented by a uniform concentration field, constant fluid velocity, and zero particle velocity. The temporal growth of a small disturbance in the concentration results in planar, wave-forms of voidage which propagate both upward and downward from the point of origin. In solving the linearized disturbance equations, which were greatly simplified by the constant velocity of the base flow, he found that the flow is always unstable to small disturbances, and that the least stable disturbances have an unbounded growth rate as the wavelength decreases. Anderson and Jackson (1968) investigated the same problem for the case of a bounded flow in a fluidized bed. They found that all disturbances are unstable but that there is a distinct wavelength that has a maximum, but finite, growth rate. Hence as is the case for pure fluid flows, the effect of the walls is stabilizing.

Homsy, El-Kaissy, and Didwania (1980) studied this same flow to quantify a constitutive relation for the solid "phase". This required the evaluation of material constants from experimental data in order to describe characteristics of the flow instability (e.g., wave number, velocity of propagation, etc.). The same constants were then

used to predict these instability characteristics at different flow conditions, which in general, showed good agreement with the experimental results. Didwania and Homsy (1982) extended the analyses of instabilities in a fluidized bed still further, as they investigated the development of the planar wave disturbances into more complicated forms. Using the same constitutive relations as Homsy et al. (op. cit.), they examined the stability of the planar voidage waves, and estimated the horizontal wavenumbers of the secondary instabilities. They showed that these predicted values agreed well with those measured experimentally.

Acrivos and Herbolzheimer (1979) studied the flow of a suspension with significant spatial variations of the particle concentration in an examination of the "Boycott effect". They solved the equations governing the sedimentation of a suspension in an inclined channel, where the flow field divides into regions of pure fluid, and suspension at uniform concentrations. Hence, a buoyancy force is exerted on the pure fluid region by the heavier suspension. The unknown position of the interface, i.e., the boundary between the pure fluid and suspension regions, was determined as part of the solution. Herbolzheimer (1983) later examined the stability of the interface to small perturbations where he found that the critical Reynolds number increased for both narrower and more inclined (from the vertical position) channels. He was able to predict experimentally observed instabilities quite successfully.

In order to further assess the usefulness of the approach by Acrivos and Herbolzheimer, this work shall extend their analysis to the problem of a laminar liquid jet issuing vertically into a

suspension. Similar to the flow generated during sedimentation in an inclined channel, the flow field is expected to divide into regions of pure fluid and suspension, so that buoyancy effects are important. In addition, the position of the interface is unknown and must be determined in the solution. However, the jet is assumed to be far away from any walls so that the flow is essentially unbounded.

A motivation for this study is to understand the effect of particles on the flow of a pure fluid jet. The analogous single phase problem, i.e., a pure fluid jet issuing into an environment of the same fluid, was first investigated by Schlichting (1933) and independently, by Bickley (1937). They solved the governing boundary layer equations (with no pressure term), and found that the drag force exerted by the surrounding fluid caused the centerline velocity to decay with axial position like

$$u \sim x^{-1/3} .$$

Of course, in the two-phase flow problem, the heavier particles are expected to cause a buoyancy force to act on the pure fluid.

The analogous, single phase, free boundary layer flow where buoyancy is important is that of a plume rising above a line source of heat. In this case, the governing equations are difficult to solve because the temperature and velocity fields are coupled. However, assuming that the variation in temperature affects only the buoyancy force, i.e., the Boussinesq approximation, the equations can be simplified and solved through a similarity transformation. Fujii (1963) solved the Boussinesq equations at several Prandtl numbers and

found that the centerline velocity increased with axial distance like

$$u \sim x^{1/5} .$$

Savage and Chan (1970) examined mixed convection effects in the two-dimensional flow developed by a hot laminar jet issuing vertically into a uniform environment of a colder fluid. Based on physical arguments, they predicted that the flow field is represented by the pure fluid jet solution near the origin, and the pure fluid plume solution further downstream. Thus, they assumed a perturbation expansion of the governing equations of motion at small and large axial distances, x, where the leading order equations in these two regions were those for the jet and plume, respectively. However, the expansion parameters, i.e., $x^{4/3}$ and x^{-1}, diverge for large and small values of x, and in order to describe the entire flow field, a numerical patching procedure was required. Mollendorf and Gebhart (1973a) studied weak buoyancy effects in the flow of a round laminar vertical jet. They included the buoyancy term in the momentum equations at a higher order using an expansion paramater $\varepsilon \sim x^2$, and found that the axial velocity increased in the region of the thermal boundary layer. Hence, the qualitative effects of buoyancy on the laminar flow of a pure fluid jet are known.

There has been a significant amount of work (cf. List 1982) investigating the flow of turbulent buoyant jets and forced plumes, because of their importance in modelling environmental flow processes such as those encountered in ocean wastewater disposal or smoke from chimney stacks. These analyses follow the approach of

Morton, Taylor, and Turner (1956) who examined the flow of a turbulent plume in an environment of uniform density. They assumed that: i) the rate of entrainment of fluid into the jet is proportional to some characteristic velocity at the same height, and is specified in terms of an entrainment coefficient; ii) the cross sectional profiles of the velocity and buoyancy are similar at all heights; and iii) the density differences are significant in the buoyancy terms only. The equations of conservation of mass, momentum, and buoyancy flux were then integrated over a cross section of the jet to yield a set of ordinary differential equations. The solution of these equations gives general features of the jet (e.g., centerline velocity, jet width, and flow rate as functions of the axial distance.) However more detailed information such as the mean velocity profile, or the entrainment coefficient must be determined experimentally.

In experimental measurements made on turbulent buoyant jet flows, Kotsovinos (1975) found that the entrainment coefficient is not constant over the entire flow region. This is in accord with the results from studies made on turbulent plumes and jets, where these flows were both described reasonably well by theoretical models which used constant, but different, entrainment coefficients (cf. Ricou and Spalding (1961), and Mih and Hoopes (1972)). This question of entrainment has not been completely resolved, and a review of the different assumptions used for the entrainment function is given by Koh and Brooks (1975). Thus, an accurate description of the turbulent buoyant jet over the entire flow field is still unknown.

The goal of this thesis is to investigate the effect of the buoyancy force due to the suspension, on the flow of a laminar jet. In this theoretical and experimental study, we intend to characterize the different flow regions of the jet, and the experimental range of parameters where they are expected to occur. We shall begin this work in the next section by summarizing the equations governing a general suspension flow. In Chapter 2 the equations will then be simplified in appropriate asymptotic limits using scaling arguments, and solved using analytical techniques. The resulting asymptotic solutions describe different regions of the jet flow field, and it will be shown how these fit together in a sequence of flows.

In order to determine the conditions under which these flows are observed, their stability to small disturbances is investigated in Chapter 3. Using the wavelength of the disturbance as the expansion parameter, the linearized disturbance equations are solved analytically in an asymptotic limit that is consistent with that of the base flow solution. Finally, in Chapter 4, quantitative comparisons will be made of the experimentally measured interfacial spreading rates with those predicted by the base flow solutions in Chapter 2. In addition, the experimentally measured inception distances, (i.e., the distance from the nozzle where disturbances are first observed), will be compared to those predicted by the linear stability analysis.

1.1 Suspension Flow Governing Equations

The first step in studying suspension flows analytically is to develop a tractable set of equations and boundary conditions

governing the motion of both the fluid and the particles. Although the exact equations are known (i.e., the Navier-Stokes equations with no-slip boundary conditions at the surface of each particle together with Newton's equations of motion for each particle) and could in principle be solved completely, the large number of particles in any practical system and the complexity of the flow field around the particles makes such a detailed calculation impossible. An alternate approach is to discard the details of the motion on the scale of the particles and define flow variables averaged over a scale large compared with the particles but very small compared with that of the overall suspension. Then, by applying averaging techniques to the exact governing equations, we can obtain a set of equations governing these averaged flow variables (e.g. the fluid and particle velocities, the particle concentration, etc.) as functions of space and time. This approach is analogous to that used in studying turbulent flows of pure fluids, or even to that used in obtaining the Navier-Stokes equations where the motions of the individual molecules are averaged to yield a continuum description of the fluid. In the suspension problem, we average over a scale large compared with the particles instead of large compared with the molecules.

There are many different methods currently in use for obtaining the averaged governing equations and an extensive literature examining the subtleties of these approaches continues to flourish. It now seems safe to say that the basic governing equations are well established and that the principal difficulty is in determining constitutive relations for the suspension properties such as the stress in the suspension and the average force exerted on the

particles due to interactions with the fluid and with the other particles in the suspension. However, these equations can be recast in many different forms and for a given flow situation certain formulations are more convenient than others.

One approach, followed by Anderson and Jackson (1967), Homsy (1980), and others, is to write the momentum and continuity equations for both the particle and fluid "phases". Although in some cases, these equations are very simple, they require a constitutive relation for the stress in the fluid phase and another for that in the particle "phase". Unfortunately, these individual stresses can be neither determined theoretically nor measured experimentally, except by parameter estimation through an empirical fit of experimental data to theoretical predictions for rather complex flows (cf. Homsy op. cit.). The advantage of this approach is that acceleration of one phase relative to the other can be included with relative ease using simple models for the interphase force. However, if the particle Reynolds number, Re_p is small, the relative acceleration of the phases is negligible and it becomes easier to recast the individual phase momentum equations into one for the overall suspension and another for the motion of the particles relative to the suspension. Then the only constitutive relations we need are for the stress of the suspension, which can be measured in a viscometer, and for the interphase force, which can be determined from settling experiments.

In this thesis we shall restrict our attention to situations where the particle Reynolds number is low so let us now consider how the governing equations simplify in this case. We will restrict the discussion to suspensions of identical solid spheres in a Newtonian

incompressible fluid and assume that all non-hydrodynamic interaction between the particles and the fluid are negligible. We shall write these equations in terms of a bulk average velocity $\vec{u}^*$ and a relative velocity $\vec{u}_r^*$,

$$\vec{u}^* = c\vec{u}_p^* + (1-c)\vec{u}_f^* ,$$

and

$$\vec{u}_r^* = \vec{u}_p^* - \vec{u}^* ,$$

where c is the volume fraction of particles, the superscript * refers to dimensional quantities, and the subscripts p and f refer to the particle and fluid phases, respectively. The governing dimensional equations are

$$M_p \frac{D\vec{u}_p^*}{Dt^*} = V_p(\rho_p - \rho_f)g\vec{e} + \vec{F}_D , \tag{1.1a}$$

and

$$\frac{\partial c}{\partial t^*} + \vec{u}_p^* \cdot \nabla^* c = -c\nabla^* \cdot \vec{u}_r^* , \tag{1.1b}$$

for the particle phase, and

$$\rho^*(c)\frac{D\vec{u}^*}{Dt^*} + (\rho_p-\rho_f)c\left[\frac{D\vec{u}_r^*}{Dt^*} + \vec{u}_r^* \cdot \nabla\vec{u}^*\right] = -\nabla^* p^*$$

$$+ \nabla^* \cdot \mu^*(c)\left[\nabla^*\vec{u}^* + (\nabla^*\vec{u}^*)^T\right] + \rho^*(c)g\vec{e} \ , \tag{1.2a}$$

and

$$\nabla^* \cdot \vec{u}^* = 0 \ , \tag{1.2b}$$

for the overall suspension. In (1.1a), M_p and V_p refer to the particle mass and volume, respectively, $\vec{F}_D$ is the interphase force, p^* is the dimensional pressure and $\vec{e}$ is the unit vector in the direction of gravity. In the overall suspension equation, $\rho^*(c)$ is the volume averaged density of the suspension

$$\rho^*(c) = c\rho_p + (1-c)\rho_f \ , \tag{1.3}$$

and the suspension has been assumed to behave as a Newtonian fluid with an effective shear viscosity, $\mu^*(c)$, that is a function of concentration only. Measurements of the stress under both steady and transient conditions have shown this assumption is reasonable for volume fractions up to about 0.30 (Gadala-Maria, and Acrivos (1980)).

Dimensional analysis shows that for spherical particles settling in a quiescent fluid under low Reynolds number conditions, the interphase force is given by the Stokes drag times a function of the local concentration; i.e.,

$$F_D = \frac{6\pi\mu_f a}{f(c)} \vec{u}_r^*$$

where a is the radius of the particles. Although Lynch (1985) has shown that when the suspension is undergoing bulk shearing motion the interphase force may also be a function of the local shear rate (and possibly shear type) of the suspension, we shall follow previous investigators and neglect this shear dependence. Then, assuming the particle Reynolds number is small, we can drop the particle acceleration term in (1.1a) to find that

$$\vec{u}_r^* = u_o f(c)\vec{e} \ , \tag{1.4}$$

where u_o is the Stokes settling velocity of the particles which is equal to $\frac{2}{9}a^2(\rho_p-\rho_f)g/\mu_f$. Thus, due to the assumption that the particle Reynolds number is small and that the dependence of the interphase force on the shear is negligible, the particle momentum equation reduces to the simple result that the relative velocity between the particles and the suspension is a function of the local concentration only. Note that f(c) is determined easily by measuring the sedimentation velocity in a quiescent suspension.

Substituting the expression for the relative velocity (1.4) into the particle continuity equation (1.1b) gives

$$\frac{\partial c}{\partial t^*} + \vec{u}_p^* \cdot \nabla^* c = - u_o c \frac{\partial f}{\partial c} \vec{e} \cdot \nabla^* c \ . \tag{1.5}$$

Hence, if the concentration is initially uniform at $c = c_o$ and/or uniform at the flow inlet, it will remain at this value along particle streamlines (cf., Acrivos and Herbolzheimer 1979). Thus we can divide the flow domain into regions of pure fluid, regions of suspension at concentration c_o, and regions of accumulated sediment near the upward-facing surfaces of the vessel containing the suspension. Hence provided the sediment regions are not important, the only unknown in the concentration field is the position of the interface separating the pure fluid and suspension regions.

Now the particle momentum and continuity equations are replaced by $u_r^* = u_o f(c)\vec{e}$, and $c = 0$ or c_o, and the overall suspension equations are written in the dimensionless form,

$$\rho(c)\,\frac{D\vec{u}}{Dt} + \frac{u_o}{u_c}\left(\frac{\rho_p}{\rho_f} - 1\right)c\left[\frac{D}{Dt}f(c)\vec{e} + f(c)\vec{e}\cdot\nabla\vec{u}\right] = -\nabla p$$

$$+ Gr\left(\frac{c}{c_o} - 1\right)\vec{e} + \frac{\mu(c)}{Re}\nabla^2\vec{u}\,, \tag{1.6a}$$

and

$$\nabla\cdot\vec{u} = 0\,, \tag{1.6b}$$

where the velocity, length, time, and pressure have been made dimensionless by dividing by, u_c, L_c, L_c/u_c, and $\rho_f u_c^2$, respectively, so that the Reynolds number is defined by

$$Re = \frac{\rho_f u_c L_c}{\mu_f} \quad . \tag{1.7}$$

Furthermore, the Grashof number, defined by

$$Gr = \frac{(\rho_p - \rho_f) c_o g L_c}{\rho_f u_c^2} \tag{1.8}$$

is a relative measure of the gravitational force to the inertial forces in the suspension. We define the dimensionless variables $\rho(c)$ and $\mu(c)$ as the suspension density and viscosity, divided by their respective pure fluid quantities. In addition, the pressure term in (1.6a) has been redefined by subtracting off the hydrostatic pressure of a suspension at concentration $c = c_o$

$$\rho_f u_c^2 \nabla p = \nabla p^* - \rho(c_o) g \vec{e} \quad . \tag{1.9}$$

Consequently, the body force term appears as an effective buoyancy force with regions with $c < c_o$ tending to rise, and those with $c > c_o$ tending to sink.

Of course, these equations must be supplemented with boundary conditions at the suspension-pure fluid interface. Using the notation that $[\ ]_j$ denotes the jump of a quantity across this interface, the boundary conditions are continuity of velocity,

$$[\vec{u}]_j = 0 \ , \tag{1.10a}$$

continuity of stress,

$$[\underline{\sigma} \cdot \vec{n}]_j = 0 \ , \qquad (1.10b)$$

and the kinematic condition,

$$\frac{\partial I}{\partial t} + \vec{u}_p \cdot \nabla(I-y) = 0 \qquad \text{at} \quad y = I(x,z,t) \ , \qquad (1.10c)$$

where $y = I(x,z,t)$ is the equation for the position of the interface.

Equations (1.6) - (1.10) summarize the problem which essentially is now reduced to single phase flow of two adjacent fluids of different density and viscosity. At the interface position, which must be determined as part of the solution, there is a possible exchange of fluid, but there are no surface tension effects. Note that in the dilute limit, $\mu(c) = \rho(c) = 1$, and the only effect of the presence of the particles is in the buoyancy term. This is essentially the Boussinesq approximation. In this case, however, instead of solving a coupled transport problem for the temperature field, we need only find the position of the interface separating the suspension and pure fluid regions.

CHAPTER 2

The Steady Flow of a Vertical Two-dimensional Jet of Liquid into a Homogeneous Suspension

2.1 Introduction

Let us now consider the solution of the equations developed in the last chapter for the steady flow of a two-dimensional jet of liquid issuing vertically into an unbounded, homogeneous suspension consisting of the same liquid as in the jet but with spherical particles dispersed throughout it. As shown in Figure 1, the jet issues from a slit of width $2b_o^*$ with an initial momentum given by

$$M_o = 2\rho_f \int_0^{b_o^*} [u^*(0,y^*)]^2 \, dy^* \equiv 2\beta\rho_f u_j^2 b_o^* \, , \tag{2.1a}$$

where $u^*(x^*,y^*)$ is the dimensional velocity in the x-direction, and

$$u_j = \frac{1}{b_o^*} \int_0^{b_o^*} u^*(0,y^*) \, dy^* \, , \tag{2.1b}$$

is the average velocity of the fluid as it leaves the nozzle. The O(1) constant β accounts for the fact that the velocity profile at the nozzle may not be uniform. A particle-free region forms and is separated from the suspension by interfaces located at $y^* = \pm b^*(x)$. As the fluid in this region rises, it drives a flow in the adjoining

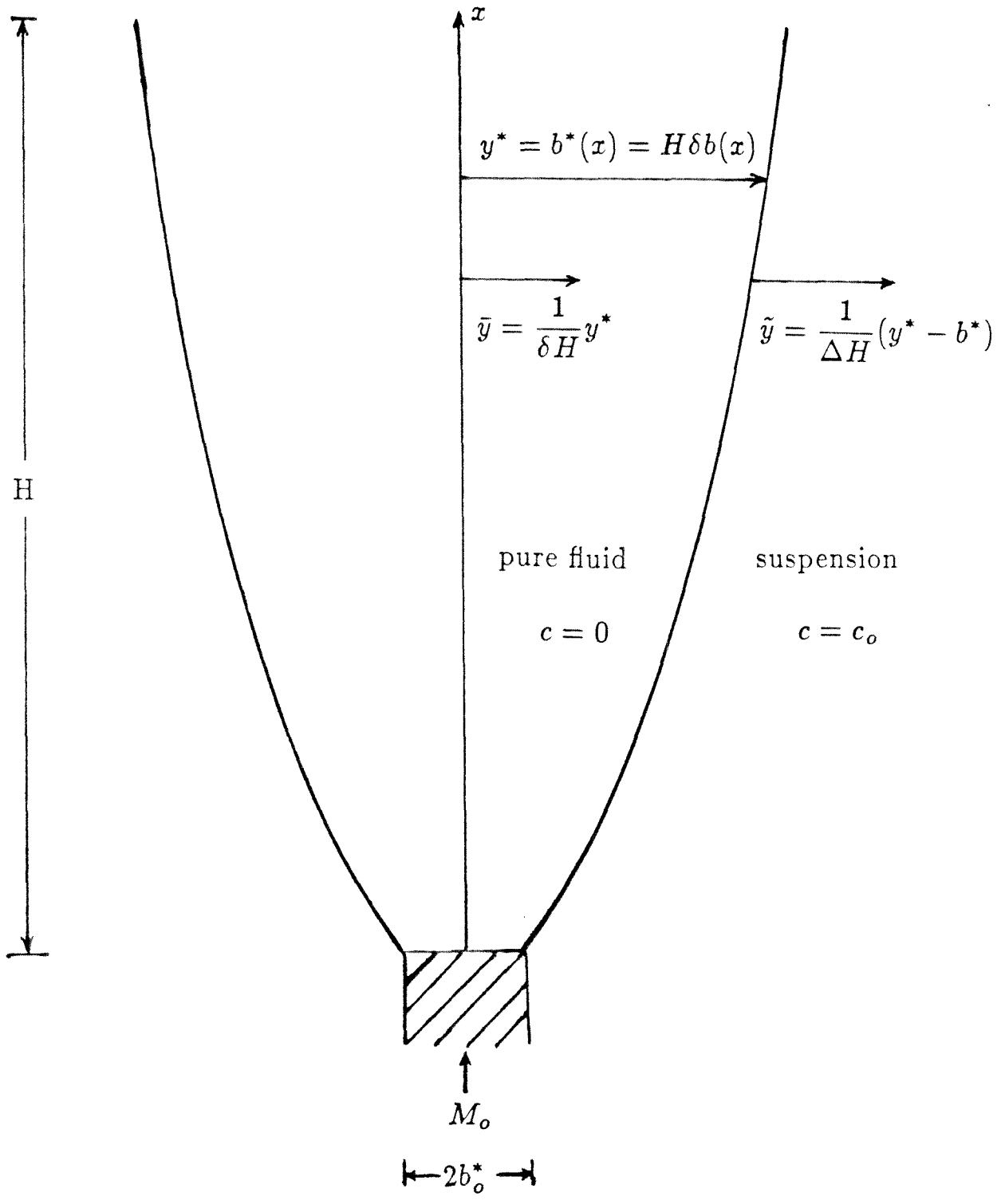

Figure 1 The jet flow region and definition of coordinate variables.

suspension by applying a shear stress at the interface between these regions. This shear stress tends to decelerate the pure fluid region. However, this effect is counterbalanced by buoyancy, which tends to accelerate the pure fluid since it is less dense than the suspension. As we shall see below, only a negligible amount of fluid crosses the interface between the pure fluid and suspension regions so continuity requires the width of the pure fluid region to vary inversely with the average velocity in this region. Hence, when buoyancy effects are negligible (corresponding to a pure fluid jet) this region becomes wider with increasing distance from the nozzle, while when buoyancy effects are important (corresponding to a plume) this region becomes narrower.

To determine quantitatively the role buoyancy plays in the mechanics of this flow, we shall solve the equations derived in Chapter 1 in the limits of large Reynolds and/or Grashof numbers. In using these equations, we are assuming that: i) the suspension is composed of identical spherical particles suspended in a Newtonian fluid; ii) all non-hydrodynamic interactions between the particles are negligible; and iii) the particle Reynolds number is small. We shall begin by presenting the mathematical formulation of the problem. Next, scaling arguments are applied to determine the flow structure in the important asymptotic limits. Finally, detailed solutions are obtained for each of the important regimes.

2.2 Mathematical Formulation

Let us now assume that the concentration in the suspension is initially uniform and equal to c_o and that the governing equations obtained in Chapter 1 apply. In the limit of large Reynolds and/or Grashof numbers we expect a boundary-layer type flow to develop, i.e., we expect the region of flow to become slender. We shall define a coordinate system which has the origin located at the center of the slit of the nozzle tip with x and u as the axial coordinate and velocity respectively, and y and v as the corresponding transverse coordinate and velocity. Hence, letting ρ_o and μ_o denote the normalized suspension density and viscosity, respectively, the dimensionless two-dimensional flow equations become,

in the pure fluid region

$$\frac{\partial u}{\partial x} + \frac{\partial \bar{v}}{\partial \bar{y}} = 0 \ , \tag{2.2a}$$

$$u\frac{\partial u}{\partial x} + \bar{v}\frac{\partial u}{\partial \bar{y}} = -\frac{\partial p}{\partial x} + \frac{Gr_j}{b_o}\left(\frac{u_j}{u_c}\right)^2 + \frac{u_j b_o}{u_c \delta^2 Re_j}\frac{\partial^2 u}{\partial \bar{y}^2} + O\left(\frac{\delta^2}{Re}\right) \ , \tag{2.2b}$$

$$\frac{\partial p}{\partial \bar{y}} \sim O\left(\delta^2 \ , \ \frac{\delta^2}{Re}\right) \ , \tag{2.2c}$$

and in the suspension region

$$\frac{\partial u^s}{\partial x} + \frac{\partial \bar{v}^s}{\partial \bar{y}} - \frac{\delta}{\Delta}\frac{db}{dx}\frac{\partial u^s}{\partial \bar{y}} = 0 \ , \tag{2.3a}$$

$$u^S\frac{\partial u^S}{\partial x} + (\bar{v}^S - \frac{\delta}{\Delta}\frac{db}{dx}u^S)\frac{\partial u^S}{\partial \tilde{y}} = -\frac{1}{\rho_o}\frac{\partial p^S}{\partial x} + \frac{u_j b_o}{u_c \Delta^2 Re_j}\nu_o\frac{\partial^2 u^S}{\partial \tilde{y}^2}$$

$$+ O(\frac{\Delta^2}{Re}, \frac{u_o}{u_c}) , \tag{2.3b}$$

$$\frac{\partial p^S}{\partial \tilde{y}} \sim O(\Delta^2 , \frac{\Delta^2}{Re}) , \tag{2.3c}$$

where the characteristic length is given by the jet penetration length H, the characteristic velocity is given by u_c (which will be specified shortly), u_j is the average jet velocity defined in (2.1) and b_o is the dimensionless slit width. Because there is no physical length scale in the axial direction, the definition of the jet penetration length H is somewhat arbitrary. We shall see that the asymptotic limits of the various solutions depend on the dimensionless slit width $b_o = b_o^*/H$, and this is interpreted as the inverse dimensionless characteristic distance from the nozzle in any flow region of interest. The stretched transverse coordinate and velocity variables are defined by

$$\bar{y} = \frac{y}{\delta} , \qquad \bar{v} = \frac{v}{\delta} , \tag{2.4a}$$

and

$$\tilde{y} = \frac{1}{\Delta}(y - \delta b(x)) , \quad \bar{v}^S = \frac{v^S}{\Delta} , \tag{2.4b}$$

for the pure fluid and suspension respectively. Here $\bar{y} = b(x) = b^*(x)/\delta H$ is the rescaled equation for the interface position, and the

scalings δ and Δ refer to the respective thicknesses of the pure fluid and suspension flow regions (cf. Figure 1). The Reynolds and Grashof numbers defined in (1.7) and (1.8) have been rescaled to give Re_j and Gr_j since these latter dimensionless groups are specified by the known parameters at the nozzle, i.e.,

$$Re_j = \frac{\rho_f u_j b_o^*}{\mu_f} = \frac{u_j}{u_c} b_o Re \ , \tag{2.5}$$

and

$$Gr_j = \frac{(\rho_p - \rho_f) c_o g b_o^*}{\rho_f u_j^2} = \frac{Gr}{b_o} \left(\frac{u_c}{u_j}\right)^2 . \tag{2.6}$$

The boundary conditions are:

i) symmetry of the flow about the centerline

$$\bar{v} = \frac{\partial u}{\partial \bar{y}} = 0 \qquad \text{at } \bar{y} = 0 \ ; \tag{2.7a}$$

ii) continuity of velocity and stress at the interface, i.e., at $\tilde{y} = 0$

$$\frac{\delta}{\Delta} \bar{v} = \bar{v}^s \ , \tag{2.7b}$$

$$u = u^s \ , \tag{2.7c}$$

$$\frac{\Delta}{\delta} \frac{\partial u}{\partial \bar{y}} = \mu_o \frac{\partial u^s}{\partial \tilde{y}} \ , \tag{2.7d}$$

$$p = p^s \ ; \tag{2.7e}$$

iii) decay of the velocity far from the jet

$$u^s \to 0 \quad \text{as} \quad \tilde{y} \to \infty \ ; \tag{2.7f}$$

and iv) the volumetric constraint

$$\int_0^b u \, d\bar{y} = \frac{b_o u_j}{\delta u_c} \ . \tag{2.7g}$$

The last condition implies that the volumetric flow rate of the pure fluid is constant at any cross section downstream from the nozzle. This can be shown by integrating the continuity equation in the pure fluid (2.2a) and applying the first symmetry condition in (2.7a) to determine the transverse velocity at the interface

$$\bar{v} = - \frac{d}{dx} \int_0^b u \, d\bar{y} + \frac{db}{dx} u \qquad \text{at } \tilde{y} = 0.$$

Substituting in the steady form of the kinematic condition, i.e.,

$$\bar{v} = \frac{db}{dx} u_p = \frac{db}{dx} \left(u - \frac{u_o}{u_c} f\right) \qquad \text{at } \tilde{y} = 0 \ ,$$

gives the rate of change of the volumetric flow rate with respect to axial distance,

$$\frac{d}{dx}\int_0^b u\, d\bar{y} = \frac{u_o}{u_c}\frac{db}{dx} f(c) .$$

Hence provided the sedimentation velocity is small compared with the characteristic convection velocity, the amount of fluid crossing the interface is negligible. The final boundary condition that we need is the velocity profile of the fluid as it exits the nozzle. Except in the entry region very close to the nozzle, the details of this profile are unimportant and the only feature we must retain is the initial momentum of the jet. Hence, outside of the entry region, the initial condition is replaced by the macroscopic momentum balance

$$\int_0^b u^2\, d\bar{y} + \frac{\Delta}{\delta}\rho_o \int_0^\infty (u^s)^2\, d\bar{y} = \frac{Gr_j}{b_o}\left(\frac{u_j}{u_c}\right)^2 \int_0^x b(\xi)\, d\xi + \frac{M_o}{2\delta H \rho_f u_c^2} . \quad (2.7h)$$

We further see that when H is large (i.e., at large distances from the nozzle) the initial momentum of the jet is negligible in the momentum balance, and hence all details of the original velocity profile are unimportant. In this case the velocity is large compared with the jet velocity and the condition in (2.7h) is not needed.

2.3 General Scaling Results

The equations and boundary conditions will be solved in detail for different asymptotic limits of the dimensionless groups Gr_j, Re_j and b_o in Section 6. Before doing this, however, we can obtain many important features of the flow by applying simple scaling arguments.

Let us begin by developing a few general scaling results which apply to all of the solutions.

Since the scaled volumetric flow rate in (2.7g) must be an O(1) quantity we can pick the characteristic velocity such that

$$\int_0^b u \, d\bar{y} = 1 \, . \tag{2.8}$$

With this choice we have

$$u_c = u_j b_o/\delta \, . \tag{2.9}$$

Next, the flow in the suspension region is of the boundary layer type being driven by the motion of the pure fluid region. We see from (2.3b) that to retain the viscous terms, the suspension boundary layer thickness must scale as $\Delta \sim (\frac{u_j b_o}{u_c Re_j})^{1/2}$. Using (2.9) this simplifies to

$$\Delta = (\frac{\delta}{Re_j})^{1/2} \tag{2.10}$$

which, of course, must be much less than O(1) if the boundary layer assumption is valid. We see then from the suspension y-momentum equation that the pressure change across the boundary layer is $O(\delta/Re_j)$ and hence the pressure derivative in the x-direction is given by that far away from the flow region. In this outer region the

flow is effectively inviscid and driven by the $O(\Delta)$ entrainment into the boundary layer. Hence, the pressure in this region is $O(\Delta^2)$. Thus the x derivative of the pressure is $O(\delta/Re_j)$ everywhere and may be neglected in equations (2.2b) and (2.3b).

All of the equations and boundary conditions may now be written in terms of δ, the thickness of the pure fluid region, which is the one remaining unknown scaling. We obtain,

$$u \frac{\partial u}{\partial x} + \bar{v} \frac{\partial u}{\partial \bar{y}} = Gr_j \frac{\delta^2}{b_o^3} + \frac{1}{\delta Re_j} \frac{\partial^2 u}{\partial \bar{y}^2} + O\left(\frac{\delta}{Re_j}, \delta^2\right), \qquad (2.11a)$$

$$\frac{\partial u}{\partial x} + \frac{\partial \bar{v}}{\partial \bar{y}} = 0, \qquad (2.11b)$$

$$u^s \frac{\partial u^s}{\partial x} + \left(\bar{v}^s - \frac{\delta}{\Delta} \frac{db}{dx} u^s\right) \frac{\partial u^s}{\partial \bar{y}} = \nu_o \frac{\partial^2 u^s}{\partial \bar{y}^2} + O\left(\frac{\delta}{Re_j}\right), \qquad (2.12a)$$

$$\frac{\partial u^s}{\partial x} + \frac{\partial \bar{v}^s}{\partial \bar{y}} - (\delta Re_j)^{1/2} \frac{db}{dx} \frac{\partial u^s}{\partial \bar{y}} = 0, \qquad (2.12b)$$

with the boundary conditions

$$\bar{v} = \frac{\partial u}{\partial \bar{y}} = 0 \qquad \text{at } \bar{y} = 0, \qquad (2.13a)$$

$$(\delta Re_j)^{1/2} \bar{v} = \bar{v}^s \qquad \text{at } \bar{y} = 0, \qquad (2.13b)$$

$$u = u^s \qquad \text{at } \bar{y} = 0, \qquad (2.13c)$$

$$\frac{\partial u}{\partial \bar{y}} = \frac{\delta}{\Delta}\,\mu_o \frac{\partial u^s}{\partial \tilde{y}} \qquad \text{at } \tilde{y} = 0\ , \qquad (2.13d)$$

$$u^s \to 0 \qquad \text{as } \tilde{y} \to \infty\ , \qquad (2.13e)$$

$$\int_0^b u\, d\bar{y} = 1\ , \qquad (2.13f)$$

$$\int_0^b u^2\, d\bar{y} + (\delta Re_j)^{-1/2}\,\rho_o \int_0^\infty (u^s)^2\, d\tilde{y} = Gr_j \frac{\delta^2}{b_o^3} \int_0^x b(\xi)\, d\xi + \beta \frac{\delta}{b_o}\ . \qquad (2.13g)$$

The size of δ is determined from the leading order balance in the pure fluid equation provided that all of these terms are scaled correctly. However, in the limit of a large buoyancy force, the pure fluid is accelerated, and its thickness δ decreases to a value much less than that of the boundary layer in the suspension. For $\delta << \Delta$, the tangential stress condition (2.13d) requires $\frac{\partial u}{\partial \bar{y}} << 1$, which implies that the derivative $\frac{du^*}{dy^*}$ is scaled incorrectly. In this case, the change in the velocity across the thin pure fluid layer is small compared to the characteristic velocity and for scaling purposes, we redefine

$$\frac{\partial u}{\partial \bar{y}} = \frac{\delta}{\Delta}\,\frac{\overline{\partial u}}{\partial \bar{y}} \qquad (2.14)$$

where the overbar now indicates an O(1) quantity. While this result

was derived for the case where $\delta << \Delta$, it can be trivially seen to hold for the case where $\delta \sim \Delta$ as well. With (2.14), equation (2.11a) becomes

$$u\frac{\partial u}{\partial x} + (\delta Re_j)^{1/2}\, \bar{v}\frac{\overline{\partial u}}{\partial \bar{y}} = Gr_j\, \frac{\delta^2}{b_o^3} + (\delta Re_j)^{-1/2}\, \frac{\overline{\partial^2 u}}{\partial \bar{y}^2} \qquad (2.15)$$

where this equation applies for $\delta \leq \Delta$. In those flows where $\delta >> \Delta$, the boundary layer has not grown to a width comparable to that of the pure fluid region. Hence this case corresponds to the entry flow near the nozzle which has an inviscid core in the pure fluid region with thin boundary layers at the pure fluid/suspension interface. The specific scaling results for the fully developed and entry length flows will be discussed in the next section.

2.4 Scaling Results for the Various Asymptotic Limits

2.4a Fully Developed Flows

Let us first consider the fully-developed flows which occur at some distance from the nozzle. As shown in the previous section, for these flows the thickness of the pure fluid region is smaller than or comparable to that of the boundary layer in the suspension so from (2.10) we know that

$$\frac{\delta}{\Delta} = (\delta Re_j)^{1/2} \leq O(1) \ .$$

Hence from (2.15), we see that the viscous terms must be retained in

the leading order balance in the pure fluid momentum equation. There are then three possible cases: i) the buoyancy and viscous terms are large and in balance; ii) the buoyancy, viscous, and momentum terms are all of comparable magnitude; and iii) the buoyancy term is small and the viscous and momentum terms balance. Let us consider the appropriate scalings and the range of validity for each of these possibilities.

Case I: Large Buoyancy

In this case, the buoyancy and viscous terms are large and of comparable magnitude. From (2.15) we see that the balancing of these terms requires

$$Gr_j \frac{\delta^2}{b_o^3} = (\delta Re_j)^{-1/2} >> 1 \ . \tag{2.16}$$

Solving for δ and then using (2.9) and (2.10) to obtain u_c and Δ we find that

$$\delta = (b_o^6/Gr_j^2 Re_j)^{1/5} \ , \tag{2.17a}$$

$$\Delta = (b_o^3/Gr_j Re_j^3)^{1/5} \ , \tag{2.17b}$$

and

$$u_c = u_j \ (Gr_j^2 Re_j/b_o)^{1/5} \ . \tag{2.17c}$$

Furthermore, in order for the momentum terms to be neglible we must

have that $(\delta Re_j)^{1/2} = \frac{\delta}{\Delta} << 1$, which from (2.17a) requires

$$\frac{1}{b_o} >> (Re_j^2/Gr_j)^{1/3} . \tag{2.18a}$$

Finally, for the boundary layer analysis to hold at all, Δ must be much smaller than O(1) which requires that

$$\frac{1}{b_o} >> (Gr_j Re_j^3)^{-1/3} . \tag{2.18b}$$

Note that since b_o is the slit width divided by H, the jet penetration distance, these conditions are always satisifed at sufficiently large distances from the nozzle.

With these scalings, the pure fluid momentum equation (2.11a) becomes

$$\frac{\partial^2 u}{\partial \bar{y}^2} = - \varepsilon + \varepsilon^2 (u\frac{\partial u}{\partial x} + \bar{v}\frac{\partial u}{\partial \bar{y}}) + O(\delta^2) \tag{2.19}$$

where

$$\varepsilon = (\frac{\delta}{\Delta}) = \left[\frac{b_o^3 Re_j^2}{Gr_j}\right]^{1/5} << 1 . \tag{2.20}$$

Hence to leading order the velocity in the pure fluid region is a function of x only.

Case II: Moderate Buoyancy

In this case all three terms in the pure fluid momentum equation are O(1), and the scalings are given by

$$\delta = \Delta = \frac{1}{Re_j} , \tag{2.21a}$$

$$u_c = u_j b_o Re_j . \tag{2.21b}$$

In order for the buoyancy term to be O(1), we must have

$$\frac{1}{b_o} \sim (Re_j^2/Gr_j)^{1/3} , \tag{2.22a}$$

while the condition that $\Delta << 1$ requires

$$Re_j >> 1 . \tag{2.22b}$$

Since the scalings for the widths of the pure fluid and suspension regions are identical, the momentum equation for the pure fluid region can be written in terms of $\tilde{y}$, the transverse coordinate in the suspension to give

$$u\frac{\partial u}{\partial x} + (\bar{v} - \frac{db}{dx} u) \frac{\partial u}{\partial \tilde{y}} = 1 + \frac{\partial^2 u}{\partial \tilde{y}^2} , \tag{2.23}$$

which is the boundary layer equation with no pressure gradient but with an additional constant buoyancy term.

Case III: Negligible Buoyancy

If the buoyancy term is small the scalings in (2.21) still apply, but the flow occurs in the different asymptotic limit

$$\frac{1}{b_o} << (Re_j^2/Gr_j)^{1/3} . \tag{2.24}$$

Hence this case applies closer to the nozzle than the previous cases (cf. 2.18a, and 2.22a). In this limit, the governing equation in the pure fluid region reduces to that for a pure fluid jet

$$u\frac{\partial u}{\partial x} + \bar{v}\frac{\partial u}{\partial \bar{y}} = \frac{\partial^2 u}{\partial \bar{y}^2} . \tag{2.25}$$

2.4b. Entry Region Flows

The scalings derived in the last subsection apply far enough from the nozzle that the flow has had sufficient time for the viscous effects to change the velocity profile leaving the nozzle into a "fully-developed" profile satisfying the appropriate boundary layer equations. Closer to the nozzle are entry flow regions in which the rearrangement of the velocity profile takes place. In this entry region the flow is characterized by an inviscid core of pure fluid with thin boundary layers on both sides of the interfaces. The scalings of both the suspension and pure fluid boundary layers must be the same, $O(\Delta)$, in order to satisfy the shear stress condition at the interface. The thickness of these boundary layers increases with distance from the nozzle until at some point it becomes comparable to the width of the inviscid core region. The distance to this point

is represented by the dimensionless distance $\ell = \ell^*/H$ and is a measure of the length of the entry region. Let us now consider the possible entry flow regimes and the corresponding scalings for ℓ.

In contrast with the flows in Cases I - III, the characteristic length in the x direction is small, (i.e., $O(\ell) << 1$), and the equations in (2.11) and (2.12) must be rescaled to give the appropriate equations in each of three regions:

in the core region

$$u\frac{\partial u}{\partial \bar{x}} + \left(\frac{\ell}{\delta Re_j}\right)^{1/2} \bar{v}\frac{\partial \bar{u}}{\partial \bar{y}} = Gr_j \frac{\delta^2 \ell}{b_o^3} + \left(\frac{\ell}{\delta Re_j}\right)^{3/2} \frac{\partial^2 \bar{u}}{\partial \bar{y}^2} + O\left(\frac{\delta \ell}{Re_j}, \delta^2 \ell^2\right), \quad (2.26a)$$

$$\frac{\partial u}{\partial x} + \frac{\partial \bar{v}}{\partial \bar{y}} = 0 ; \quad (2.26b)$$

in the pure fluid boundary layer region

$$\tilde{u}\frac{\partial \tilde{u}}{\partial \bar{x}} + \left[\tilde{v} - (\delta \ell Re_j)^{1/2} \frac{db}{dx} \tilde{u}\right] \frac{\partial \tilde{u}}{\partial \tilde{y}} = Gr_j \frac{\delta^2 \ell}{b_o^3} + \frac{\partial^2 \tilde{u}}{\partial \tilde{y}^2} + O\left(\frac{\delta \ell}{Re_j}\right), \quad (2.27a)$$

$$\frac{\partial \tilde{u}}{\partial \bar{x}} + \frac{\partial \tilde{v}}{\partial \tilde{y}} - (\delta \ell Re_j)^{1/2} \frac{db}{dx} \frac{\partial \tilde{u}}{\partial \tilde{y}} = 0 ; \quad (2.27b)$$

and in the suspension boundary layer region

$$u^S\frac{\partial u^S}{\partial \bar{x}} + \left[\tilde{v}^S - (\delta \ell Re_j)^{1/2}\frac{db}{dx}u^S\right]\frac{\partial u^S}{\partial \tilde{y}} = \nu_o\frac{\partial^2 u^S}{\partial \tilde{y}^2} + O(\frac{\delta \ell}{Re_j}) , \qquad (2.28a)$$

$$\frac{\partial u^S}{\partial \bar{x}} + \frac{\partial \tilde{v}^S}{\partial \tilde{y}} - (\delta \ell Re_j)^{1/2}\frac{db}{dx}\frac{\partial u^S}{\partial \tilde{y}} = 0 . \qquad (2.28b)$$

Note that we have used the new rescaled variables

$$\bar{x} = \frac{x}{\ell} ,$$

$$\bar{v} = (\ell/\delta)v = \frac{\Delta}{\delta}\tilde{v} = \frac{\Delta}{\delta}\tilde{v}^S , \qquad (2.29)$$

and

$$\frac{\partial u}{\partial \bar{y}} = \frac{\Delta}{\delta}\frac{\widetilde{\partial u}}{\partial \bar{y}} ,$$

where $\Delta \sim (\delta \ell/Re_j)^{1/2}$, and $\tilde{u}(\bar{x},\tilde{y})$ and $\tilde{v}(\bar{x},\tilde{y})$ correspond to the axial and transverse velocities in the pure fluid boundary layer.

The boundary conditions are essentially the same as those for the fully developed cases, but with additional matching conditions of both velocities between the pure fluid core and boundary layer regions. Also, the momentum balance (2.13g) must be replaced by the initial condition, i.e., matching the velocity profile with that of the fluid exiting the nozzle. The boundary conditions are then given by

$$\bar{v} = \frac{\partial u}{\partial \bar{y}} = 0 \qquad \text{at } \bar{y} = 0 , \qquad (2.30a)$$

$$\tilde{v} = (\delta Re_j/\ell)^{1/2}\, \bar{v} \qquad \text{as } \tilde{y} \to -\infty\ , \tag{2.30b}$$

$$\tilde{u} = u \qquad \text{as } \tilde{y} \to -\infty\ , \tag{2.30c}$$

$$\tilde{v} = \bar{v}^S \qquad \text{at } \tilde{y} = 0\ , \tag{2.30d}$$

$$\tilde{u} = u^S \qquad \text{at } \tilde{y} = 0\ , \tag{2.30e}$$

$$\frac{\partial \tilde{u}}{\partial \tilde{y}} = \mu_o \frac{\partial u^S}{\partial \bar{y}} \qquad \text{at } \tilde{y} = 0\ , \tag{2.30f}$$

$$u^S \to 0 \qquad \text{as } \tilde{y} \to \infty\ , \tag{2.30g}$$

$$\int_0^b u\, d\bar{y} = 1\ , \tag{2.30h}$$

and

$$u = u_i(\bar{y}) \qquad \text{at } x = 0\ , \tag{2.30i}$$

where $u_i(\bar{y})$ is the the non-dimensional initial velocity profile. For small ℓ, (2.26a) shows that to leading order the flow in the core region is inviscid but possibly accelerated by buoyancy. Hence applying the initial condition (2.30i) we find that

$$u = \frac{\delta}{b_o} \sqrt{2Gr_j \frac{\ell}{b_o}\, \bar{x} + u_i^2(\bar{y})}\ . \tag{2.31}$$

Thus depending on the size of the jet Grashof number, the fluid will

either accelerate with increasing x, or flow unchanged from its initial velocity profile. Meanwhile the boundary layer thickness increases with x until it is comparable in size to the core width. The point where the boundary layers merge defines the entry length.

Cases IVa and b: Large or Moderate Buoyancy

We see from (2.31 that for the asymptotic limit where buoyancy effects are important

$$Gr_j \geq b_o/\ell \ . \tag{2.32}$$

In order for the scaled velocity in (2.31) to be O(1), the pure fluid thickness must scale as

$$\delta \sim \left(\frac{b_o^3}{Gr_j \ell}\right)^{1/2} . \tag{2.33}$$

Hence in the limit

$$Gr_j >> \frac{b_o}{\ell} \ , \tag{2.34a}$$

i.e., that of Case IVa, the jet is quickly accelerated as it exits the nozzle and the initial velocity profile is not important, while in the limit

$$Gr_j \sim \frac{b_o}{\ell} \ , \tag{2.34b}$$

i.e., that of Case IVb, the initial jet velocity profile is required. Since the scalings for both cases are identical, the entry lengths are the same and are found by equating $\delta \sim \Delta$, i.e.,

$$\ell \sim b_o(Re_j^2/Gr_j)^{1/3} , \tag{2.35a}$$

where

$$\delta \sim b_o(Gr_jRe_j)^{-1/3} , \tag{2.35b}$$

and

$$u_c = u_j(Gr_jRe_j)^{1/3} . \tag{2.35c}$$

These results are substituted into (2.34) to show that Case IVa applies in the asymptotic limit

$$Gr_jRe_j >> 1 , \tag{2.36a}$$

while Case IVb applies in the asymptotic limit

$$Gr_jRe_j \sim 1 . \tag{2.36b}$$

Case V: Negligible Buoyancy

In the asymptotic limit of a small buoyancy force, which is defined as

$$Gr_j << \frac{b_o}{\ell} , \tag{2.37}$$

the inviscid core is a plug flow. In this case the scalings for the

width of the core region and the characteristic velocity are given by those at the nozzle conditions

$$\delta \sim b_o, \quad \text{and} \quad u_c = u_j \ . \tag{2.38a}$$

The width of the boundary layer then scales like

$$\Delta \sim (b_o \ell / Re_j)^{1/3} \ , \tag{2.38b}$$

and the entry length is given by

$$\ell \sim b_o Re_j \ . \tag{2.39}$$

Hence this case applies in the asymptotic limit

$$Gr_j Re_j << 1 \ . \tag{2.40}$$

2.5 Description of the Flow Sequence

A description of the jet as it flows downstream can now be constructed from the different Cases I - V discussed in the previous section. The pure fluid jet exits the nozzle and flows in an inviscid core. Small boundary layers grow in the pure fluid and suspension as the jet flows downstream until their widths are of a size comparable to that of the core region. The pure fluid boundary layers then merge and a fully developed flow results. The distance from the nozzle where the boundary layers merge, along with other scaling results for the entry region flows Cases IV and V, are given

Table 1

Summary of the Entry Region Flows

Solution	Asymptotic Limit	Scalings	Flow Characteristics
Case IVa	$Gr_jRe_j >> 1$	$\delta \sim b_o(Gr_jRe_j)^{-1/3}$ $\Delta \sim b_o(Gr_jRe_j)^{-1/3}$	buoyancy accelerated core
	$Re_j >> 1$	$u_c = u_j(Gr_jRe_j)^{1/3}$ $\ell \sim b_o(Re_j^2/Gr_j)^{1/3}$	jet momentum negligible
Case IVb	$Gr_jRe_j \sim 1$	$\delta \sim b_o(Gr_jRe_j)^{-1/3}$ $\Delta \sim b_o(Gr_jRe_j)^{-1/3}$	buoyancy accelerated core
	$Re_j >> 1$	$u_c = u_j(Gr_jRe_j)^{1/3}$ $\ell \sim b_o(Re_j^2/Gr_j)^{1/3}$	jet momentum important
Case V	$Gr_jRe_j << 1$	$\delta \sim b_o$ $\Delta \sim b_o$	plug flow core
	$Re_j >> 1$	$u_c = u_j$ $\ell \sim b_oRe_j$	buoyancy negligible

Table 2

Summary of the Fully Developed Flows

Solution	Asymptotic Limit	Scalings	Flow Characteristics
Case I	$\frac{1}{b_o} >> (Re_j^2/Gr_j)^{1/3}$ $\frac{1}{b_o} >> (Gr_j Re_j^3)^{-1/3}$	$\delta \sim (b_o^6/Gr_j^2 Re_j)^{1/5}$ $\Delta \sim (b_o^3/Gr_j Re_j^3)^{1/5}$ $u_c = u_j (Gr_j^2 Re_j/b_o)^{1/5}$	buoyancy dominated plume flow
Case II	$\frac{1}{b_o} \sim (Re_j^2/Gr_j)^{1/3}$ $Re_j >> 1$	$\delta \sim 1/Re_j$ $\Delta \sim 1/Re_j$ $u_c = u_j b_o Re_j$	buoyancy, viscosity, inertia, important plume-jet flow
Case III	$\frac{1}{b_o} << (Re_j^2/Gr_j)^{1/3}$ $Re_j >> 1$	$\delta \sim 1/Re_j$ $\Delta \sim 1/Re_j$ $u_c = u_j b_o Re_j$	inertia dominated jet flow

in Table 1.

The general scaling features of the fully developed flows Cases I - III are summarized in Table 2. The asymptotic limits where the solutions apply depend on the relative sizes of the dimensionless distance from the nozzle, H/b_o^*, and the parameter $(Re_j^2/Gr_j)^{1/3}$. Hence, the fully developed flow in the pure fluid exhibits i) jet, ii) mixed plume-jet, and iii) plume characteristics for distances from the nozzle that are i) much less than, ii) of the same order as, and iii) much greater than the value of $(Re_j^2/Gr_j)^{1/3}$. Of course, the pure fluid may not exhibit the fully developed mixed plume-jet or jet flows, i.e., Cases II and III depending on the size of the entry region length. However the buoyancy dominated flow represented by Case I will always apply at large enough distances downstream.

There are essentially two different flow sequences which result for the conditions where $Gr_jRe_j \ll 1$, and $Gr_jRe_j \geq 1$. For the case where $Gr_jRe_j \ll 1$, the entry region flow is represented by the core jet solution in Case V. The distance over which this solution applies is much less than that for the mixed plume solution in Case IIa; i.e., from (2.39) and (2.22a)

$$\ell \sim b_oRe_j \ll (Re_j^2/Gr_j)^{1/3} ,$$

where the inequality results from the assumption that $Gr_jRe_j \ll 1$.

Thus, when the boundary layers merge at a distance of $O(b_oRe_j)$, the pure fluid jet flow described in Case III results (cf. 2.24). As the jet flows downstream, buoyancy effects become increasingly important and, at the dimensionless distance $H/b_o^* \sim (Re_j^2/Gr_j)^{1/3}$, the

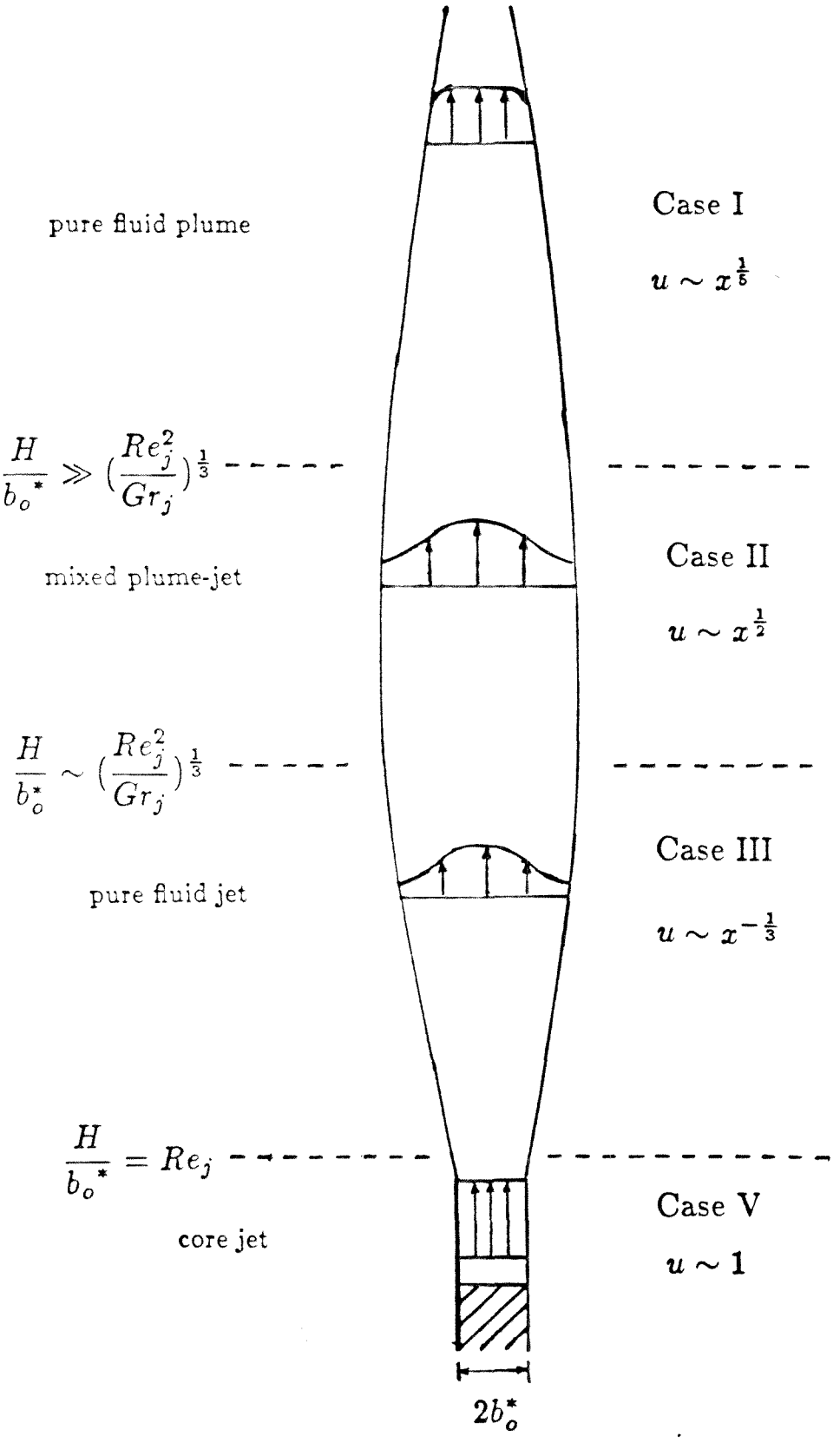

Figure 2 The pure fluid flow sequence for $Gr_j Re_j \ll 1$.

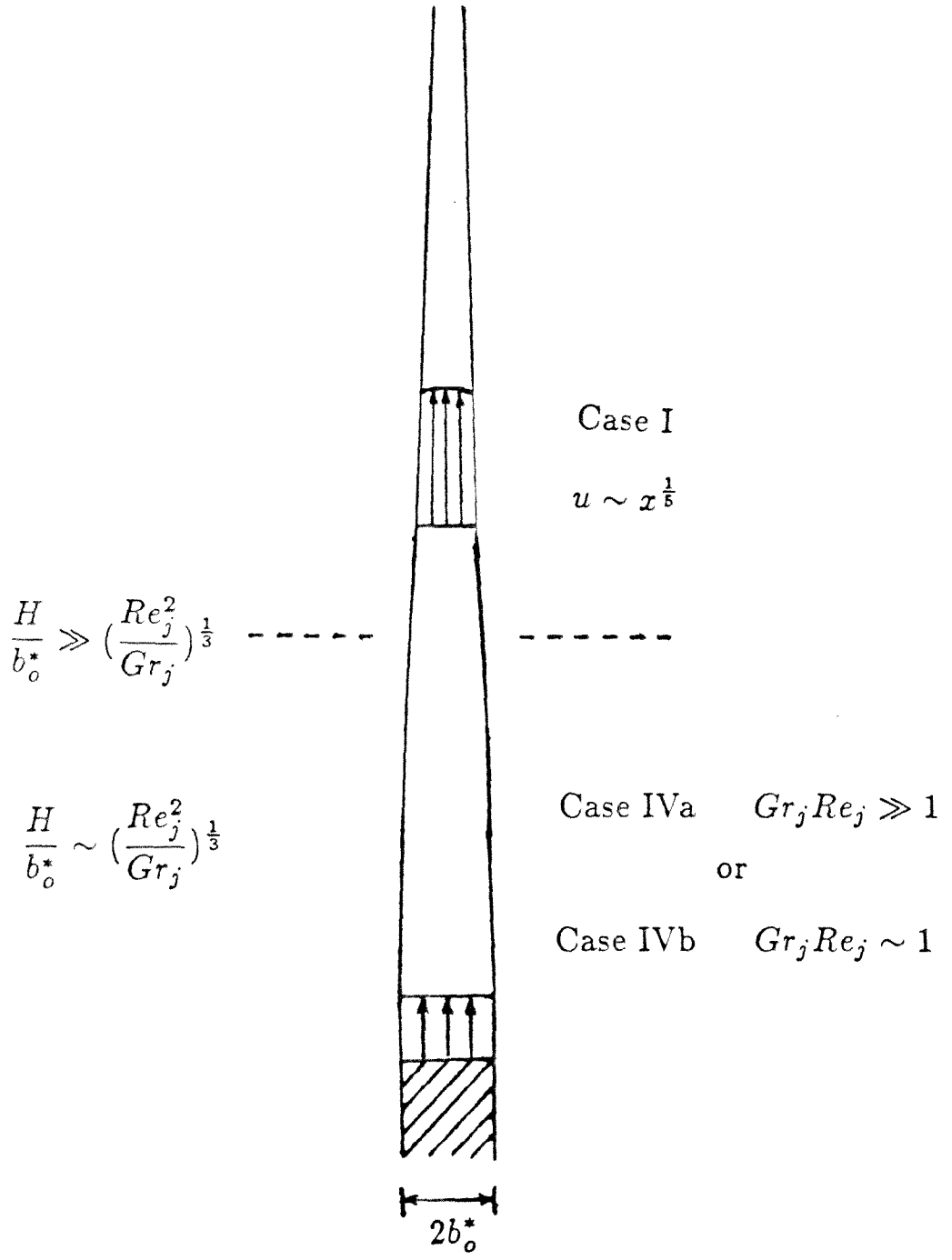

Figure 3 The pure fluid flow sequence for $Gr_j Re_j \geq 1$.

mixed plume-jet (Case IIa) results. Finally, at still larger distances the buoyancy force dominates the flow, and causes a plume-like flow (Case I). This flow sequence is shown schematically in Figure 2, where the initial velocity profile is assumed to be flat.

The flows with stronger buoyancy (i.e., $Gr_j Re_j \gg 1$ and $Gr_j Re_j \sim 1$) are quite similar except that the boundary layers in the pure fluid merge at a distance from the nozzle of order $(Re_j^2/Gr_j)^{1/3}$ (cf. 2.35a). Hence the flow sequence goes directly from the entry region solution (given by Case IVa for $Gr_j Re_j \gg 1$, and Case IVb for $Gr_j Re_j \sim 1$) to the fully developed plume solution. This flow sequence is shown in Figure 3 for a flat initial velocity profile.

2.6 Solutions

The qualitative features of the solutions to the governing equations for Cases I - V have already been discussed in the previous two sections. To complete the analysis, we shall determine the analytical solutions of these equations, where possible. Solving for the flow in the pure fluid region is simple, and in most cases a similarity transformation may be used to simplify the boundary layer equations describing the flow in the suspension region to a single (nonlinear) ordinary differential equation. This equation is then integrated numerically using a standard subroutine. In Cases IIb and IVb this simplification was not possible. However, since the solutions of these problems are not expected to yield any additional insight, full numerical calculations in these cases were not performed. Also, for convenience, the equations were solved in the

dilute limit for which $\mu_o = \rho_o = 1$. Extension to the nondilute case is straightforward and the solutions are similar.

Case I Large Buoyancy

For the buoyancy dominated flow, the equation governing the flow in the pure fluid is

$$\frac{\partial^2 u}{\partial \bar{y}^2} = -\varepsilon + \varepsilon^2 \left(u\frac{\partial u}{\partial x} + \bar{v}\frac{\partial u}{\partial \bar{y}}\right) + O\left(\frac{\varepsilon^4}{Re_j^2}\right) , \tag{2.41}$$

where

$$\varepsilon = \frac{\delta}{\Delta} \sim (b_o^3 Re_j^2/Gr_j)^{1/5} . \tag{2.42}$$

This can be integrated twice and the centerline condition (2.13a) applied to give

$$u = a_o(x) - \varepsilon \frac{\bar{y}^2}{2} + \varepsilon^2 \frac{\bar{y}^2}{2} a_o \frac{da_o}{dx} + O(\varepsilon^3) . \tag{2.43}$$

The integration constant is then found from the volumetric constraint (2.13f)

$$a_o(x) = \frac{1}{b} + \varepsilon \frac{b^2}{6} + \varepsilon^2 \frac{1}{6b} \frac{db}{dx} + O(\varepsilon^3) . \tag{2.44}$$

Upon substituting (2.44) into the boundary conditions (2.13), the equations governing the suspension flow become

$$u^s \frac{\partial u^s}{\partial x} + (\bar{v}^s - \varepsilon \frac{db}{dx} u^s) \frac{\partial u^s}{\partial \tilde{y}} = \nu_o \frac{\partial^2 u^s}{\partial \tilde{y}^2} + O(\frac{\varepsilon}{Re_j})^2 , \qquad (2.45a)$$

$$\frac{\partial u^s}{\partial x} + \frac{\partial \bar{v}^s}{\partial \tilde{y}} - \varepsilon \frac{db}{dx} \frac{\partial u^s}{\partial \tilde{y}} = 0 , \qquad (2.45b)$$

$$v^s = 0 \qquad \text{at } \tilde{y} = 0 , \qquad (2.46a)$$

$$u^s = \frac{1}{b(x)} \qquad \text{at } \tilde{y} = 0 , \qquad (2.46b)$$

$$\frac{\partial u^s}{\partial \tilde{y}} = - \frac{1}{\mu_o} b(x) \qquad \text{at } \tilde{y} = 0 , \qquad (2.46c)$$

$$u^s \to 0 \qquad \text{as } \tilde{y} \to \infty , \qquad (2.46d)$$

$$u^s \to 0 \qquad \text{as } x \to 0 . \qquad (2.46e)$$

This problem can be solved using a similarity transformation of the form

$$u^s = E(x) F'(\eta) , \qquad (2.47)$$

where

$$\eta = \frac{\tilde{y}}{G(x)} .$$

Taking the necessary derivatives and substituting them into the governing equations and boundary conditions gives

$$\nu_o F''' - (F')^2 - 3FF'' = 0 \ , \tag{2.48}$$

$$F(0) = 0 \ , \tag{2.49a}$$

$$F'(0) = A \ , \tag{2.49b}$$

$$F''(0) = \frac{1}{\mu_o A} \ , \tag{2.49c}$$

$$F'(\infty) = 0 \ , \tag{2.49d}$$

where

$$u^S = (5x)^{1/5} F'(\eta) \ , \tag{2.50a}$$

$$v^S = (5x)^{-2/5} [2\eta F' - 3F] - \varepsilon \frac{1}{5x} \frac{F'(\eta)}{F(0)} \ , \tag{2.50b}$$

and

$$\eta = \frac{\tilde{y}}{(5x)^{2/5}} \ , \tag{2.50c}$$

and the constant A must be determined from the numerical solution. Note that the two boundary conditions (2.46d) and (2.46e) collapse to (2.49d) as is necessary for application of a similarity solution. Equation (2.48) is the Falkner-Skan equation except there is no pressure term and the boundary conditions are different.

This system of equations was solved numerically using a shooting technique. Initial values for the function and its first two derivatives are specified at the interface. The equations are then integrated numerically using the canned subroutine MODDEQ, which was

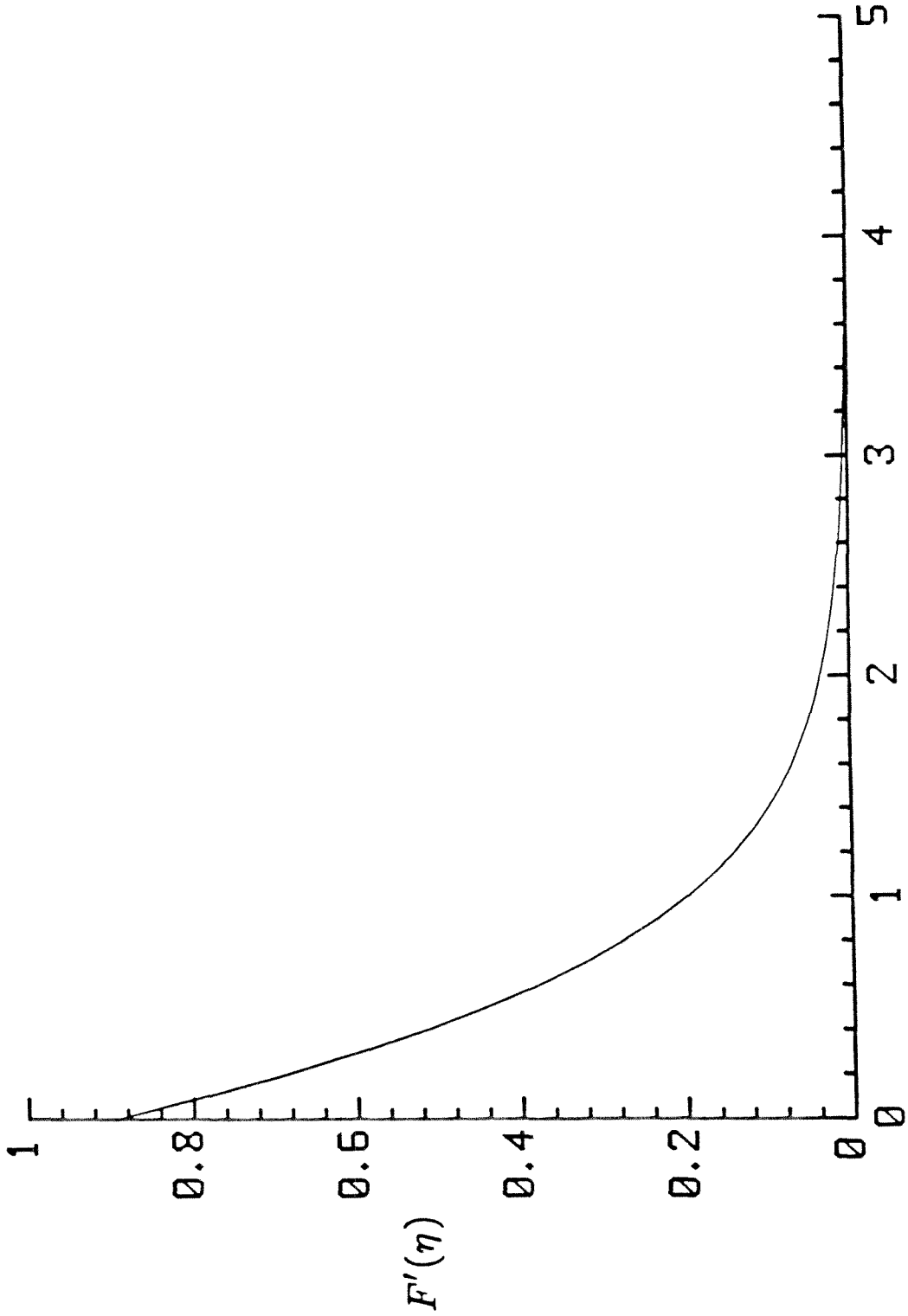

Figure 4 The Case I solution of equation (2.48) : $u^* \propto F'(\eta)$

modified slightly to include double precision variables. The Runge-Kutta-Gill method is used at the beginning of the integration and whenever the interval size is changed. The values of the function and its derivatives that are calculated from this method are then used as starting values for the iterative Adams-Moulton method.

As mentioned previously, the calculations were performed for $\nu_o = \mu_o = 1$ only. The results for $F'(\eta)$, (i.e., the velocity profile for u^s at constant x) in the dilute limit are plotted in Figure 4. As expected, the suspension velocity quickly decays to zero as the distance from the interface increases. The computed numerical value of the constant $A = 0.8927$ is then used to determine the width of the pure fluid region

$$b(x) = .8119\ x^{-1/5} . \tag{2.51}$$

The flow in the pure fluid region strongly resembles that of a laminar plume above a line source of heat. Fujii (1963) solved this problem at several Prandtl numbers using a self-similar solution, and found that the velocity accelerated with increasing axial distance according to

$$u \sim x^{1/5} .$$

Furthermore, he determined that the velocity scaled as

$$u_c \sim G^{2/5} ,$$

where G is the buoyancy flux (a constant) and is analogous to the jet Grashof number in this problem. These results can be compared to those in (2.43), (2.44), and (2.51), and (2.17c) to show that the pure fluid velocity, and scaling velocity in Case I behave in an identical manner.

Case II: Moderate Buoyancy

This case divides into two subcases depending on the magnitude of the parameter $Gr_j Re_j$. Substituting the scalings for the pure fluid thickness and velocity (cf. 2.21a and 2.22a) into the momentum constraint (2.13g) gives

$$\int_0^b u^2 \, d\bar{y} + \rho_o \int_0^\infty (u^s)^2 \, d\tilde{y} = \int_0^x b(\xi) \, d\xi + \frac{\beta}{(Gr_j Re_j)^{1/3}} . \qquad (2.52)$$

For Case IIa where $Gr_j Re_j >> 1$, the initial momentum of the jet is negligible, (i.e., $u \to 0$ as $x \to 0$), and a solution can be found using a similarity transformation. However for Case IIb where $Gr_j Re_j \sim 1$, the initial momentum is important and in this case, no analytical solution has been found. Hence we shall solve this problem only in the asymptotic limit of large $Gr_j Re_j$.

Case IIa: $Gr_j Re_j >> 1$

Following the same procedure taken for Case I, we assume solutions of the form

$$u = E(x)\, f'(\eta) , \tag{2.53a}$$

and

$$u^S = E(x)\, F'(\eta) , \tag{2.53b}$$

where the similarity variable is defined as

$$\eta = \frac{\tilde{y}}{G(x)} . \tag{2.53c}$$

Substitution into the partial differential equations governing the flow in the pure fluid and suspension (cf. 2.23, 2.11b, and 2.12) gives the ordinary differential equations

$$f''' - (f')^2 + \frac{3}{2} ff'' + 1 = 0 \qquad -1 \leq \eta \leq 0 , \tag{2.54a}$$

and

$$\nu_o F''' - (F')^2 - \frac{3}{2} FF'' = 0 \qquad \eta > 0 . \tag{2.54b}$$

The boundary counditions in (2.13) are also transformed to

$$f''(-1) = 0 , \tag{2.55a}$$

$$f(0) = F(0) = 0 , \tag{2.55b}$$

$$f'(0) = F'(0) , \tag{2.55c}$$

$$f''(0) = \mu_o F''(0) , \tag{2.55d}$$

$$F'(\infty) = 0 \ . \tag{2.55e}$$

In order for the existence of a self-similar solution, the transformations must be of the form

$$u = (2x)^{1/2} f'(\eta) \ , \tag{2.56a}$$

$$\tilde{v} = \frac{1}{2} (2x)^{-1/4} [(\eta + 1)f' - 3f] \ , \tag{2.56b}$$

and

$$u^S = (2x)^{1/2} F'(\eta) \ , \tag{2.56c}$$

$$\tilde{v}^S = \frac{1}{2} (2x)^{-1/4} [(\eta + 1)F' - 3F] \ , \tag{2.56d}$$

where

$$\bar{\eta} = \frac{\tilde{y}}{(2x)^{1/4}} \tag{2.56e}$$

and the functions $f'(\eta)$ and $F'(\eta)$ are evaluated numerically. The velocity profile for the dilute limit case is shown in Figure 5. In comparison with the solution in Case I, the smaller buoyancy force causes a weaker acceleration in the pure fluid, i.e., $x^{1/2}$ as opposed to $x^{1/5}$ (where $x < 1$). In addition, the increased importance of the drag due to the suspension region causes the pure fluid region to spread according to

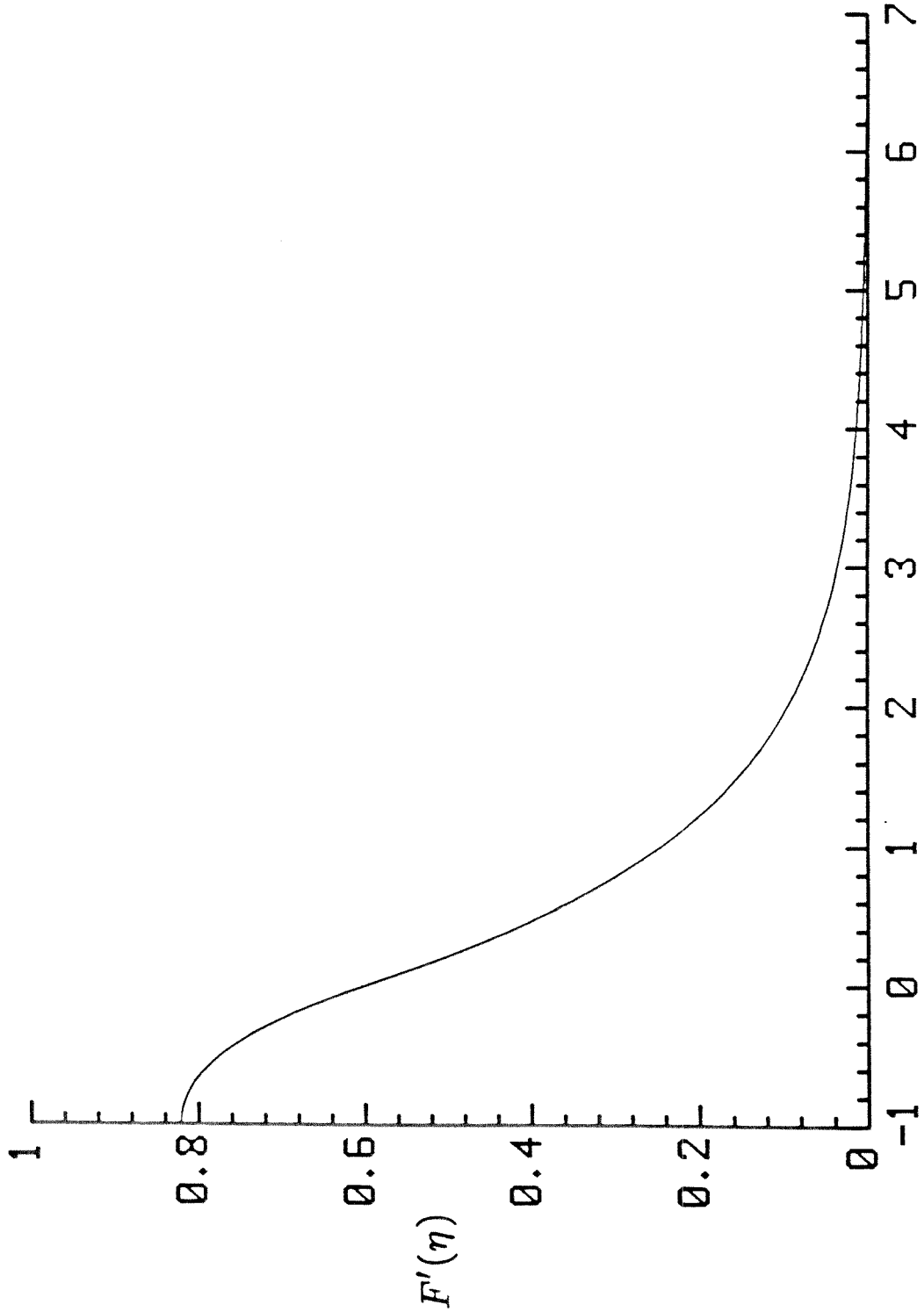

Figure 5 The Case IIa solution of equations (2.54a and b):
$u \alpha F'(\eta)$ *for* $\eta \leq 0$; $u^* \alpha F'(\eta)$ *for* $\eta > 0$.

$$b \sim x^{1/4} . \tag{2.56f}$$

Case III: Small Buoyancy

For convenience, we rewrite the equations governing the motion in the suspension in terms of the stretched pure fluid variable $\bar{y}$. The governing equations and boundary conditions are then given by

$$u\frac{\partial u}{\partial x} + \bar{v}\frac{\partial u}{\partial \bar{y}} = \frac{\partial^2 u}{\partial \bar{y}^2} , \tag{2.57a}$$

$$\frac{\partial u}{\partial x} + \frac{\partial \bar{v}}{\partial \bar{y}} = 0 , \tag{2.57b}$$

$$u^S\frac{\partial u^S}{\partial x} + \bar{v}^S\frac{\partial u^S}{\partial \bar{y}} = \nu_o\frac{\partial^2 u^S}{\partial \bar{y}^2} , \tag{2.58a}$$

$$\frac{\partial u^S}{\partial x} + \frac{\partial \bar{v}^S}{\partial \bar{y}} = 0 , \tag{2.58b}$$

$$\bar{v} = \frac{\partial u}{\partial \bar{y}} = 0 \qquad \text{at } \bar{y} = 0 , \tag{2.59a}$$

$$\bar{v} = \bar{v}^S \qquad \text{at } \bar{y} = b , \tag{2.59b}$$

$$u = u^S \qquad \text{at } \bar{y} = b , \tag{2.59c}$$

$$\frac{\partial u}{\partial \bar{y}} = \mu_o\frac{\partial u^S}{\partial \bar{y}} \qquad \text{at } \bar{y} = b , \tag{2.59d}$$

$$u^s \to 0 \qquad \text{as } \bar{y} \to \infty \,, \tag{2.59e}$$

and

$$\int_0^b u^2 \, d\bar{y} + \rho_o \int_b^\infty (u^s)^2 \, d\bar{y} = \beta \,. \tag{2.59f}$$

In the dilute limit, these equations and boundary conditions are identical to those describing the flow of a pure fluid laminar jet issuing from a line source of momentum. Hence following the approach used by Bickley (1937), who first solved the laminar jet problem, we obtain expressions for the fluid velocities in terms of analytical functions

$$u = \frac{3}{2} \left(\frac{\beta}{3}\right)^{2/3} x^{-1/3} \operatorname{sech}^2 \bar{\eta} \,, \tag{2.60a}$$

and

$$\bar{v} = \left(\frac{\beta}{3}\right)^{1/3} x^{-2/3} \left[2\bar{\eta} \operatorname{sech}^2 \bar{\eta} - \tanh^2 \bar{\eta}\right] \,, \tag{2.60b}$$

where

$$\bar{\eta} = \frac{1}{2} \left(\frac{\beta}{3}\right)^{1/3} \frac{\bar{y}}{x^{2/3}} \,. \tag{2.60c}$$

A plot of the axial velocity profile is given in Figure 6. Of course in the flow of a jet in a dilute suspension, the particles mark the position of the interface which is given by

$$b(x) \sim x^{2/3} \tanh^{-1}(x^{-1/3}) \,. \tag{2.60d}$$

Although this is a complicated function of x, the rate of spreading

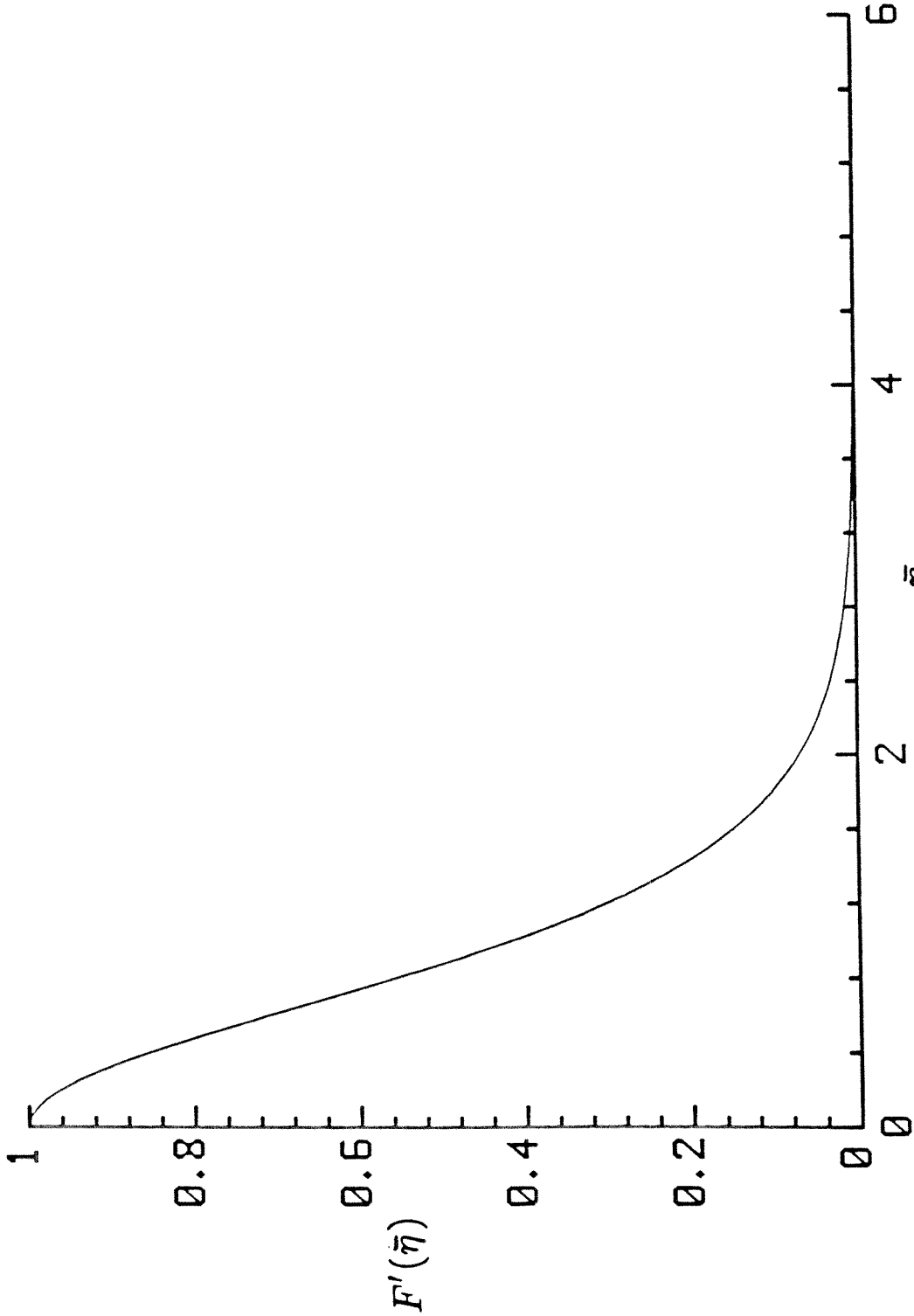

Figure 6 The Case III solution of equations (2.57a and b): $u \propto sech^2(\bar{\eta})$.

of the pure fluid region asymptotes to

$$b \sim x^{1/3} \qquad \text{as } x \to \infty \ .$$

This is faster than the $x^{1/4}$ spreading rate of Case IIa because there is no buoyancy force to counteract the viscous drag.

Case IV

As in Case II, a similarity solution is not possible if the initial momentum of the jet is important. Hence only Case IVa, where $Gr_j Re_j \gg 1$, will be considered. The velocity in the core region is determined by the solution of (2.31) using the scalings from (2.33) and (2.34) which gives

$$u = (2\bar{x})^{1/2} \ , \tag{2.61a}$$

and hence the buoyancy force accelerates the pure fluid. Thus, we find from the volumetric constraint (2.30h) that the width of the pure fluid must decrease with increasing distance from the nozzle

$$b = (2\bar{x})^{-1/2} \ . \tag{2.61b}$$

Transforming the equations in the pure fluid and suspension boundary layers using self-similar solutions of the form

$$u = (2\bar{x})^{1/2} f'(\eta) \ , \tag{2.62a}$$

$$\tilde{v} = \frac{1}{2}(2\bar{x})^{-1/4}[\eta f' - 3f] - \frac{1}{2\bar{x}} f' , \qquad (2.62b)$$

and

$$u^S = (2\bar{x})^{1/2} F'(\eta) , \qquad (2.62c)$$

$$\tilde{v}^S = \frac{1}{2}(2\bar{x})^{-1/4}[\eta F' - 3F] - \frac{1}{2\bar{x}} F' , \qquad (2.62d)$$

where

$$\eta = \frac{\tilde{y}}{(2\bar{x})^{1/4}} , \qquad (2.62e)$$

gives the ordinary differential equations

$$f''' - (f')^2 + \frac{3}{2} f f'' + 1 = 0 \qquad \eta \leq 0 , \qquad (2.63a)$$

and

$$\nu_o F''' - (F')^2 - \frac{3}{2} F F'' = 0 \qquad \eta > 0 , \qquad (2.63b)$$

with the boundary conditions

$$f'(-\infty) = 1 , \qquad (2.64a)$$

$$f(0) = F(0) = 0 , \qquad (2.64b)$$

$$f'(0) = F'(0) , \qquad (2.64c)$$

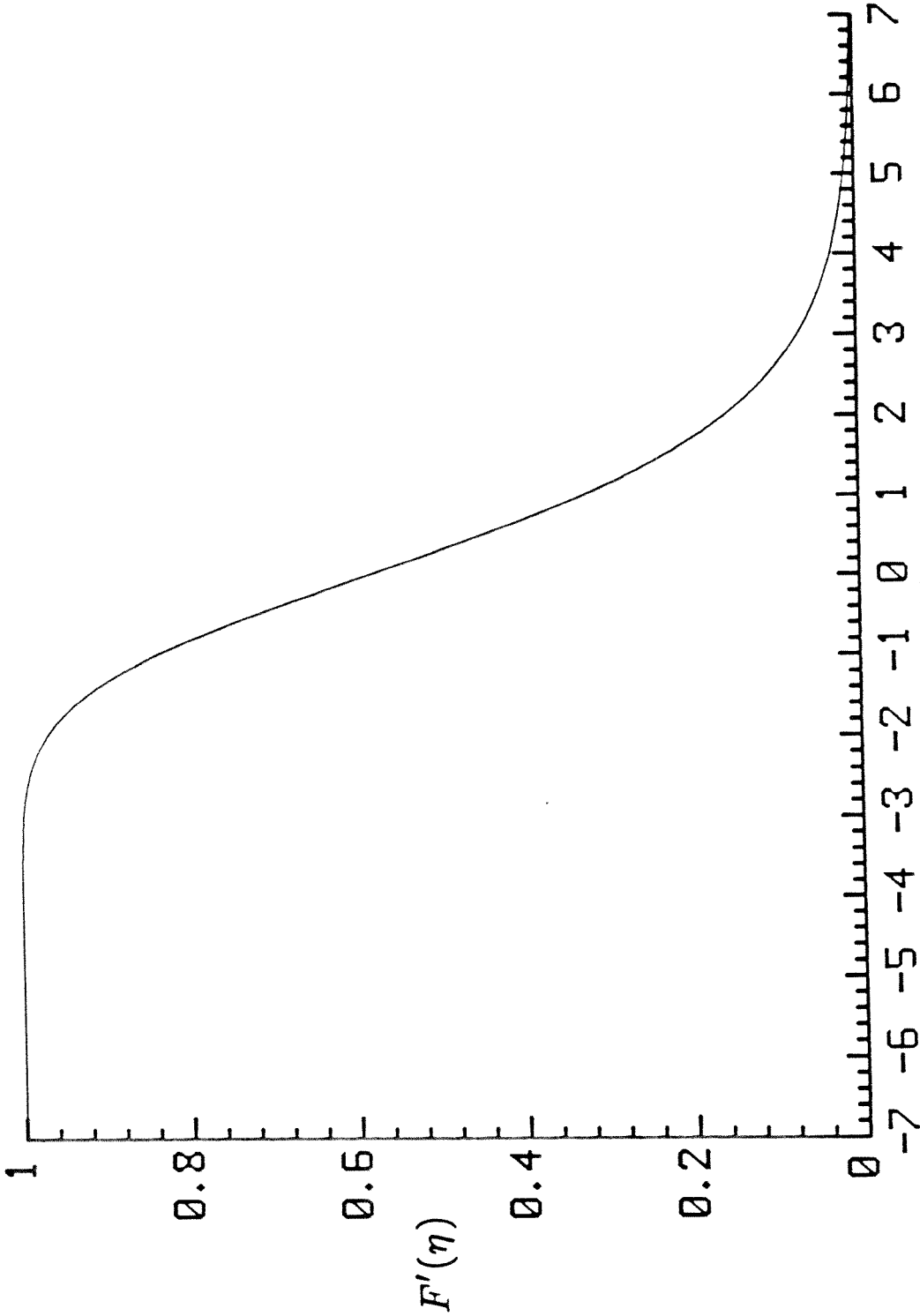

Figure 7 The Case IVa solution of equations (2.63a and b): $u \alpha F'(\eta)$ *for* $\eta \leq 0$; $u' \alpha F'(\eta)$ *for* $\eta > 0$.

$$f''(0) = \mu_o F''(0) \ , \tag{2.64d}$$

$$F'(\infty) = 0 \ . \tag{2.64e}$$

Hence, the axial velocity in the boundary layer increases with increasing distance from the nozzle. In fact, the dependence of this velocity on x is identical to that in Case IIa (cf. 2.56 and 2.62). This supports the result obtained in section 2.5 that the fully developed flow represented by the solution of Case IIa does not appear at the dimensionless distance $(Re_j^2/Gr_j)^{1/3}$, and is replaced by the flow represented in the entry region solution of Case IVa. Solving the equations (2.63 - 2.64) numerically in the dilute limit gives the velocity profile shown in Figure 7.

Case V

In this case the velocity profile in the core region is the same as that exiting the nozzle

$$u = u_i(\bar{y}) \tag{2.65a}$$

Since to leading order the axial velocity and the volumetric flow rate are both independent of the axial coordinate x, the width of the pure fluid region is a constant

$$b = 1 \ . \tag{2.65b}$$

Again using a similarity transformation, the solution is represented

by

$$u = f'(\eta) \ , \tag{2.66a}$$

$$\tilde{v} = (2\bar{x})^{-1/2} [\eta f' - f] \ , \tag{2.66b}$$

and

$$u^S = F'(\eta) \ , \tag{2.66c}$$

$$\tilde{v}^S = (2\bar{x})^{-1/2} [\eta F' - F] \ , \tag{2.66d}$$

where

$$\eta = \frac{\tilde{y}}{(2\bar{x})^{1/2}} \ , \tag{2.66e}$$

and the governing equations and boundary conditions reduce to

$$f''' + ff'' = 0 \qquad \eta \leq 0 \ , \tag{2.67a}$$

$$\nu_o F''' + FF'' = 0 \qquad \eta > 0 \ , \tag{2.67b}$$

$$f'(-\infty) = 1 \tag{2.68a}$$

$$f(0) = F(0) = 0 \tag{2.68b}$$

$$f'(0) = F'(0) \tag{2.68c}$$

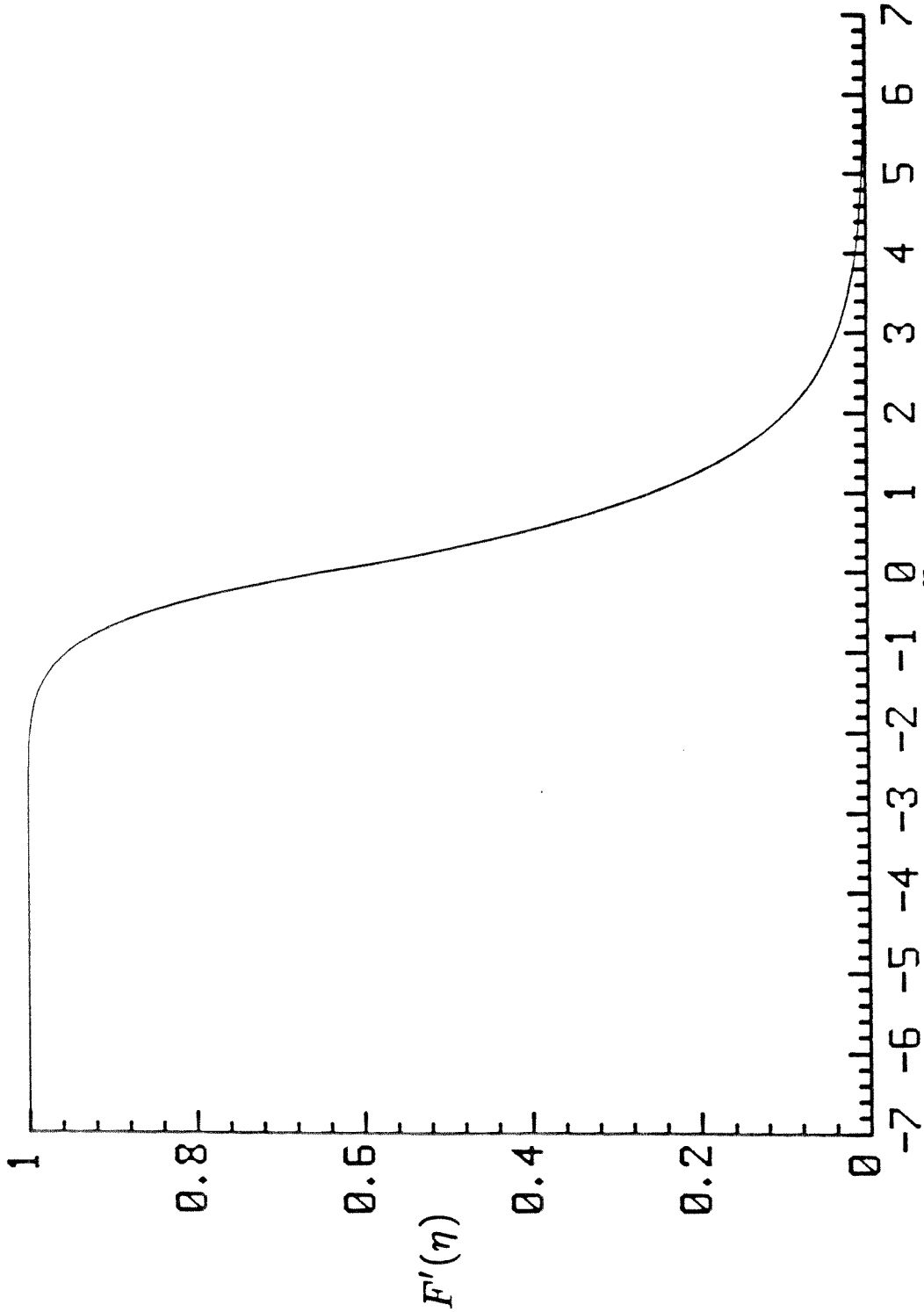

Figure 8 The Case V solution of equations (2.67a and b):
$u \alpha F'(\eta)$ *for* $\eta \leq 0$; $u' \alpha F'(\eta)$ *for* $\eta > 0$.

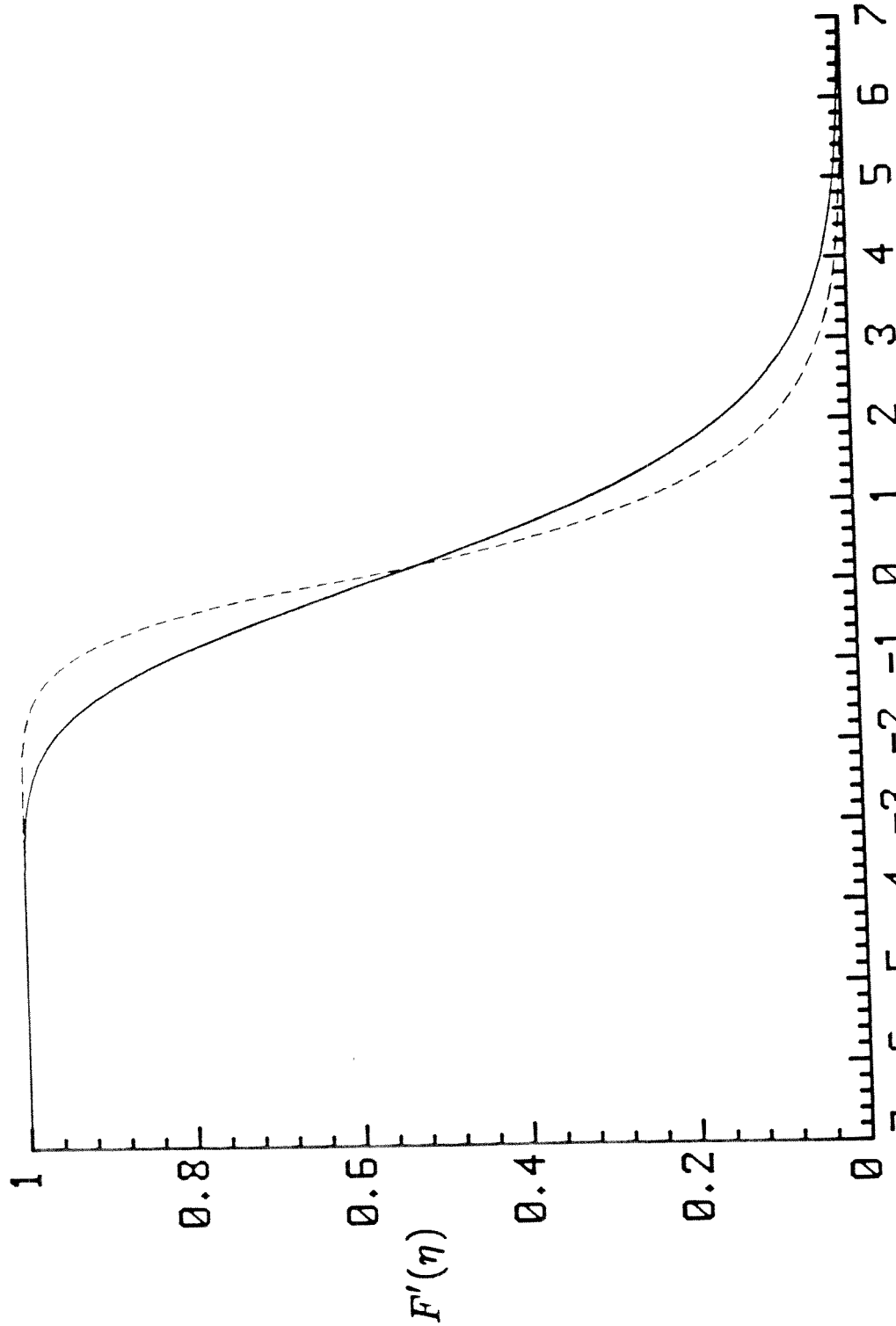

Figure 9 Comparison of Case IVa and Case V solutions: the solid curve is the Case IVa solution; the dashed curve is the Case V solution.

$$f''(0) = \mu_o F''(0) \tag{2.68d}$$

$$F'(\infty) = 0 \ . \tag{2.68e}$$

The velocity profile from the numerical solution for the dilute limit is given in Figure 8. A comparison of this velocity profile with that from Case IVa, (cf. Figure 9) shows that the velocity gradients for Case V are steeper. Hence in addition to accelerating the velocity in the axial direction, the buoyancy force also flattens the velocity profile.

2.7 Discussion

The present analysis describes the possible flow sequences which may develop when a laminar jet of fluid issues vertically into a homogeneous suspension. By comparing the solutions that we have just derived with those for the analogous single phase momentum jet or thermal plume problems, we see that the presence of particles in the flow field has a dramatic effect on the pure fluid flow.

One obvious effect of the particles is to alter the flow configuration. For the momentum jet or thermal plume, the flow region is confined to a single boundary layer region where the driving force for the flow is located at the origin. However, for the jet in an initially homogeneous suspension at small particle Reynolds numbers, the pure fluid and suspension phases do not mix and the flow field divides into the three different flow regions of the pure fluid jet, the suspension boundary layer driven by the jet, and an outer nearly stagnant suspension. Consequently additional

equations which describe the flow in the suspension region, as well as new boundary conditions at the interface separating the pure fluid and the suspension must be formulated.

The separation of the flow field into regions of constant concentration, i.e., $c = 0$ and $c = c_o$, causes a constant buoyancy force to be exerted on the pure fluid, (provided that the particles are more dense than the pure fluid). This is in contrast with the flow of a thermal plume, where the temperature difference between the plume and the environment decreases with distance from the heat source. Thus, in a heated jet with a small amount of buoyancy, the flow resembles that of a momentum jet (Mollendorf and Gebhart 1973a). However, in the analogous suspension flow problem, the particles have a significant effect on the jet, as even a small buoyancy force will eventually cause a transition to a plume-like flow. This was observed in experiments that we performed where dye particles which were used for flow visualization purposes (and were slightly more dense than the pure fluid) caused plume-like flow characteristics (e.g. slower spreading rate) in the jet. In some of these experiments, instabilities caused a transition in the flow before the plume-like solution was attained. Hence, although the analysis predicts ranges of the parameters Gr_j, Re_j, and H/b_o^* over which the solutions to Cases I - V apply, we need to restrict these ranges further when we consider unstable flows. In the next chapter we shall examine the stability of these flow solutions to small amplitude disturbances.

CHAPTER 3

The Stability of a Buoyant Jet in a Homogeneous Suspension

3.1 Introduction

In the previous chapter, asymptotic solutions of the governing equations of motion were developed to describe the flow of a jet issuing into a suspension. Of course, these solutions should accurately describe the jet only so long as the flow remains stable. However in several experiments where we observed this jet flow, particles from the suspension were mixed into the pure fluid region by a wave-type disturbance of the interface.

For flows at very small values of the jet Grashof number, the pure fluid issued vertically from the nozzle and sharp interface boundaries existed between it and the suspension region. Further downstream, sinusoidal waves appeared at each interface. The waves on the two interfaces had identical wavelengths and amplitudes but they were antisymmetric with respect to the centerline of the jet. The amplitudes of the waves grew with distance, and as they grew, an increasing number of particles were mixed into the pure fluid region. Eventually, the pure fluid region could no longer be discerned.

For flows at larger values of the jet Grashof number, the width of the pure fluid region decreased with distance from the nozzle. The portion of the jet near the nozzle oscillated slightly with a frequency on the order of 0.005 sec^{-1}. In this region, the interfaces of the jet remained two-dimensional and smooth, i.e., no particles were mixed in with the pure fluid. Near the tip of the pure fluid

region, the jet oscillated with a much larger amplitude, and frequency (on the order of 0.1 sec^{-1}) which caused the pure fluid region to bend in a sinuous mode. This resulted in many particles mixing into the pure fluid region so that it could not be seen.

In order to better understand these instabilities and the conditions which cause them, we examined the growth of small disturbances at the interfaces of the asymptotic base flow solutions developed in Chapter 2. The linearized equations which describe the growth of small amplitude disturbances in parallel shear flows are the well-known Orr-Sommerfeld equations. These equations can also be applied to leading order to describe the growth of small disturbances in the larger class of nearly parallel flows. In this case, the errors are due to neglecting the nonparallel terms in the stability equations, as well as the inaccuracy of the base flow solution. In the asymptotic limit of some large parameter these errors are small, and the approximation is a good one. The earlier stability analyses for both parallel and nearly parallel flows focused primarily on predicting critical Reynolds or Grashof numbers above which disturbances would grow. However, more recent analyses have shown the importance of determining the growth rates and frequencies of the unstable disturbances as well.

One example out of several nearly parallel flows for which the stability problem has been extensively examined is boundary layer flow over a flat plate. The stability of this flow to small disturbances was first investigated by Tollmein (1929). By neglecting the nonparallel terms and solving the Orr-Sommerfeld equations he found a critical Reynolds number of 575. Gaster (1974),

Smith (1979), and others relaxed the parallel flow assumption and used perturbation techniques to include nonparallel effects. Gaster found that including the nonparallel terms of $O(Re^{-1/2})$ reduced the critical Reynolds number to approximately 500. Smith used a multiple scales approach to develop the asymptotic structure of the nonparallel terms with the disturbance wavelength as the asymptotic parameter. His analysis also gave a critical Reynolds number of approximately 500. Although the nonparallel results generally are in better agreement with the experimentally observed critical Reynolds number of approximately 400 (cf. Schubauer and Skramstad (1948)), the differences from the parallel flow results are not large. This is because the error terms of the equations governing the disturbed flow, and of the base flow solution, are of order $(Re^{-1/2})$. Thus the error for a critical Reynolds number of O(500), (i.e., approximately 0.045) is small, at least in a numerical sense.

In general, free boundary layer flows, such as jets or plumes, are less stable than semibounded or unbounded flows due to the lack of disturbance damping at the bounding surfaces. Stability analyses of these flows characteristically predict very low critical Reynolds or Grashof numbers. For example, Clenshaw and Elliott (1960) solved the full Orr-Sommerfeld equations numerically in examining the stability of the pure fluid, planar jet to small amplitude disturbances and obtained a critical Reynolds number of 3.7. Pera and Gebhart (1971) investigated the analogous stability problem for a plume above a line source of heat. Using the quasi-parallel flow assumption, they solved the Orr-Sommerfeld equations numerically and found that the plume is unstable at Grashof numbers above 3.5.

Of course, at very low values of the Reynolds or Grashof numbers, the quasi-parallel flow assumption is no longer valid. Recent investigations by Garg (1981), and Wakitani (1985), on the non-parallel stability of the two-dimensional jet, and plume, respectively, included at higher order the effects of the transverse velocity component and of the streamwise variations of the base flow, disturbance wavenumber, and growth rate. However as first pointed out by Bouthier (1973), the various disturbance flow quantities (such as the streamfunction, velocity components, pressure, etc.) have different growth rates, and these result in markedly different stability characteristics depending on which quantity is observed. For the neutral stability curve based on the disturbance's mean kinetic energy, Garg found that the critical Reynolds number was 21.6, a marked increase over that for the parallel flow. In the nonparallel stability analysis for the plume, Wakitani found that the critical Grashof number for the neutral curve based on the disturbance temperature increased to approximately 6.7. Hence, in comparisons of the nonparallel theory with the experimental data for single phase jets or plumes, care must be taken to insure that the amplification rate used is the correct one for the disturbance quantity that is observed.

Experimental studies by Sato and Sakao (1964) on the plane jet, and Bill and Gebhart (1975) for the plane plume, indicate that laminar jets and plumes may be obtained at Reynolds and Grashof numbers well above the critical values predicted by the linear theory. This discrepancy may be due to the error terms in the governing equations for the stability problem. However, a more

plausible explanation is that the amplification rates were so small that the disturbances were convected out of the experimental apparatus, before they could grow to an appreciable size. This was shown to be the case in the studies conducted by Atherton and Homsy (1973) on flow down an inclined plane, and by Herbolzheimer (1983) on sedimentating flow in an inclined channel. The observable onset of instability correlated well with the spatial growth rates predicted by the linear theory but not with the point where the system parameters passed through their critical value. Thus, in specifying the conditions for stability, it is not only important to determine the sign of the amplification factor but the size as well.

There have been relatively few analyses which examine the stability of laminar, single phase, buoyant jets or forced plumes primarily because of the difficulty in calculating the base flow solution. Mollendorf and Gebhart (1973b) studied the growth of small disturbances in a weakly buoyant round jet, where the equations for the base flow include the buoyancy force due to a thermal source at a higher order. Solving the Orr-Sommerfeld equations numerically, they found that the buoyancy force is destabilizing, as the critical Reynolds number decreased from 32.8 (for a round momentum jet), to 9.4. In the present analysis, we shall examine the effect of a buoyancy force, due to the particles in the suspension, on the stability of a two-dimensional jet of pure fluid. This buoyant jet flow differs from those in previous analyses, due to the stronger buoyancy force and the need to determine the interface position rather than a temperature or concentration field.

Stability analyses on flows with an interface have been quite successful in predicting the flow conditions for instability. Benjamin (1957) first studied the stability of the flow of a thin film of fluid down an inclined plane. Yih (1963) later amended this analysis by linearizing the boundary conditions at the fluid-air interface. Herbolzheimer (1983) extended this approach to buoyancy driven flows with a pure fluid-suspension interface in his study on the instability of sedimentation flows in inclined channels. In the following analysis, we will extend this approach still further to buoyant free boundary layer flows with an interface.

Of the five different base flows presented in the previous chapter, we shall only examine the stability of that described by Case I which corresponds to the plume solution. In the dilute limit, the velocity profile in Case III is identical to that for a pure fluid jet, and hence an analysis of the stability of this solution would not be expected to give any new results. The solutions in Cases IVa and V both describe entry flows and only apply in regions very close to the nozzle. Furthermore, a stability analyses of these flows, as well as that in Case IIa, would be difficult because of the numerical solutions in the boundary layers on both sides of the interface. The solution technique would involve a numerical integration of the governing disturbance equations. Although the base flow solution in the suspension region for Case I is also numerical, we shall see that only the interfacial values of the suspension velocity and its derivatives are required.

In the following analysis, we shall first derive the equations and boundary conditions that govern the growth of small amplitude

disturbances in both the pure fluid and suspension regions. Two sets of boundary conditions are derived for the subcases of antisymmetric and symmetric waves so that these may be analyzed separately. The governing equations and boundary conditions for both cases are then solved analytically in the asymptotic limit of small wavelength disturbances and lead to eigenvalue conditions for the complex wavenumber. The roots of these conditions are evaluated numerically, giving the disturbance growth rate as a function of the disturbance frequency. The magnitude of the amplification factor for the most unstable disturbance is then calculated to determine an estimate of the distance where disturbances should first be observed.

3.2 Governing Equations

We begin by deriving the governing equations and boundary conditions for the spatial amplification of small amplitude disturbances in the nearly parallel base flow of Case I. The spatial analysis is chosen over a temporal one because of the instability behavior observed in the experiments.

Squire (1933) showed that in a temporal stability analysis of a parallel flow between two walls any three-dimensional disturbance can be represented as a two-dimensional disturbance at a lower Reynolds number. Gaster (1962) studied the relationship between temporal and spatial growth rates and found that to leading order, these amplification rates were identical near the neutral stability curve. Hence for spatially amplified waves with small growth rates, two-dimensional disturbances are less stable than three-dimensional disturbances. In this analysis, we assume that this result applies

at larger amplification rates as well, and consider two-dimensional disturbances only. Although there is no rigorous justification for this, in the experiments described in Chapter 4, two-dimensional disturbances were the first to be observed.

Following the standard approach for a linear stability analysis, the flow variables are written as the sum of the base flow variable plus a small perturbation. Of course, the two-dimensional disturbance velocities may be written in terms of the streamfunction and we shall denote this as Ψ and Φ in the pure fluid and suspension regions respectively. Using the same characteristic velocity and length scales as the base flow, i.e., u_c and H, the dimensional flow variables in the pure fluid and suspension are then written as

$$u^* = u_c(u + \delta\Psi_y) , \quad v^* = u_c(v - \delta\Psi_x) , \quad p^* = \rho_f u_c^2(p + p') ,$$

and (3.1)

$$u^* = u_c(u^s + \delta\Phi_y) , \quad v^* = u_c(v^s - \delta\Phi_x) , \quad p^* = \rho_f u_c^2(p + p^{s\prime}) ,$$

where the subscripts on the streamfunctions denote partial derivatives, and the streamwise disturbance velocity in the pure fluid, i.e., $u' = \delta u_c \Psi_y$, is defined so that it is $O(u_c)$ in the stretched coordinates. Note that we have restricted the analysis somewhat by assuming that the perturbations occur only in the velocity and pressure fields, while the concentration remains uniform throughout both the pure fluid and suspension regions. Substituting (3.1) into the Navier-Stokes equations, neglecting all quadratic terms in the disturbance variables, and subtracting out the equations governing the base flow gives the disturbance equations of motion in

the pure fluid

$$\Psi_{yt} + u\Psi_{yx} + u_x\Psi_y - u_y\Psi_x + v\Psi_{yy} = -\frac{1}{\delta}\, p'_x + \frac{\delta}{Re_j}\nabla^2\Psi_y \,, \qquad (3.2a)$$

and

$$\Psi_{xt} + u\Psi_{xx} - v_x\Psi_y + v_y\Psi_x + v\Psi_{xy} = \frac{1}{\delta}\, p'_y + \frac{\delta}{Re_j}\nabla^2\Psi_x \,.$$

The pressure may be eliminated by cross differentiating to give the fourth-order equation

$$\frac{\delta}{Re_j}\nabla^4\Psi = \nabla^2\Psi_t + u\nabla^2\Psi_x - u_{yy}\Psi_x + u_{xy}\Psi_y$$

$$+ v\nabla^2\Psi_y - v_{xx}\Psi_y + v_{xy}\Psi_x \,. \qquad (3.2b)$$

The disturbance equations in the suspension are derived in an analogous fashion to give

$$\rho_o\left[\Phi_{yt} + u^s\Phi_{yx} + u^s_x\Phi_y - u^s_y\Phi_x + v^s\Phi_{yy}\right] = -\frac{1}{\delta}p^{s\prime}_x + \frac{\delta}{Re_j}\,\mu_o\nabla^2\Phi_y \,, \qquad (3.3a)$$

and

$$\frac{\delta}{Re_j}\,\frac{\mu_o}{\rho_o}\nabla^4\Phi = \nabla^2\Phi_t + u^s\nabla^2\Phi_x - u^s_{yy}\Phi_x + u^s_{xy}\Phi_y$$

$$+ v^s\nabla^2\Phi_y - v^s_{xx}\Phi_y + v^s_{xy}\Phi_x \,. \qquad (3.3b)$$

The equations (3.2a) and (3.3a) are retained in order to evaluate the disturbance pressures, which, as we shall see below, are needed in the normal stress balance.

It turns out to be more convenient to transfer the origin of the coordinates so that it lies at the position of the unperturbed interface (see Fig. 10). In addition, the wavelength of the disturbance, ℓ_x, is chosen to be much smaller than the characteristic distance over which the base flow varies in the streamwise direction. Thus, disturbance variations in the streamwise direction occur over a "fast" length scale and do not see the corresponding "slow", streamwise base flow changes. This establishes the asymptotic structure through which the higher order terms of the base flow are introduced. We define the fast variable as $\hat{x} = x/\ell_x$ and a corresponding stretched time as $\hat{t} = t/\ell_x$. We also define the rescaled transverse variable*

$$\bar{y} = \frac{y}{\delta b(x)} - 1 \ , \tag{3.4}$$

and the coordinate transformation may then be represented as, $(x,y,t) \rightarrow (x,\hat{x},\bar{y},\hat{t})$ where the derivatives are given by

$$\frac{\partial}{\partial x} = \frac{\partial}{\partial x} + \frac{1}{\ell_x}\frac{\partial}{\partial \hat{x}} - (\bar{y}+1)\frac{b'}{b}\frac{\partial}{\partial \bar{y}} \ ,$$

*Note that $\bar{y}$ is not the same variable defined in Chapter 2.

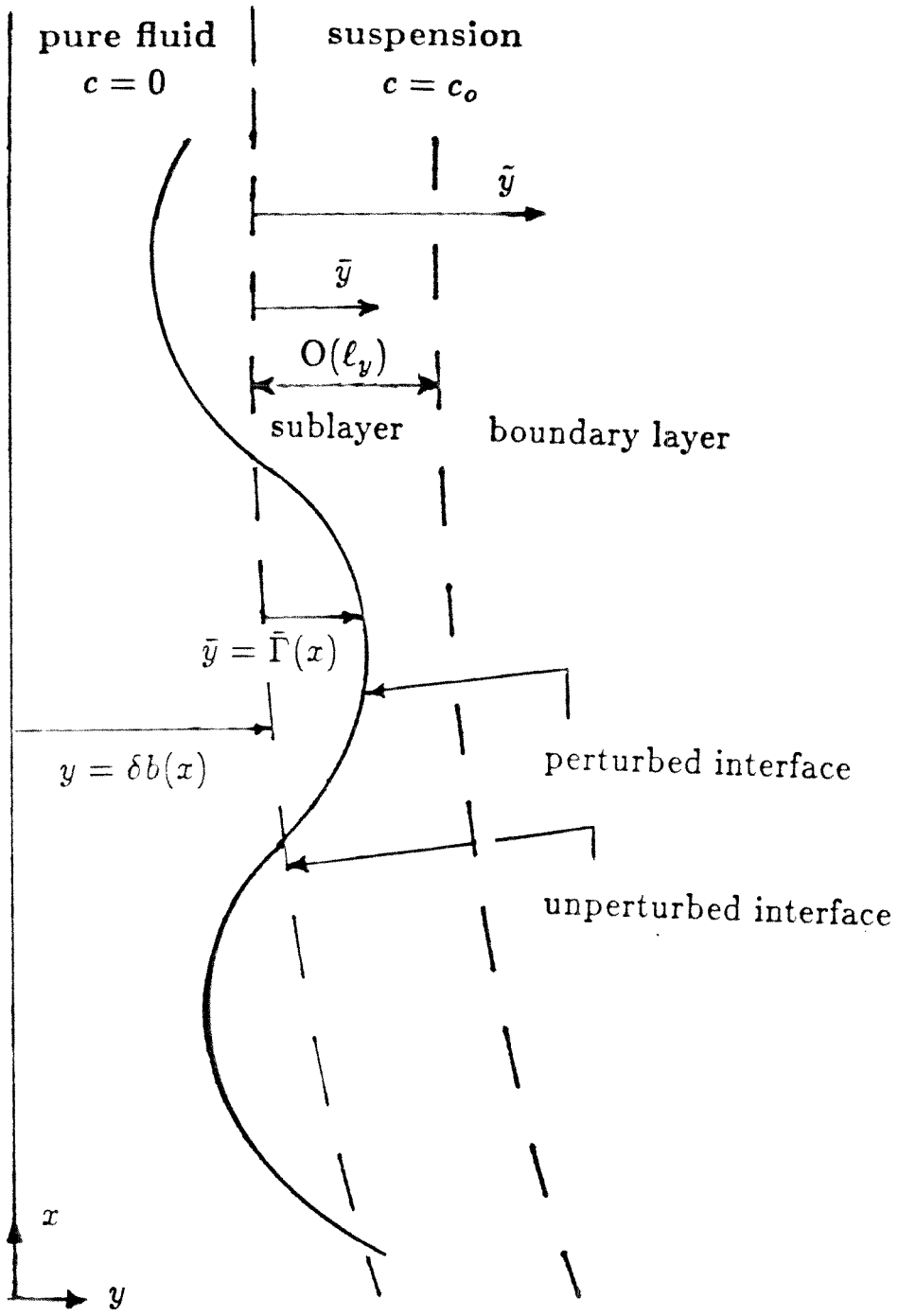

Figure 10 Definition of the variables used in the linear stability analysis.

$$\frac{\partial}{\partial y} = \frac{1}{\delta b} \frac{\partial}{\partial \bar{y}} ,$$

and

$$\frac{\partial}{\partial t} = \frac{u_c}{\ell_x} \frac{\partial}{\partial \hat{\tau}} .$$

Using these transformations, the equations may be rewritten in the new coordinates:

$$\Psi_{\bar{y}\bar{y}\bar{y}\bar{y}} + 2(\frac{\delta b}{\ell_x})^2 \Psi_{\hat{x}\hat{x}\bar{y}\bar{y}} + (\frac{\delta b}{\ell_x})^4 \Psi_{\hat{x}\hat{x}\hat{x}\hat{x}} = \frac{Re_j \delta b^2}{\ell_x} \left[\Psi_{\hat{\tau}\bar{y}\bar{y}}\right.$$

$$\left. + (\frac{\delta b}{\ell_x})^2 \Psi_{\hat{\tau}\hat{x}\hat{x}} + u(\Psi_{\bar{y}\bar{y}\hat{x}} + (\frac{\delta b}{\ell_x})^2 \Psi_{\hat{x}\hat{x}\hat{x}}) - u_{\bar{y}\bar{y}}\Psi_{\hat{x}}\right] + O(\delta Re_j, \frac{\delta^2}{\ell_x}) , \tag{3.5a}$$

and

$$\frac{\partial p'}{\partial \hat{x}} = \frac{\ell_x}{Re_j \delta b^3} \left[\Psi_{\bar{y}\bar{y}\bar{y}} + (\frac{\delta b}{\ell_x})^2 \Psi_{\hat{x}\hat{x}\bar{y}}\right]$$

$$- \frac{1}{b} \left[\Psi_{\hat{\tau}\bar{y}} + u\Psi_{\hat{x}\bar{y}} - u_{\bar{y}}\Psi_{\hat{x}} + O(\ell_x, \frac{\delta}{Re_j})\right] \tag{3.5b}$$

The equations governing the disturbance flow in the suspension are derived in the same way as for the pure fluid, the only difference being that the suspension streamfunction depends on the transverse variable

$$\hat{y} = \frac{y-\delta b}{\ell_y b} ,$$

where ℓ_y (i.e., the sublayer thickness) is the scaling of the

suspension region where viscosity is important. These equations are then given by

$$\Phi_{\hat{y}\hat{y}\hat{y}\hat{y}} + 2\left(\frac{\ell_y b}{\ell_x}\right)^2 \Phi_{\hat{x}\hat{x}\hat{y}\hat{y}} + \left(\frac{\ell_y b}{\ell_x}\right)^4 \Phi_{\hat{x}\hat{x}\hat{x}\hat{x}} = \frac{Re_j \ell_y^2 b^2}{\delta \ell_x} \frac{\rho_o}{\mu_o}\Big[\Phi_{\hat{\tau}\hat{y}\hat{y}}$$

$$+ \left(\frac{\ell_y b}{\ell_x}\right)^2 \Phi_{\hat{\tau}\hat{x}\hat{x}} + u^s\left(\Phi_{\hat{y}\hat{y}\hat{x}} + \left(\frac{\ell_y b}{\ell_x}\right)^2 \Phi_{\hat{x}\hat{x}\hat{x}}\right) - \left(\frac{\ell_y}{\Delta}\right)^2 u^s_{\tilde{y}\tilde{y}} \Phi_{\hat{x}}\Big] + O\left(\frac{\ell_y^2}{\delta}, \frac{\ell_y^2}{\ell_x}\right), \tag{3.6a}$$

and

$$\frac{\partial p^{s'}}{\partial \hat{x}} = \frac{\delta^2 \ell_x}{Re_j \ell_y^3 b^3} \mu_o\Big[\Phi_{\hat{y}\hat{y}\hat{y}} + \left(\frac{\ell_y b}{\ell_x}\right)^2 \Phi_{\hat{x}\hat{x}\hat{y}}\Big]$$

$$- \frac{\delta}{\ell_y b} \rho_o\Big[\Phi_{\hat{\tau}\hat{y}} + u^s \Phi_{\hat{x}\hat{y}} - \frac{\ell_y}{\Delta} u^s_{\tilde{y}} \Phi_{\hat{x}} + O\left(\ell_x, \frac{\ell_y^2}{\ell_x}\right)\Big]. \tag{3.6b}$$

The boundary conditions require that both components of the disturbance velocity must vanish far away from the jet, i.e.,

$$\Phi, \Phi' \to 0 \quad \text{as} \quad y \to \pm \infty .$$

However, since the equations are linear in the disturbance streamfunction (and we shall see that this is also true for the boundary conditions), the solution may be decomposed into a linear combination of symmetrical and antisymmetrical components. The boundary conditions at infinity then may be replaced by

$$\Phi = \Phi' \to 0 \quad \text{as} \quad y \to \infty$$

along with the conditions at the centerline

for antisymmetric disturbances

$$\Psi' = \Psi''' = 0 \quad \text{at} \quad \bar{y} = -1 \ , \tag{3.7a}$$

or for symmetric disturbances

$$\Psi = \Psi'' = 0 \quad \text{at} \quad \bar{y} = -1 \ . \tag{3.7b}$$

Hence, we only need to consider the positive half plane, i.e., $y > 0$. The remaining boundary conditions arise from matching conditions at the interface. More specifically, at the perturbed position of the interface, given by $\bar{y} = \bar{\Gamma}$, the velocity and stress must be continuous. However, as is consistent with the linear analysis, it is more convenient to transfer the matching conditions to the unperturbed position. For example, continuity of the tangential velocity requires

$$u + \delta\Psi_y = u^S + \delta\Phi_y \qquad \bar{y} = \bar{\Gamma} \ .$$

This condition is simplified using a Taylor series expansion about $\bar{y} = 0$ for each term, and linearizing in the perturbation quantities to give

$$u + \delta\Psi_y + \frac{\partial u}{\partial \bar{y}}\Big|_o \bar{\Gamma} = u^S + \delta\Phi_y + \frac{\partial u^S}{\partial \bar{y}}\Big|_o \bar{\Gamma} \quad \text{at} \quad \bar{y} = 0 \ .$$

Since the base flow tangential velocities are equal at the

unperturbed interface position, and the derivatives are related by the base flow shear stress condition (2.17d), this condition further simplifies to

$$\Psi_{\bar{y}} = \frac{\delta}{\ell_y}\,\Phi_{\hat{y}} + \frac{\delta}{\Delta}\,(1-\mu_o)\frac{\partial u^s}{\partial \bar{y}}\Big|_o\, b\bar{\Gamma} \qquad \text{at} \quad \bar{y} = 0\ . \tag{3.7c}$$

Continuity of the normal velocity component at the interface requires

$$\delta\bar{v} - \frac{\delta}{\ell_x}\,\Psi_{\hat{x}} - \delta\left[\Psi_x - (\bar{y}+1)\frac{b'}{b}\,\Psi_{\bar{y}}\right] = \Delta\bar{v}^s - \frac{\delta}{\ell_x}\,\Phi_{\hat{x}} - \delta\left[\Phi_x - (\hat{y} + \frac{\delta}{\ell_y})\frac{b'}{b}\,\Phi_{\hat{y}}\right] \qquad \text{at} \quad \bar{y} = \bar{\Gamma}\ ,$$

where $\bar{v}(x,\bar{y})$ and $\bar{v}^s(x,\bar{y})$ represent the rescaled base flow velocities in the pure fluid and suspension respectively. Transferring this condition to $\bar{y} = 0$ and subtracting out the base flow normal velocity condition gives

$$\Psi_{\hat{x}} + \ell_x\left[\Psi_x - (\bar{y}+1)\frac{b'}{b}\,\Psi_{\bar{y}}\right] - \ell_x\left(\frac{\partial\bar{v}}{\partial\bar{y}}\Big|_o - \frac{\partial\bar{v}^s}{\partial\bar{y}}\Big|_o\right)\bar{\Gamma} = \Phi_{\hat{x}} + \ell_x\left[\Phi_x - (\hat{y} + \frac{\delta}{\ell_y})\frac{b'}{b}\,\Phi_{\hat{y}}\right] \qquad \text{at } \bar{y} = 0\ .$$

This may be further simplified by using the base flow continuity equation and the result in (3.7c) to give

$$\Psi_{\hat{x}} = \Phi_{\hat{x}} + \ell_x(\Phi_x - \Psi_x) \qquad \text{at} \quad \bar{y} = 0\ . \tag{3.7d}$$

The boundary conditions also require that the stress is continuous at the interface. If we represent the disturbance stress tensor as $\underline{\underline{\sigma}}'$, and the normal vector to the perturbed interface as $\vec{n} + \vec{n}'$, the normal stress balance may be written as

$$(\vec{n} + \vec{n}') \cdot [\underline{\underline{\sigma}} + \underline{\underline{\sigma}}']_j \cdot (\vec{n} + \vec{n}') = 0 \qquad \text{at } \bar{y} = \bar{\Gamma} \ ,$$

where $[\ ]_j$ denotes the jump across the interface. Transferring this condition to $\bar{y} = 0$ in the same way as before, subtracting off the base flow condition, and linearizing in the disturbance quantities gives

$$\vec{n} \cdot \underline{\underline{\Sigma}} \cdot \vec{n} = 0 \qquad \text{at } \bar{y} = 0 \ ,$$

where

$$\underline{\underline{\Sigma}} = \left[\underline{\underline{\sigma}}' + \frac{\partial \underline{\underline{\sigma}}}{\partial \bar{y}} \Big|_0 \bar{\Gamma} \right]_j \ ,$$

and

$$\vec{n} = -\delta \frac{\partial b}{\partial x} \vec{i} + \vec{j}$$

is the normal vector to the unperturbed interface written in terms of the cartesian coordinate unit vectors. The leading order term in this balance requires that $\Sigma_{22} = 0$, or equivalently

$$[p']_j + \frac{\delta}{Re_j \ell_x b} 2(\Psi_{\hat{x}\bar{y}} - \frac{\delta}{\ell_y} \mu_0 \Phi_{\hat{x}\hat{y}}) = 0 + O(\frac{\delta}{Re_j}) \qquad \text{at } \bar{y} = 0 \ . \quad (3.7e)$$

The fact that the base flow pressure does not contribute to the

stability problem at leading order (cf. 3.5 - 3.7) reflects the result found in Chapter 2 that the pressure field is constant, and the flow is driven by buoyancy.

The tangential stress condition is derived in a similar manner and to leading order gives

$$\Sigma_{12} = 0 \ ,$$

or

$$\Psi_{\bar{y}\bar{y}} - \mu_o\left(\frac{\delta}{\ell_y}\right)^2 \Phi_{\hat{y}\hat{y}} + \left[u_{\bar{y}\bar{y}} - \left(\frac{\delta}{\Delta}\right)^2 \mu_o u^s_{\bar{y}\bar{y}}\right] b\bar{\Gamma}$$

$$- \left(\frac{\delta b}{\ell_x}\right)^2 \left(\Psi_{\hat{x}\hat{x}} - \mu_o \Phi_{\hat{x}\hat{x}}\right) + O\left(\frac{\delta^2}{\ell_x}\right) = 0 \qquad \text{at} \quad y = 0 \ . \tag{3.7f}$$

The final boundary condition which must be formulated is the kinematic condition. In the original non-dimensional, coordinate system, i.e., (x,y,t), this is written as

$$\frac{\partial}{\partial t}\left[y - \delta b(1+\bar{\Gamma})\right] + \left[u - \frac{u_o}{u_c} f(c) + \delta \Psi_y\right] \frac{\partial}{\partial x}\left[y - \delta b(1+\bar{\Gamma})\right]$$

$$+ (v - \delta \Psi_x) \frac{\partial}{\partial y}\left[y - \delta b(1+\bar{\Gamma})\right] = 0 \qquad \text{at} \quad y = \delta b(1+\bar{\Gamma}) \ .$$

Following the usual steps to transfer this condition to $\bar{y} = 0$, and subtracting out the base flow kinematic condition gives

$$b\left[\bar{\Gamma}_{\hat{t}} + u\bar{\Gamma}_{\hat{x}}\right] + \Psi_{\hat{x}} + O(\ell_x) = 0 \qquad \text{at} \quad \bar{y} = 0 \ . \tag{3.7g}$$

We wish to analyze the growth or decay of infinitesimal disturbances governed by the set of linear partial differential equations in (3.5) and (3.6), together with the boundary and matching conditions in (3.7) for the base flow of Case I. The linearity of the problem allows any arbitrary disturbance to be expressed as a superposition of normal mode solutions. Thus, we assume that the perturbation variables take the form

$$\begin{Bmatrix} \bar{\Gamma}(x,\hat{x},\hat{\tau}) \\ \Psi(x,\hat{x},\bar{y},\hat{\tau}) \\ \Phi(x,\hat{x},\hat{y},\hat{\tau}) \\ p'(x,\hat{x},\bar{y},\hat{\tau}) \\ p^{s'}(x,\hat{x},\hat{y},\hat{\tau}) \end{Bmatrix} = \begin{Bmatrix} \frac{1}{b}\,\eta(x,\hat{\tau}) \\ \psi(x,\bar{y}) \\ \phi(x,\hat{y}) \\ P(x,\bar{y}) \\ P^{s}(x,\hat{y}) \end{Bmatrix} \exp\{i[g(\hat{x}) - \hat{\omega}\hat{\tau}]\} \qquad (3.8a)$$

where $\hat{\omega}$ is the scaled frequency which is assumed to be real, and the complex scaled wavenumber, given by

$$\frac{dg}{d\hat{x}} \equiv \hat{\alpha}(x,\hat{\tau}) \qquad (3.8b)$$

is a function of the slow variable only. Hence the imaginary component of the wavenumber determines whether a disturbance will grow or decay, where $\hat{\alpha}_I > 0$ represents a stable wave. The spatial analysis was chosen over a temporal analysis based on physical grounds since spatial growth is the true situation observed in experiments.

Using the normal mode solution form, the problem is reduced to an eigenvalue problem for the eigenfunctions ψ (in the pure fluid) and ϕ (in the suspension) with $\hat{\alpha}$ as the complex eigenvalue. The function $\eta(x,\hat{t})$ represents the unknown position of the perturbed interface, and is related to the streamfunction ψ through the kinematic condition

$$\eta = \frac{\hat{\alpha}\psi}{\hat{\omega}-\hat{\alpha}u} \ . \tag{3.9}$$

The functions P and P^S in (3.8a) are needed to calculate the difference in the disturbance pressure at the unperturbed interface for the normal stress condition. From (3.5b) and (3.6b) we obtain

$$i\hat{\alpha}P' = \frac{\ell_x}{Re_j\delta b^3}\left[\psi''' - \left(\frac{\delta}{\ell_x}\right)^2 (b\hat{\alpha})^2\psi'\right] + \frac{i}{b}\left[(\hat{\omega}-\hat{\alpha}u)\psi' + \hat{\alpha}u_{\bar{y}}\psi\right] + O\left(\ell_x, \frac{\delta}{Re\ell_j}\right) \tag{3.10a}$$

and

$$i\hat{\alpha}P^{S'} = \frac{\delta^2\ell_x}{Re_j\ell_y^3 b^3}\mu_o\left[\phi''' - \left(\frac{\ell_y}{\ell_x}\right)^2 (b\hat{\alpha})^2\phi'\right] + \frac{i\delta}{\ell_y b}\rho_o\left[(\hat{\omega}-\hat{\alpha}u^S)\phi' + \frac{\ell_y}{\Delta}\hat{\alpha}u^S_{\bar{y}}\phi\right] + O\left(\ell_x, \frac{\delta\ell_x}{\ell_y}\right) \ . \tag{3.10b}$$

The primes on the streamfunctions shall be used to denote derivatives taken with respect to the appropriate transverse coordinate. In order to simplify the x-dependence of the equations,

the following variables are defined

$$U = \frac{u}{u_o} , \qquad U^s = \frac{u^s}{u_o} ,$$

(3.11a)

$$\alpha = b\hat{\alpha} , \qquad \omega = \frac{b}{u_o}\hat{\omega}, \qquad R = bu_oRe_j = Re_j\{1 + O(\varepsilon)\} ,$$

where

$$u_o = \frac{1}{b}\left[1 - \varepsilon\frac{b^3}{3} - \varepsilon^2\frac{1}{3}\frac{db}{dx}\right] \tag{3.11b}$$

is the base flow velocity at the unperturbed interface. The final form of the governing equations and boundary conditions is then determined by substituting (3.8) and (3.11) into equations (3.5) - (3.7) to give

$$\psi^{iv} - 2(\frac{\delta}{\ell_x})^2\alpha^2\psi'' + (\frac{\delta}{\ell_x})^4\alpha^4\psi = - i\frac{R\delta}{\ell_x}\left[(\omega-\alpha U)(\psi'' - (\frac{\delta}{\ell_x})^2\alpha^2\psi)\right.$$

(3.12)

$$\left. + \alpha U_{\bar{y}\bar{y}}\psi + O(\ell_x)\right] + O(\frac{\delta^2}{\ell_x}) ,$$

and

$$\phi^{iv} - 2(\frac{\ell_y}{\ell_x})^2\alpha^2\phi + (\frac{\ell_y}{\ell_x})^4\alpha^4\phi = - i\frac{R\ell_y^2}{\delta\ell_x}\frac{\rho_o}{\mu_o}\left[(\omega-\alpha U^s)(\phi'' - (\frac{\ell_y}{\ell_x})^2\alpha^2\phi)\right.$$

(3.13)

$$\left. + (\frac{\ell_y}{\Delta})^2\alpha U^s_{\bar{y}\bar{y}}\phi\right] + O(\frac{\ell_y^2}{\ell_x}) ,$$

with the boundary conditions for the antisymmetric disturbance

$$\psi'(-1) = \psi'''(-1) = 0 \ , \tag{3.14a}$$

or for the symmetric disturbance

$$\psi(-1) = \psi''(-1) = 0 \ , \tag{3.14b}$$

together with the conditions at infinity

$$\phi, \phi' \to 0 \quad \text{as} \quad y \to \infty \ , \tag{3.14c}$$

and the matching condtions at $\bar{y} = 0$

$$\psi = \phi = 1 \ , \tag{3.14d}$$

$$\psi' = \frac{\delta}{\ell_y}\,\phi' + \frac{\delta}{\Delta}\,(1-\mu_o)\frac{\alpha}{\omega-\alpha}U^S_{\tilde{y}} \ , \tag{3.14e}$$

$$\begin{aligned}\psi''' = {} & \left(\frac{\delta}{\ell_y}\right)^3 \mu_o\phi''' + \left(\frac{\delta}{\ell_x}\right)^2 3\alpha^2\left(\psi' - \frac{\delta}{\ell_y}\,\mu_o\phi'\right) \\ & - i\frac{R\delta}{\ell_x}\left[(\omega-\alpha)\left(\psi' - \frac{\delta}{\ell_x}\,\rho_o\phi'\right) + \frac{\delta}{\Delta}\,(\mu_o-\rho_o)\alpha U^S_{\tilde{y}}\right] \ ,\end{aligned} \tag{3.14f}$$

$$\frac{\omega-\alpha}{\alpha}\left(\psi'' - \left(\frac{\delta}{\ell_y}\right)^2\mu_o\phi''\right) = -\frac{\delta}{\Delta}\left(\overline{U_{\bar{y}\bar{y}}} - \frac{\delta}{\Delta}\mu_o U^S_{\tilde{y}\tilde{y}}\right) - \left(\frac{\delta}{\ell_x}\right)^2(1-\mu_o)\alpha(\omega-\alpha) \ , \tag{3.14g}$$

where the base flow shear stress derivative with the overbar in (3.14g), has been rescaled so that it is now O(1). Since any multiple of an eigenfunction solution is also a solution, the normal velocity

condition (3.14d) has been used to set this arbitrary constant. Finally, the normalized base flow velocities

$$U = \frac{u}{u_o} = 1 - \varepsilon\left(\frac{1}{2}\bar{y}^2 + \bar{y}\right)\left[b^3 + \varepsilon\left(\frac{b^6}{3} + \frac{db}{dx}\right)\right] + O(\varepsilon^3) \qquad (3.15a)$$

and

$$U^S = \frac{u^S}{u_o} = \frac{F'(\eta)}{F'(o)} + O(\varepsilon) \qquad (3.15b)$$

have been used to evaluate $U(0) = U^S(0) = 1$.

The governing stability equations for the pure fluid and suspension for the nearly parallel base flow soluton of Case I have been rewritten in an asymptotic framework using the disturbance wavelength as the expansion parameter. The leading order equation in each region is the same as for a parallel flow, i.e., the Orr-Sommerfeld equation, with the nonparallel error terms of $O(\ell_x)$. In the asymptotic limit, the error terms are small, and the Orr-Sommerfeld equation is a good approximation. The problem is now reduced to an eigenvalue problem for the complex eigenvalue α, and the eigenfunctions Ψ and Φ. Hence for a given set of physical properties of the system, i.e., b_o, Re_j, Gr_j, μ_o and ρ_o, and for a disturbance frequency $\omega(x,\hat{\omega})$, the equations (3.12) - (3.14) can only be satisfied at certain values of α, and the sign of α_I then determines whether disturbances will locally grow or decay. As we shall see below, the disturbances with the maximum growth rates, and consequently the ones of interest to us, lie in the range of wavelengths that are of the same order of magnitude as the sublayer

thickness, i.e., $\ell_x \sim \ell_y$.

In contrast with the governing equations for the stability of a pure fluid plume, the jet Reynolds number appears as a parameter of the problem, and represents the rate at which buoyancy is fed into the flow. In addition, although the flow is buoyancy driven, there is no explicit dependence on the jet Grashof number in the governing equations because of the assumption that there is no perturbation in the concentration. Instead, it affects the disturbance flow through the base flow velocity profiles and scalings. In particular, we shall see that the difference in the shear stress derivatives at the interface, i.e., $U_{yy}|_o$ and the asymptotically small scaling ratio of the thicknesses of the base flow regions, i.e., $\varepsilon = \frac{\delta}{\Delta} << 1$, are important features of this stability problem which are caused by buoyancy.

3.3 Solutions to the Disturbance Equations

3.3a Long Wavelength Disturbances

Antisymmetric Disturbances

Let us first investigate the solution to the equations (3.12) - (3.14) for antisymmetric disturbances with asymptotic wavelengths that are large compared to the pure fluid thickness, i.e., assume

$$\delta << \ell_x << 1 \tag{3.16a}$$

and

$$R\frac{\delta}{\ell_x}(\omega-\alpha U)\psi'' << 1 , \tag{3.16b}$$

where $R \sim O(Re_j)$ is defined in (3.11). In this case, the leading order disturbance equation for the pure fluid region is purely viscous,

$$\psi^{iv} = \left(\frac{\delta}{\ell_x}\right)^2 2\alpha^2\psi'' - iR\frac{\delta}{\ell_x}\left[(\omega-\alpha U)\psi'' + \alpha U_{\bar{y}\bar{y}}\psi\right] \tag{3.17}$$

$$+ iR\left(\frac{\delta}{\ell_x}\right)^3 (\omega-\alpha U)\alpha^2\psi - \left(\frac{\delta}{\ell_x}\right)^4\alpha^4\psi + O\left(\delta R, \frac{\delta^2}{\ell_x}\right) .$$

Integrating the homogeneous equation four times and applying the centerline and normalization conditions (3.14a and d) results in the solution

$$\psi = 1 + a_1\left(\frac{1}{2}\bar{y}^2 + \bar{y}\right) - \frac{1}{6}\psi_p'''(-1)\left(\bar{y}^3 - 3\bar{y}\right) - \psi_p'(-1)\bar{y} + \psi_p(\bar{y}) , \tag{3.18a}$$

where $\psi_p(\bar{y}) < O(1)$ is a particular solution of equation (3.17). The remaining integration constant is determined from the tangential velocity condition at the interface and is given by

$$a_1 = \left(\frac{\delta}{\ell_y}\right)\phi'(0) + \frac{\delta}{\Delta}\left(1-\mu_o\right)\frac{\alpha}{\omega-\alpha}U_{\bar{y}}^s\Big|_o . \tag{3.18b}$$

If the scaling of the derivative of the suspension streamfunction is such that $\phi'(0) \leq O(\ell_y/\delta)$, and additionally if $(\omega-\alpha) > O(\delta/\Delta)$, the leading order term in the streamfunction for the pure fluid disturbance is just a constant $\psi = 1$, and hence the streamwise disturbance velocity in the pure fluid, given by $\psi' \sim a_1$, is of a smaller order. Substituting the pure fluid solution (3.18)

into the shear stress condition (3.14g) gives the eigenvalue condition,

$$\frac{\omega-\alpha}{\alpha} = -\frac{\ell_y}{\Delta}\,\frac{\overline{U_{\bar{y}\bar{y}}} + (1-\mu_o)U^s_{\bar{y}} - \frac{\delta}{\Delta}\,\mu_o U^s_{\bar{y}\bar{y}}}{\phi' - \left(\frac{\delta}{\ell_y}\right)\mu_o\phi'' + \frac{\delta\ell_y}{\ell_x^2}\,\alpha^2(1-\mu_o)} \qquad \text{at } \bar{y} = 0\ . \tag{3.19}$$

Note that the eigenvalue α depends on the difference in the shear stress derivatives of the base flow in the pure fluid and the suspension. This difference is caused by the buoyancy force and we shall soon see that it results in the flow becoming unstable for disturbances in a certain range of wavelengths. At leading order the eigenvalue is real, and hence the disturbance is neutrally stable. However, the difference in the U_{yy} terms at the interface allows energy to be transferred from the base flow to the disturbance flow and results in unstable disturbances.

As we shall show below, the sublayer thickness is much smaller than the boundary layer thickness, i.e.,

$$\frac{\ell_y}{\Delta} \ll 1\ , \tag{3.20}$$

provided $\ell_x \ll 1$. Thus, if we assume the expansion

$$\alpha = \alpha_o\,[1 + \alpha_1 + \alpha_2 + \ldots]\ , \tag{3.21a}$$

then from (3.19) the leading order eigenvalue is given by

$$\alpha_o = \omega \ , \tag{3.21b}$$

provided that the suspension stream function derivatives are scaled correctly, and $\phi'(0) \neq 0$. Since the frequency ω is real, the leading order disturbance behavior is neutrally stable, and the wave speed of the disturbance, which is defined in terms of the real component of the wavenumber, $c_w = \omega/\alpha_r = 1$, is the same as the base flow interfacial velocity. This is not surprising since in the leading order equations the base flow velocity is a constant, i.e., 1, and hence there is no interaction with the disturbance. In other words, a disturbance placed on a uniform velocity field neither grows nor decays, but instead, propagates with the flow at the same constant velocity.

In order to check the assumptions that we made in deriving these results (cf. 3.20 and 3.16b), we need to determine the thickness of the sublayer region, i.e., that region in the suspension where viscous effects are important. Using the scaling result from the eigenvalue condition (3.19), we set

$$(\omega-\alpha) = \frac{\ell_y}{\Delta}\,(\overline{\omega-\alpha}) = -\frac{\ell_y}{\Delta}\,\omega\tilde{\alpha}_1 + O(\alpha_2) \ , \tag{3.22}$$

where $(\overline{\omega-\alpha})$ and $\tilde{\alpha}_1$ represent O(1) quantities. In addition, the suspension base flow velocity in the sublayer is represented by a Taylor series about $\tilde{y} = 0$. In terms of the sublayer variables this becomes

$$U^S = 1 + \frac{\ell_y}{\Delta} U^S_{\hat{y}}|_o \hat{y} + \frac{\ell_y}{\Delta} U^S_{\hat{y}\hat{y}}|_o \frac{\hat{y}^2}{2} ,$$

which along with (3.22) is substituted into (3.13), the disturbance equation for the suspension region, to determine the size of its leading order inertial term

$$R\frac{\ell_y^2}{\delta \ell_x} \frac{\rho_o}{\mu_o}(\omega - \alpha U^S) = -R\frac{\ell_y^3}{\Delta \delta \ell_x} \frac{\omega}{\nu_o}(\tilde{\alpha}_1 + U^S_{\hat{y}}|_o \hat{y}) . \qquad (3.23)$$

Hence for the leading order inertial and viscous terms to be balanced, the sublayer thickness must scale as

$$\ell_y \sim \nu_o \frac{\Delta \delta \ell_x}{R} \sim \frac{\varepsilon}{Re_j} (\nu_o \ell_x)^{1/3} , \qquad (3.24a)$$

where the scalings for Δ and δ are determined in the base flow solution (cf. 2.17) and

$$\varepsilon \sim \left[\frac{b_o^3 Re_j^2}{Gr_j}\right]^{1/5} \qquad (3.24b)$$

is an asymptotically small parameter.

The ratio of the sublayer and boundary layer thicknesses can now be written as

$$\frac{\ell_y}{\Delta} \sim (\nu_o \ell_x)^{1/3} , \tag{3.24c}$$

which is small since the analysis applies for asymptotically small wavelengths. Hence, viscous effects in the disturbance flow in the suspension are confined to a very small region adjacent to the interface. We can also use the scaling result in (3.22) to show that the leading order inertial term in the stability equation for the pure fluid region is of the order

$$R\frac{\delta}{\ell_x} (\omega-\alpha U)\psi'' \sim \frac{\varepsilon\delta}{\ell_x} \tilde{\alpha}_1 \phi'(0) ,$$

which is small since $\delta/\ell_x << 1$ (cf. 3.16a). Hence in this region, the disturbance flow is dominated by viscous forces and the inertial effects occur at a smaller order ~ $o(\varepsilon^3/Re_j\ell_x)$.

The homogeneous solution for ψ is now specified in terms of the streamfunction in the suspension ϕ. However we need the leading order term of the particular solution as well, to evaluate the $\psi'''(0)$ term in the normal stress condition. This leading order term is governed by the equation

$$\psi_p^{iv} = \frac{\delta^3}{\ell_x^2 \ell_y} \left[2\alpha^2(\phi'(0) - (1-\mu_o)\frac{1}{\tilde{\alpha}_1} U_{\tilde{y}}^s|_o) + R\frac{\ell_x}{\Delta} i\omega\tilde{\alpha}_1\mu_o\phi''(0) \right] ,$$

for which the solution is given by

$$\psi_p = \frac{\delta^3}{\ell_x^2 \ell_y}\left[2\alpha^2(\phi'(0) + (1-\mu_o)\frac{1}{\tilde{\alpha}_1}U^s_{\tilde{y}}|_o) - \frac{R(\ell_x)}{\Delta}\, i\omega\tilde{\alpha}_1\mu_o\phi''(0)\right]\frac{\bar{y}^4}{24} .$$

The normal stress condition (3.14f) then becomes

$$\mu_o\phi''' + \left[i\nu_o(1-\rho_o)\omega\tilde{\alpha}_1 + (\frac{\ell_y}{\ell_x})^2\,\alpha^2(1-3\mu_o)\right]\phi'$$

$$- \left[i\nu_o(1-\rho_o)\omega\tilde{\alpha}_1 + (\frac{\ell_y}{\ell_x})^2\,\alpha^2(1-\mu_o)\right]\tilde{\alpha}_1 U^s_{\tilde{y}} = 0 + O(\frac{\ell_y^2}{\ell_x\Delta}) \qquad \text{at } \bar{y} = 0 . \tag{3.25}$$

In order to determine the suspension solution, we first rewrite the sublayer equation as

$$(\phi''-\bar{\alpha}^2\phi'')'' - \left[\bar{\alpha}^2 + i\omega U^s_{\tilde{y}}|_o(\frac{\tilde{\alpha}_1}{U^s_{\tilde{y}}|_o} + \hat{y})\right](\phi''-\bar{\alpha}^2\phi) = -\frac{\ell_y}{\Delta} i\alpha U^s_{\tilde{y}\tilde{y}}\phi . \tag{3.26a}$$

where

$$\bar{\alpha} = (\frac{\ell_y}{\ell_x})\alpha . \tag{3.26b}$$

Substituting in for ϕ and $\hat{y}$ using

$$u(z) = \phi'' - \bar{\alpha}^2\phi , \qquad \text{and} \qquad z = z_o + m\hat{y} , \tag{3.27a}$$

where

$$z_o = \left(\frac{\bar{\alpha}}{m}\right)^2 + \frac{m\tilde{\alpha}_1}{U^s_{\tilde{y}}|_o} , \qquad \text{and} \qquad m = (i\omega U^s_{\tilde{y}}|_o)^{1/3} , \tag{3.27b}$$

transforms equation (3.26a) into the inhomogeneous Airy equation

$$u'' - zu = - \frac{\ell_y}{\Delta} \frac{i\alpha}{m^2} U^s_{\tilde{y}\tilde{y}}\phi . \tag{3.28a}$$

It turns out that the leading order imaginary component of the wavenumber can be determined from the solution of the homogeneous Airy equation, and this solution is given by

$$u(z) = B_2 Ai(z) + B_3 Bi(z) . \tag{3.28b}$$

In order for ϕ' to decay at infinity, B_3 must vanish, and of the three possible values for m (cf. 3.27b) we must choose the one for which Ai(z) decays as $\hat{y} \to \infty$. This requires

$$m = \left(\frac{\omega}{\mu_o}\right)^{1/3} be^{-i\pi/6} . \tag{3.29}$$

Now that u(z) is known, applying the method of variation of parameters to (3.27a) yields

$$\phi = B_o e^{-\bar{\alpha}\hat{y}} + B_1 e^{\bar{\alpha}\hat{y}} + \frac{B_2}{2\bar{\alpha}} \left[e^{\bar{\alpha}\hat{y}} \int_0^{\hat{y}} Ai(z_o+m\eta)\, e^{-\bar{\alpha}\eta}\, d\eta \right.$$

$$\left. - e^{-\bar{\alpha}\hat{y}} \int_0^{\hat{y}} Ai(z_o+m\eta)\, e^{\bar{\alpha}\eta}\, d\eta \right] . \tag{3.30}$$

The remaining boundary conditions which must be satisfied are

$$\phi \to 0 \qquad \text{as } y \to \infty , \tag{3.31a}$$

$$\phi(0) = 1 , \tag{3.31b}$$

and the normal stress condition (3.25). Then with ϕ completely specified, the eigenvalue condition in (3.19) may be evaluated.

In order to apply the boundary condition at infinity, the size of the wavelength must be known. It turns out that the unstable disturbances have wavelengths the same size as the sublayer thickness, i.e., from (3.24a)

$$\ell_x \sim \ell_y \sim \nu_o^{1/2} \left(\frac{\varepsilon}{Re_j}\right)^{3/2} , \tag{3.32}$$

and the relevant scaling parameters are then given by

$$\frac{\delta}{\ell_y} \sim \left(\frac{\varepsilon Re_j}{\nu_o}\right)^{1/2}, \quad \frac{\ell_y}{\Delta} \sim \left(\nu_o \frac{\varepsilon}{Re_j}\right)^{1/2}, \quad \text{and} \quad \bar{\alpha} = \alpha \, . \tag{3.33a}$$

Then since ϕ must vanish outside of the sublayer region,

$$B_1 = - \frac{B_2}{2\alpha} I_1 \, , \tag{3.33b}$$

where

$$I_1 = \int_0^\infty Ai(z_o + m\eta)\, e^{-\omega\eta}\, d\eta + O\left(\nu_o \frac{\varepsilon}{Re_j}\right)^{1/2} . \tag{3.33c}$$

Applying the normalization condition gives

$$B_o = 1 + \frac{B_2}{2\alpha} I_1 \, . \tag{3.33d}$$

Finally, the remaining integration constant is found from the normal stress condition and is given by

$$B_2 = \frac{(1-2\mu_o)\omega^3 + i\nu_o(1-\rho_o)\omega^2\tilde{\alpha}_1}{\mu_o m\, Ai'(z_o) - [(1-2\mu_o)\omega^2 + i\nu_o(1-p_o)\omega\tilde{\alpha}_1]I_1}$$

$$+ \frac{U^s_y|_o}{\tilde{\alpha}_1} \frac{(1-\mu_o) + i\nu_o(1-\rho_o)\omega\tilde{\alpha}_1}{\mu_o m Ai'(z_o) - [(1-2\mu_o)\omega^2 + i\nu_o(1-\rho_o)\omega\tilde{\alpha}_1]I_1} \, . \tag{3.34}$$

Note that B_2, and consequently also $\phi'(0)$, are $O(1)$ and nonzero. Thus our earlier assumption that $(\omega-\alpha)$ is of order ℓ_y/Δ was justified.

The leading order streamfunctions in the pure fluid and suspension are now completely specified (cf. 3.33 and 3.34) and

substituting them into the eigenvalue condition (3.19) gives

$$-\left(\frac{\omega\tilde{\alpha}_1}{U^s_{\tilde{y}}|_0}+1\right)mAi'(z_0)=\omega^2 I_1=\omega^2\int_0^\infty Ai(z_0+m\eta)\,e^{-\omega\eta}\,d\eta\,. \qquad (3.35)$$

In this expression, the complex wavenumber, $\tilde{\alpha}_1$, is expressed as an implicit function of both the frequency and concentration (since $U^s_{\tilde{y}}|_0 = -b^3/\mu(c_0)$), but there is no dependence on the jet Reynolds number. Hence any disturbance that grows, will be unstable at all Reynolds numbers. In addition, since the argument of the Airy function depends on the wavenumber, (cf. 3.27) this equation must be solved by an iterative method. In Section 3.4, we shall eliminate the concentration dependence in the eigenvalue condition by defining new variables for the wavenumber and frequency. A numerical solution of the resulting eigenvalue condition then gives the reduced wavenumber β as a function of the reduced frequency s_0 only. These results are presented in Section 3.5.

Symmetric Disturbances

The solution procedure for symmetric disturbances follows analogously from that for the antisymmetric disturbances and hence will be only briefly summarized. The governing equations are identical to those for the antisymmetric disturbances, (i.e., 3.17 and 3.26), the only difference occuring in the centerline boundary conditions. Hence the streamfunction for the pure fluid region is found by integrating 3.17 four times and applying the centerline and

normalization conditions (cf. 3.14b and d) to give the solution

$$\psi = 1 + \bar{y} + a_3(\bar{y}^3 + 3\bar{y}^2 + 2\bar{y}) - \frac{1}{2}\psi_p''(-1)\,(\bar{y}^2 + \bar{y}) + \psi_p(-1)\bar{y} + \psi_p(\bar{y})\ .$$

The remaining integration constant is determined from the normal stress condition where

$$6a_3 = \frac{\varepsilon^3}{\ell_x}\,\rho_o\phi'''(0)$$

$$+ \frac{\varepsilon^3}{Re_j(\nu_o\ell_x^4)^{1/3}}\left[iR(1-\rho_o)\omega\tilde{\alpha}_1 + \frac{\varepsilon^2}{Re_j\ell_x}\,3\alpha^2(1-\mu_o)\right]\left[(\phi'(0) - \frac{1}{\tilde{\alpha}_1}U^s_{\bar{y}}|_o)\right] \qquad (3.36)$$

We shall see that the particular solution is small in magnitude, and does not contribute to the leading order amplification factor.

The leading order disturbance streamfunction in the suspension has the same general form as its antisymmetric counterpart given in equation (3.30). The boundary conditions which must be satisfied by the suspension streamfunction for the most unstable waves, i.e., where $\ell_x \sim \nu_o^{1/2}(\frac{\varepsilon}{Re_j})^{3/2}$, are

$$\phi \to 0 \quad \text{as } y \to \infty\ ,$$

$$\phi(0) = 1\ ,$$

and

$$\phi'(0) = \left(\frac{\nu_o}{\varepsilon Re_j}\right)^{1/2}\left[1 + O\left(\frac{\varepsilon Re_j}{\nu_o}\right)^{1/2}\right].$$

Substituting from (3.30) into these boundary conditions and solving for the integration constants gives

$$B_0 = -\left(\frac{\nu_o}{\varepsilon Re_j}\right)^{1/2}\left[\frac{1}{2\alpha} + O\left(\frac{\varepsilon Re_j}{\nu_o}\right)^{1/2}\right],$$

$$B_1 = \left(\frac{\nu_o}{\varepsilon Re_j}\right)^{1/2}\left[\frac{1}{2\alpha} + O\left(\frac{\varepsilon Re_j}{\nu_o}\right)^{1/2}\right],$$

$$B_2 = \left(\frac{\nu_o}{\varepsilon Re_j}\right)^{1/2}\left[-\frac{1}{I_1} + O\left(\frac{\varepsilon Re_j}{\nu_o}\right)^{1/2}\right],$$

where I_1 is given in (3.33c). The homogeneous solution for the streamfunction in the pure fluid is then completed by substituting the solution for ϕ into (3.36) to give

$$6a_3 = \frac{\varepsilon Re_j}{\nu_o}\left[\mu_o\left(\alpha^2 - \frac{mAi'(z_o)}{I_1}\right) + i\nu_o^{2/3}\omega\tilde{\alpha}_1(1-\rho_o) + 3\alpha^2(1-\mu_o) + O\left(\frac{\varepsilon Re_j}{\nu_o}\right)^{1/2}\right]$$

and from (3.17), the leading order particular solution is of the order $\psi_p \sim O(\varepsilon Re_j/\nu_o)^{3/2}$. The solutions for ψ and ϕ are then substituted into the tangential stress balance to give the eigenvalue condition

$$\frac{-\omega\tilde{\alpha}_i}{U^s_{\tilde{y}}|_o}\,Ai(z_o) + \alpha I_i = 0 \ . \tag{3.37}$$

As in the antisymmetric case the eigenvalue condition can not be solved analytically, since the argument of the Airy function depends on the eigenvalue $\tilde{\alpha}_i$. Hence in Section 3.4, we numerically solve this equation using an iteration procedure. However we will first complete this analysis in the next section by removing the long wavelength assumption in (3.16a) and investigating disturbances with wavelengths of the same order as the pure fluid thickness.

3.3b Short Wavelength Disturbances

Let us now investigate disturbances with short wavelengths,

$$\ell_x \sim \delta \sim \frac{\varepsilon^2}{Re_j} \ .$$

In contrast with the long wavelength analysis, the stability equation for the pure fluid now retains all of the viscous derivatives at leading order, i.e.,

$$\psi^{iv} - 2\alpha^2\psi'' + \alpha^4\psi = -iR[(\omega-\alpha U)(\psi''-\alpha^2\psi) + \alpha U_{\bar{y}\bar{y}}\psi] + 0\,(\frac{\varepsilon^2}{Re_j}) \ .$$

We find for both antisymmetric and symmetric waves that the leading order disturbance flow is neutrally stable and that

$$(\omega-\alpha U) = 0 + \varepsilon(\overline{\omega-\alpha U}) \ .$$

Hence the leading order stability equations in the pure fluid and suspension are both purely viscous, and essentially the same,

$$\psi^{iv} - 2\alpha^2\psi'' + \alpha^4\psi = -\varepsilon iR\left[(\overline{\omega-\alpha U})(\psi''-\alpha^2\psi) + \alpha\overline{U_{\bar{y}\bar{y}}}\psi\right] + O(\frac{\varepsilon^2}{Re_j}) , \quad (3.38)$$

and

$$\phi^{iv} - 2\alpha^2\phi'' + \alpha^4\phi = -\varepsilon i\nu_o R\left[(\overline{\omega-\alpha U^s})(\phi''-\alpha^2\phi) + \varepsilon\alpha U^s_{\tilde{y}\tilde{y}}\phi\right] + O(\frac{\varepsilon^2}{Re_j}) , \quad (3.39)$$

with the boundary conditions for antisymmetric disturbances

$$\psi'(-1) = \psi'''(-1) = 0 , \quad (3.40a)$$

or for symmetric disturbances

$$\psi(-1) = \psi''(-1) = 0 , \quad (3.40b)$$

together with the conditions at infinity

$$\phi, \phi' \to 0 \qquad \text{as } \hat{y} \to \infty , \quad (3.40c)$$

and the interfacial conditions at $\bar{y} = 0$

$$\psi' = \phi' + (1-\mu_o)\frac{\alpha}{\overline{\omega-\alpha}}U^s_{\tilde{y}} , \quad (3.40d)$$

$$\psi''' = \mu_o\phi''' + 3\alpha^2(1-\mu_o) - \varepsilon iR\left[(\overline{\omega-\alpha})(\psi'-\rho_o\phi') + (\mu_o-\rho_o)\alpha U^s_{\tilde{y}}\right] , \quad (3.40e)$$

$$\psi'' = \mu_o\phi'' - \frac{\alpha}{\omega-\alpha}(\overline{U_{\bar{y}\bar{y}}} - \varepsilon\mu_o U^S_{\bar{y}\bar{y}}) + \alpha^2(1-\mu_o) \ . \qquad (3.40f)$$

The solution of this problem requires a considerable amount of algebra (cf. Appendix A), and hence, we shall only summarize the important results.

Antisymmetric Disturbances

The solution of these equations and boundary conditions using the centerline conditions for antisymmetric disturbances (3.40a), gives an eigenvalue of the form

$$\alpha = \omega[1 + \alpha_1 + \alpha_2 + \ldots] \ , \qquad (3.41a)$$

where the first correction to the eigenvalue is real

$$\alpha_1 = \varepsilon \frac{b^3}{2\omega e^{2\omega}} \ . \qquad (3.41b)$$

Hence to determine whether disturbances will grow, the eigenvalue at the next order must be determined, and this is given by

$$\alpha_2 = \alpha_{2r} + i\alpha_{2_I} \ , \qquad (3.41c)$$

where

$$\alpha_{2r} = \varepsilon^2 \frac{U S_{\tilde{y}\tilde{y}}|_o}{2\omega e^{2\omega}} , \tag{3.41d}$$

and

$$\alpha_{2_I} = -\varepsilon^2 \frac{b^6 Re_j}{8\omega^4} \left[1 - \frac{9}{16\omega}(1 - e^{-4\omega}) + \frac{5}{4}e^{-4\omega} \right.$$
$$\left. - \frac{\omega}{2}(e^{-2\omega} - 2e^{-4\omega}) + \frac{2}{3}\omega^3 e^{-2\omega} + \frac{\omega + 2\omega^2}{2}e^{-4\omega} \right] . \tag{3.41e}$$

Since the imaginary part of α_2 is always negative, all antisymmetric disturbances with wavelengths on the order of the pure fluid thickness grow. However, the amplification factor decreases to zero as the wavelength decreases (cf. Appendix A).

Symmetric Disturbances

For symmetric disturbances, the first correction to the eigenvalue is real

$$\alpha_1 = -\varepsilon \frac{b^3}{2\omega e^{2\omega}} , \tag{3.42a}$$

and the second correction is complex, with the real and imaginary components

$$\alpha_{2r} = -\varepsilon^2 \frac{U S_{\tilde{y}\tilde{y}}|_o}{2\omega e^{2\omega}} , \tag{3.42b}$$

and

$$\alpha_{2_I} = -\varepsilon^2 \frac{b^6 Re_j}{8\omega^4}\left[1 - \frac{9}{16\omega}(1 - e^{-4\omega}) + \frac{5}{4}e^{-4\omega}\right.$$

$$\left. + \frac{\omega}{2}(e^{-2\omega} + 2e^{-4\omega}) - \frac{2}{3}\omega^3 e^{-2\omega} + \frac{\omega + 2\omega^2}{2}e^{-4\omega}\right]. \qquad (3.42c)$$

As is the case for the antisymmetric disturbances, the imaginary component of the wavenumber is negative for all frequencies, and decreases to zero for shorter wavelengths. However, the amplification factor for the symmetric disturbances is always larger than that for the antisymmetric disturbances, and hence for the short wavelength disturbances, the symmetric disturbances are slightly less stable. Although we have already found in the last section, that the disturbances with the largest growth rates occur for the range of wavelengths where $\ell_x \sim \ell_y \sim \nu_o^{1/2}(\varepsilon/Re_j)^{3/2}$, the short wavelength results are useful for checking the asymptotic behavior of the long wave solution as the wavelength shrinks to zero, or equivalently, as $\omega \to \infty$.

3.4 Numerical Solution

The major difficulty in solving for the roots of the eigenvalue conditions in (3.35) and (3.37) arises in calculating the integral I_1, and is primarily due to the lack of a closed form representation of the Airy function. The Airy function is an analytic, complex-valued function of a complex variable and is represented by the infinite series

$$Ai(z) = c_1 f(z) - c_2 g(z) , \qquad (3.42)$$

where

$$c_1 = .355028 \ldots ,$$

$$c_2 = .258819 \ldots ,$$

$$f(z) = \sum_{k=0}^{\infty} 1_k \frac{z^{3k}}{(3k)!} ,$$

$$g(z) = \sum_{k=0}^{\infty} 2_k \frac{z^{3k+1}}{(3k+1)!} ,$$

and

$$n_k \equiv \begin{cases} 1 & k=0 \\ n(n+3)(n+6) \ldots (n+3k-1) & k=1,2,\ldots . \end{cases}$$

Thus, in evaluating the integral

$$I_1 = \int_0^{\infty} Ai(z_0+m\hat{y})e^{-\omega\hat{y}} \, d\hat{y} ,$$

the complex value of the Airy function in the integrand must be calculated for each increment in $\hat{y}$. To avoid this expensive procedure, we rewrite the integral in terms of the new variables

$$t = m\hat{y} , \qquad s = \frac{\omega}{m} = s_o e^{i\pi/6} , \tag{3.43a}$$

and

$$s_o = \frac{1}{b}(\mu_o \omega^2)^{1/3} , \tag{3.43b}$$

to give

$$I_1 (\omega,m,z_o) = \frac{1}{m}\int_0^\infty Ai(z_o+t)\, e^{-st}\, dt = \frac{1}{m} f(s;z_o) . \tag{3.43c}$$

Taking $\partial f/\partial s$ and using the Airy equation to substitute for $tAi(t)$ gives

$$z_o f - \frac{\partial f}{\partial s} = \int_0^\infty (z_o+t)\, Ai(z_o+t)\, e^{-st}\, dt$$

$$= - Ai'(z_o) - sAi(z_o) + s^2 f(s;z_o) .$$

The solution of this differential equation for f is easily found to be

$$f(s;z_o) = e^{(sz_o - \frac{s^3}{3})}\left[f(0;z_o) + Ai'(z_o)\int_0^s e^{(\frac{r^3}{3} - rz_o)}\, dr \right.$$

$$\left. + Ai(z_o)\int_0^s r\, e^{(\frac{r^3}{3} - rz_o)}\, dr \right] .$$

Then from (3.43c)

$$f(0;z_o) = \int_0^\infty Ai(z_o+t)\,dt = \int_{z_o}^\infty Ai(\gamma)\,d\gamma = \frac{1}{3} - \int_0^{z_o} Ai(\gamma)\,d\gamma ,$$

where we have used the identity

$$\int_0^\infty Ai(\gamma)\,d\gamma = \frac{1}{3} .$$

Hence the function $f(s;z_o)$ now contains the Airy function, its derivative, and its integral, as functions of the parameter z_o only, and these can be calculated from their respective power series. However, the parameter z_o depends on the eigenvalue, (cf. 3.27) so that solving the eigenvalue conditions (3.35) and (3.37) requires an iteration scheme.

By defining the reduced wavenumber

$$\beta = -\frac{\omega\tilde{\alpha}_1}{U_y^s|_o} = \frac{\mu_o}{b^3}\,\omega\tilde{\alpha}_1 , \qquad (3.44)$$

the eigenvalue conditions can be written as functions of this reduced wavenumber and the reduced frequency s_o only, i.e., the antisymmetric condition (3.35) becomes

$$F_1(s_o,\beta) = (\beta-1)Ai'(z_o) - s_o^2 f(s;z_o)e^{i\pi/3} = 0 , \qquad (3.45a)$$

and the symmetric condition (3.37) becomes

$$F_2(s_o,\beta) = \beta Ai(z_o) + s_o f(s;z_o)e^{i\pi/6} = 0 , \qquad (3.45b)$$

where

$$f(s;z_o) = e^{i\frac{2}{3}s_o^3-\beta}\left[\frac{1}{3} - \int_0^{z_o} Ai(\gamma)\,d\gamma + Ai(z_o)\int_0^s r\, e^{(\frac{r^3}{3}-rz_o)}\,dr\right.$$

$$\left. + Ai'(z_o)\int_0^s e^{(\frac{r^3}{3}-rz_o)}\,dr\right] , \qquad (3.46a)$$

and

$$z_o = (is_o^2 - \frac{\beta}{s_o})e^{-i\pi/6} . \qquad (3.46b)$$

Note from (3.46) that $f(s;z_o)$, (and consequently F_1 and F_2), oscillates in the complex plane where the frequency of oscillation increases proportionally to s_o^3. This presents convergence problems for the iteration scheme, particularly at large values of the dimensionless frequency where f oscillates rapidly.

The eigenvalue problems for antisymmetric and symmetric disturbances are now reduced to finding β as a function of s_o for the constraints $F_i(s_o,\beta) = 0$ where i=1 is the antisymmetric condition, and i=2 is the symmetric condition. The solution procedure for a given value of s_o, takes an initial guess for β and evaluates z_o (cf. 3.46b). The power series for the Airy function, its derivative and

integral are then calculated until the absolute error of the last term, and the corresponding relative error compared to the sum are less than the tolerance of 10^{-6}. The complex-valued exponential integrals in $f(s;z_o)$, (cf. 3.46) are calculated numerically using Adam's predictor-corrector method in the differential equation-solving subroutine DGEAR. In evaluating these integrals, the error relative to the maximum value of the integrand at each step is required to be less than 10^{-6}.

The eigenvalue constraint function F_i is then evaluated, and a Newton-Raphson iteration procedure is used to make successive guesses for β. When the constraint function has converged to zero within the tolerance 10^{-6}, s_o is incremented slightly, and the iteration steps are repeated. For small values of s_o this iteration process is quite efficient, usually requiring about four iterations before converging. However at larger values of the reduced frequency, the function fluctuates rapidly, which requires the initial guess for β to be close to the final value in order for the solution to converge to the correct root. The results from this numerical scheme give the wavenumber-frequency relationship over the entire range of frequencies.

Although the eigenvalue conditions for both antisymmetric and symmetric disturbances can only be solved numerically at moderate values of the frequency, the asymptotic behaviors of both eigenvalues can be analytically determined in the limit of large frequency values. The asymptotic behavior is useful in obtaining general features of the stability curve, in addition to checking whether the numerical scheme converges to the correct root. This behavior

should also match that obtained from the short wavelength analysis.

The expansion and solution of the eigenvalue condition for large frequencies is algebraically very tedious and is summarized in Appendix C. For the antisymmetric case, the large frequency asymptotic behavior of the eigenvalue which satisfies the constraint in (3.35) is given by

$$\beta = \frac{1}{2} - i\frac{1}{16s_o^3} . \qquad 3.47a)$$

For symmetric disturbances, the solution of (3.37) in the limit of large frequencies is given by

$$\beta = -\frac{1}{2} - i\frac{3}{16s_o^3} . \qquad 3.47b)$$

Hence both antisymmetric and symmetric disturbances grow, but the symmetric disturbances are less stable. In addition, the most unstable waves for both types of disturbances occur at smaller frequency values where numerical solutions of the eigenvalue conditions are required.

In order to asymptotically match the eigenvalues from the long and short wavelength analyses, the short wavelength eigenvalue is rewritten in terms of the long wavelength variables, (i.e., setting $\omega_s = (\varepsilon Re_j/\nu_o)^{1/2}\omega$, and $\alpha_s = (\varepsilon Re_j/\nu_o)^{1/2}\alpha$ where ω_s and α_s respectively refer to the frequency and wavenumber of disturbances with wavelengths $\ell_x \sim \delta$) and evaluated as $\omega \to 0$. In terms of the

variables β and s_o the small frequency asymptotic behavior for the short wavelength antisymmetric eigenvalue in (3.41) is given by

$$\beta = \frac{1}{2} - i\frac{1}{16s_o^3} .$$

The small frequency asymptotic behavior for the symmetric eigenvalue from the short wavelength in (3.42) is given by

$$\beta = -\frac{1}{2} - i\frac{3}{16s_o^3} .$$

Hence the long and short wavelength analyses are consistent as the eigenvalues for both antisymmetric and symmetric disturbances match asymptotically (cf. 3.47).

3.5 Results

The numerical solution of each eigenvalue condition in (3.45), for disturbances with wavelengths on the order of the sublayer thickness, yields a stability curve which applies for all concentrations and axial distances. The stability curves for symmetric and antisymmetric disturbances are shown in Figures 11a and 11b respectively, where the amplification factor $(-\beta_I)$ is plotted versus the reduced frequency s_o, and $(-\beta_I) > 0$ corresponds to an unstable wave. The asymptotic behavior from the short wavelength (cf. 3.48) is also shown in each figure by a dashed line.

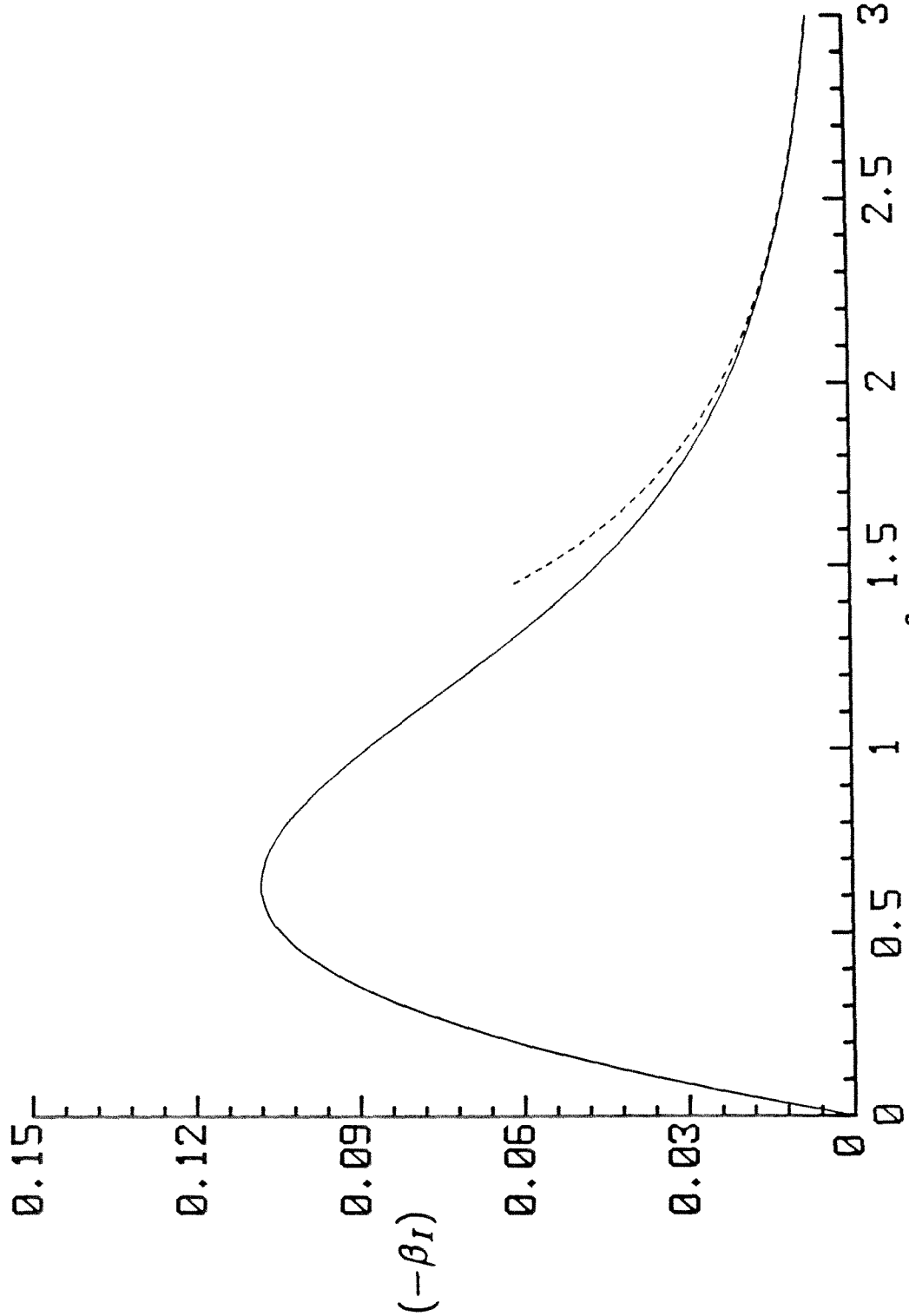

Figure 11a Numerically calculated values of $(-\beta_I)$ versus s_o for symmetric disturbances

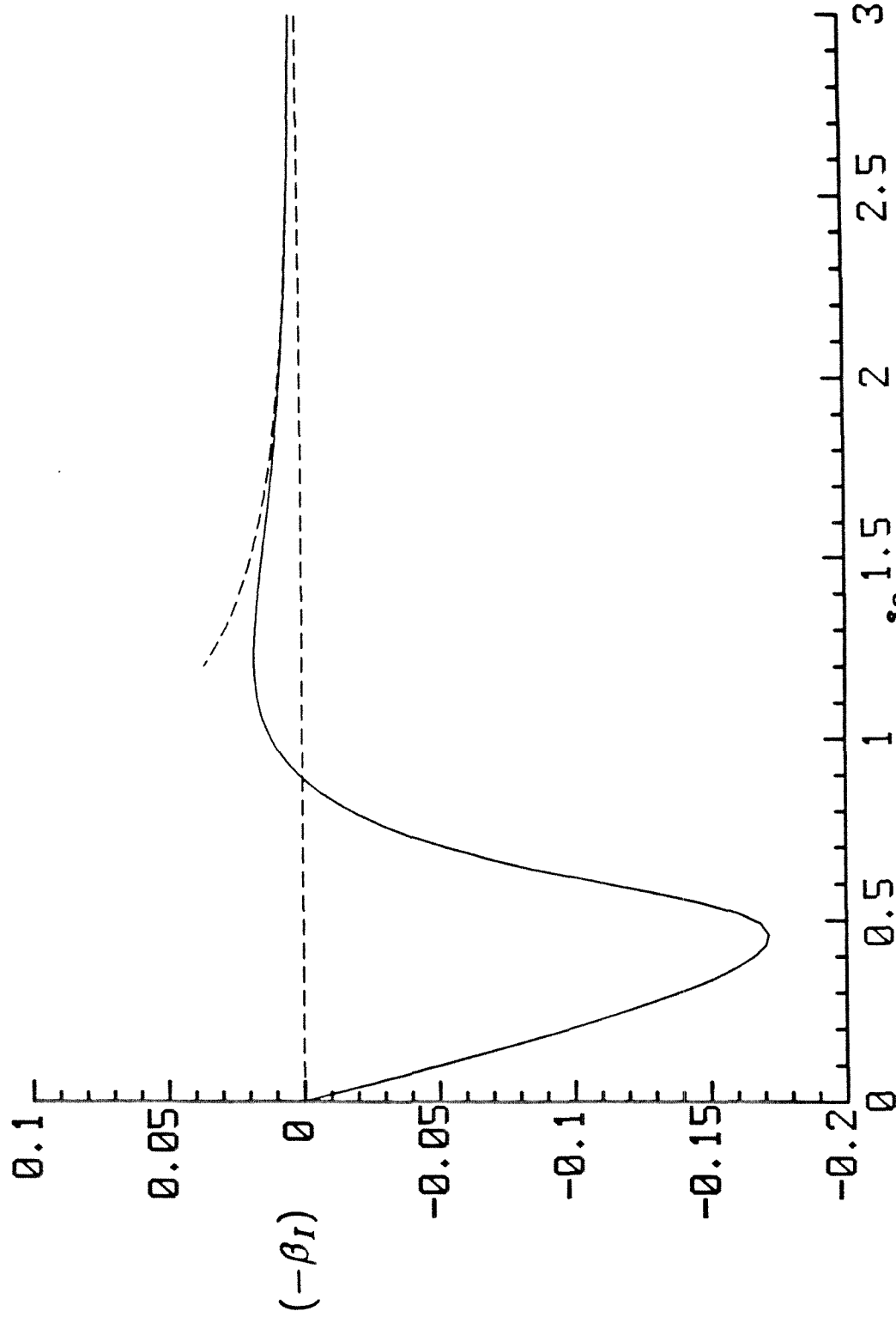

Figure 11b Numerically calculated values of $(-\beta_I)$ versus s_o for antisymmetric disturbances

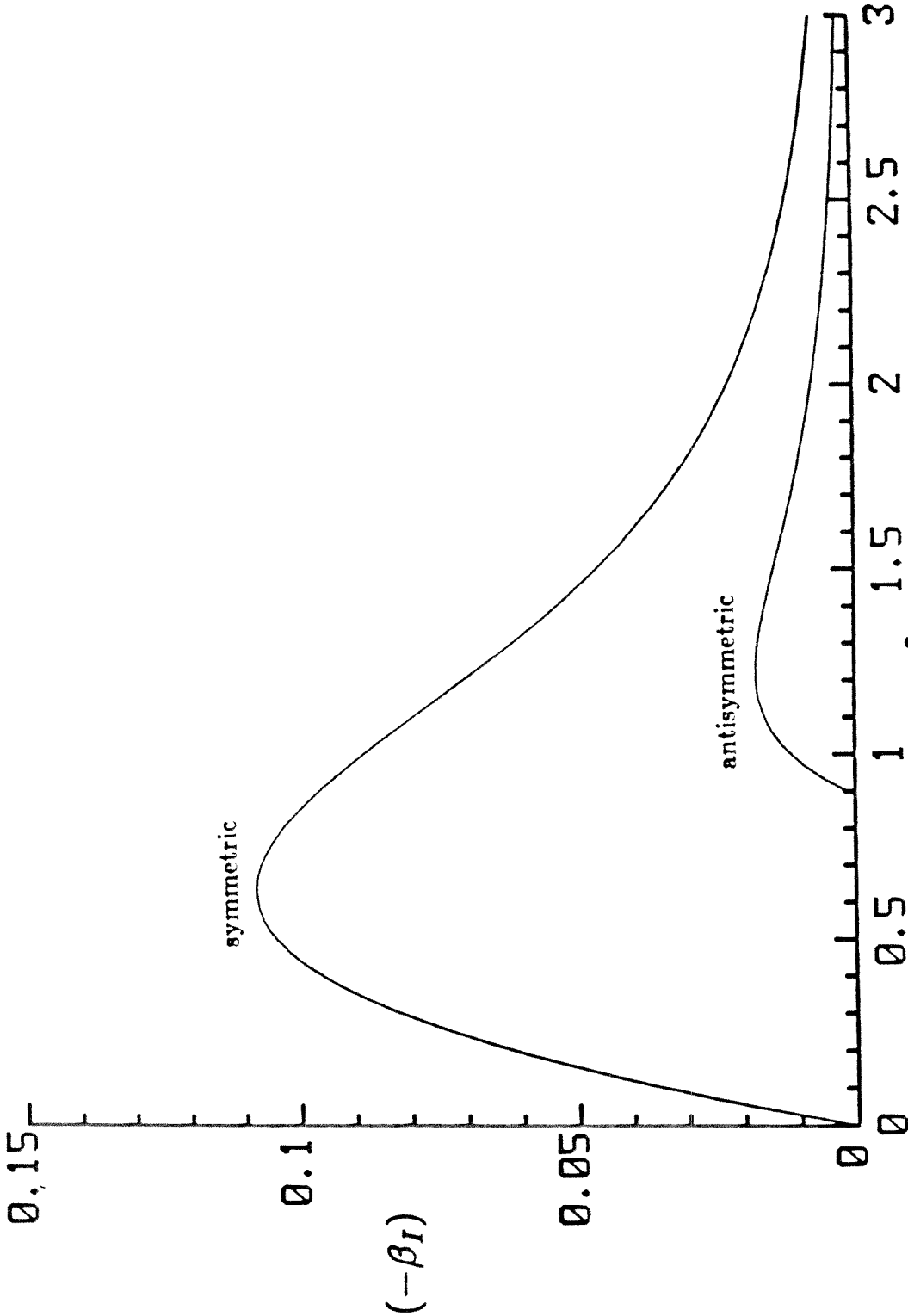

Figure 11c Comparison of the numerically calculated values of $(-\beta_I)$ versus s_o for symmetric and antisymmetric disturbances

In Figure 11a, the amplification factor is positive for all frequencies, and hence all symmetric disturbances, with wavelengths on the order of the sublayer thickness, are unstable. The least stable disturbance has an amplification factor of 0.108, corresponding to a reduced frequency value of $s_o = 0.64$. For disturbances with larger reduced frequency values, the amplification factor drops quickly, and approaches the asymptotic behavior predicted by the short wavelength analysis.

In contrast with the results for the symmetric disturbance, the antisymmetric disturbances are stable at small frequencies. Figure 11b shows that the damping factor, i.e., β_I, initially increases with the reduced frequency, and reaches a maximum value of 0.171 at a reduced frequency of $s_o = 0.46$. Disturbances where $s_o < 0.89$ are also stable, but the damping factor decreases to zero. Above this value of the reduced frequency, all disturbances are unstable. The amplification factor for the unstable disturbances increases to a maximum value of 0.0175 for waves with a reduced frequency of $s_o = 1.20$. At still larger values of the reduced frequency, the amplification rate follows the behavior predicted by the short wavelength analysis, and decreases to zero.

The amplification factors for both symmetric and antisymmetric disturbances are plotted versus the reduced frequency, s_o, in Figure 11c. Thus, the symmetric disturbance is always less stable than the antisymmetric disturbance, and in determing the conditions under which disturbance growth will be first observed, it is sufficient to consider the symmetric disturbances only.

The real component of the wavenumber β_r, which is plotted versus s_o in Figures 12a and 12b for the symmetric and antisymmetric disturbances respectively, represents the deviation of the wave speed from the interfacial velocity, i.e.,

$$c_w = 1 + (\nu_o \frac{\varepsilon}{Re_j})^{1/2} \frac{\beta_r}{\omega} U^s_{\bar{y}}|_o \ .$$

The dotted lines in these figures show the asymptotic behavior predicted by the short wavelength analysis. Thus for symmetric waves, the deviation is in the negative direction, and results in a slower wave velocity compared to the base flow interfacial velocity. However, for antisymmetric waves, the wave velocity is larger than that of the base flow interfacial velocity.

Since the stability curve in Figure 11a is independent of Gr_j and Re_j, there is no critical value for these parameters, i.e., all flows are unstable. However, it is still possible that stable flows may be observed experimentally since the amplification rate may be small enough that disturbances are convected some distance, or even out of the apparatus, before they can grow to an observable size. Since the initial amplitude of these small disturbances is unknown, it is very difficult to make quantitative comparisons of the amplification rates with the experiments. However qualitative comparisons of the effect of the jet Reynolds and Grashof numbers, and the concentration on the amplification rate still can be assessed.

In order to make such comparisons, the amplification rate must be determined. From (3.8a), the perturbed interface position is given

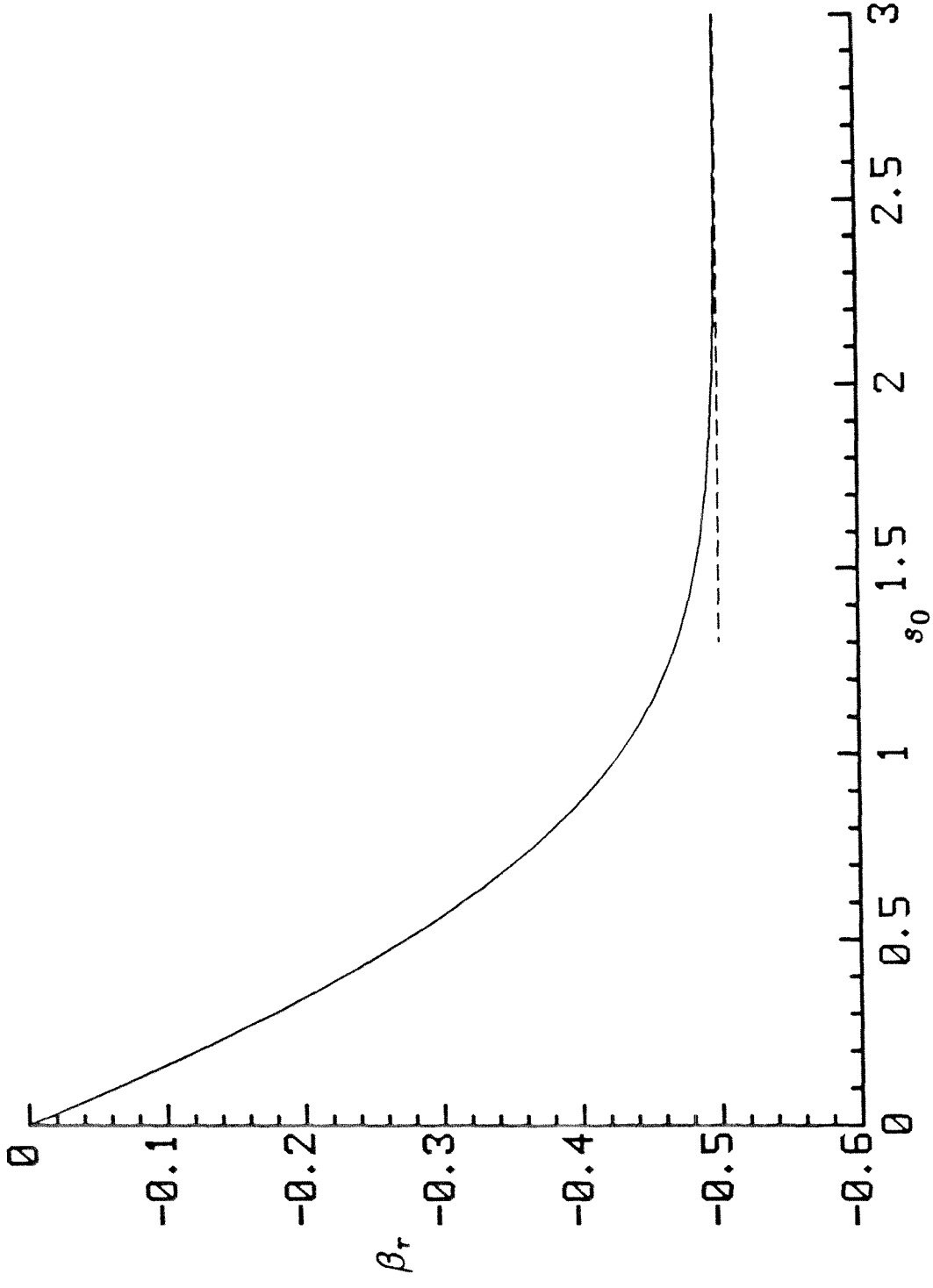

Figure 12a Numerically calculated values of β_r versus s_o for symmetric disturbances

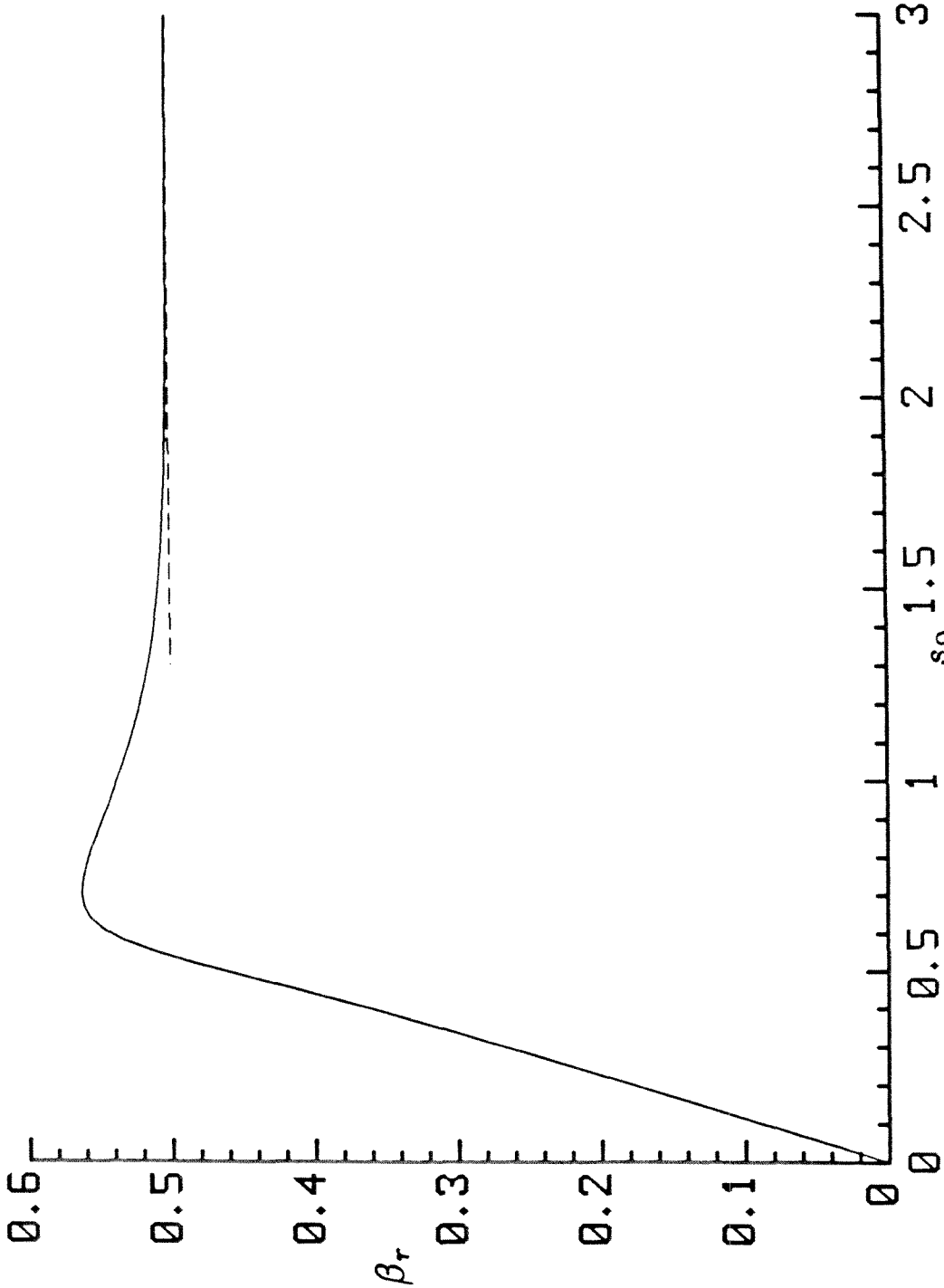

Figure 12b Numerically calculated values of β_r versus s_o for antisymmetric disturbances

by

$$\bar{\Gamma} = \frac{\eta}{b} \exp[i\{g(\hat{x}) - \hat{\omega}\hat{\tau}\}] \tag{3.48}$$

where $\frac{dg}{d\hat{x}} = \hat{\alpha}(x) = \frac{\alpha}{b(x)}$, i.e.,

$$g(\hat{x}) = \frac{1}{\ell_x} \int_{x_o}^{x} \frac{\alpha(\xi)}{b(\xi)} \, d\xi \ . \tag{3.49}$$

The magnitude of $\bar{\Gamma}$ is determined from the imaginary component of the eigenvalue

$$\alpha_I(x) = (\nu_o \frac{\varepsilon}{Re_j})^{1/2} \, b^3(x) \, \beta_I(s_o) \ ,$$

which, upon substituting for $\ell_x \sim \nu_o^{1/2}(\frac{\varepsilon}{Re_j})^{3/2}$ in (3.49) gives

$$|\bar{\Gamma}| = |\frac{\eta}{b}| \exp \left[- (\frac{Re_j}{\varepsilon}) \int_{x_o}^{x} \beta_I(s_o) \, b^2(\xi) \, d\xi \right]$$

In general, this integral can not be evaluated analytically since the reduced wavenumber β_I is an implicit function of x. However, since the argument of the wavenumber is a weak function of x, i.e.,

$$s_o(\hat{\omega},x) \sim s_o(\hat{\omega})b^{1/3} = s_o(\hat{\omega})x^{-1/15} \sim s_o(\hat{\omega}) \ ,$$

the wavenumber is approximately constant. Hence the magnitude of the interface perturbation becomes

$$|\bar{\Gamma}| \sim \exp\left[-\ 1.089\ \left(\frac{Re_j}{\varepsilon}\right)\ \beta_I\ x^{3/5}\right]$$

where x_o has been taken as the origin. Since the plume solution occurs in the asymptotic limit of

$$\left(\frac{Re_j}{\varepsilon}\right) \sim \left(\frac{Gr_j Re_j^3}{b_o^3}\right)^{1/5} >> 1$$

(cf. 2.10 and 2.17), the disturbance is expected to grow to an appreciable size over a relatively small length. Taking the maximum amplification factor for symmetric disturbances, i.e., $|\beta_I| = 0.108$, and substituting for Re_j/ε, gives the magnitude of the perturbed interface for the maximum amplified wave,

$$|\bar{\Gamma}_m| \sim \exp\left[.1176\ \left(\frac{Gr_j Re_j^3}{b_o^3}\right)^{1/5}\ x^{3/5}\right]. \qquad (3.50)$$

Thus the dimensionless inception distance H_i/b_o^*, where the amplitude of the perturbed interface for the maximum amplified disturbance grows to a size A, is given by

$$\frac{H_i}{b_o^*} = (8.5034\ \ell nA)^{5/3}\ Gr_j^{-1/3} Re_j^{-1}\ . \qquad (3.51)$$

Hence, the effect of increasing the jet Grashof number is destabilizing, which is due to the increasing importance of buoyancy in the flow. An increase in the jet Reynolds number is also destabilizing, as this increases the rate at which buoyancy is introduced into the flow.

The reduced wavenumber and frequency of the maximum amplified disturbance are both constants. Hence, an increase in the concentration of the suspension, which increases the Grashof number, is destabilizing. However, the frequency and wavenumber for the maximum amplified disturbance, given by

$$\hat{\omega} \sim \mu_o^{-1/2}(s_m)^{3/2} \quad \text{and} \quad \hat{\alpha} \sim \mu_o^{-1/2}\beta_m \ ,$$

where s_m and β_m refer to the reduced frequency and wavenumber for the maximum amplified disturbance, will decrease to smaller values. Furthermore, a disturbance of a given frequency will exhibit different amplification factors if it encounters variations in the particle concentration, (for example, in a suspension with stably stratified levels of particle concentration), where these amplification factors will depend on the particle concentration, as well as the frequency of the disturbance.

3.6 Discussion

In order for a disturbance to grow, it must receive energy from the base flow. For the base flow described in the Case I solution, the mechanism for energy transfer is mathematically expressed in the tangential stress condition at the interface, by the balance of the

difference in the shear stress derivative of the base flow, with the disturbance streamfunctions. However the shear stress of the base flow, and its derivative, are both of order ε and do not appear in the leading order equations. Hence at this order, no energy is supplied to the disturbance flow, and disturbances of all wavelengths are neutrally stable and travel with a speed equal to the base flow interfacial velocity.

At a higher order, energy is supplied to the disturbance flow in the pure fluid and suspension regions, and the stability of the flow depends on the relative rate at which energy is transferred, to that at which it is dissipated by viscosity. The flow region in the pure fluid is very thin, and the disturbance flow is purely viscous there. In comparison, the width of the flow region in the suspension is much larger, and hence viscous dissipation rates there much smaller, than those in the pure fluid. Thus, the disturbances which are the least stable occur in the flows where the suspension region cannot fully dissipate the energy that is supplied by gravity. Of course, the amount of energy that is supplied is a function of the wavelength, and the type, (i.e., antisymmetric or symmetric), of the disturbance.

For disturbance waves that are antisymmetric with respect to the centerline, the base flow derivative in the shear stress condition, i.e., $\overline{U_{\bar{y}\bar{y}}}|_o$, is balanced by the $\psi''(0)$ term and energy is transferred to the disturbance flow in the pure flow. However when the wavelength of the disturbance is very long, the disturbance streamfunction in the pure fluid copies the base flow, (i.e., $\Psi = U$), which hinders the rate at which energy is transferred to the disturbance flow. The amount of energy dissipated by viscosity

balances that which is fed into the pure fluid region and the flow remains stable. As the wavelength is decreased, the energy is still transferred to the disturbances in the pure fluid. However, the streamfunction no longer copies the base flow and the energy that is supplied is larger than the amount that is dissipated by viscosity. Thus the disturbance grows, and the flow becomes unstable. For very short wavelengths, disturbances in both the pure fluid and suspension regions are excited. However the disturbance flow in both regions are purely viscous, so that the disturbances are unstable, but their growth rates are small.

For symmetric disturbances the leading order shear stress condition balances the $\overline{U_{\bar{y}\bar{y}}}$ and $\phi''(0)$ terms and hence, energy is transferred to the disturbance flow in the suspension. The larger length scale in the suspenion results in less viscous dissipation than in the pure fluid. Thus for an unstable antisymmetric disturbance, the corresponding symmetric disturbance at the same frequency will be less stable.

Although the velocity profiles are similar, the stability characteristics of the two-phase and pure fluid plume base flows are quite different. The two-phase plume solution (which applies at large jet Grashof numbers and hence is expected to be less stable) has no critical Grashof or Reynolds numbers. In addition, this analysis does not show the existence of an upper branch to the neutral stability curve, whereas for pure fluid plume flows, short waves are stable. However, the amplification factor of the unstable waves quickly drops to zero, as it is proportional to the inverse cube of the reduced frequency. Hence it is likely that higher order

terms in the wavenumber will cause the amplification factor to cross the $\beta_I = 0$ axis, thereby giving stable, short wavelength disturbances. Finally, previous stability analyses for pure fluid plumes predict that symmetric disturbances are always more stable than antisymmetric disturbances, whereas for the two-phase plume, we have shown that the opposite is true.

CHAPTER 4

Experimental Observations

4.1 Introduction

In Chapter 2, asymptotic solutions were developed which describe the flow of a jet in a suspension. The asymptotic limits are specified in terms of the jet Grashof and Reynolds numbers, and a dimensionless distance from the nozzle. For given values of the jet Grashof and Reynolds numbers, the theory predicts a sequence of flow solutions as the jet travels downstream. There are essentially two different flow sequences. For $Gr_jRe_j \ll 1$ (cf. Figure 2), after a short entry region the flow evolves into a fully-developed jet and then, as the distance from the nozzle increases, buoyancy becomes increasingly important until the flow becomes a pure plume. For larger values of Gr_jRe_j, the fully developed plume-like solution evolves directly from the entry region flow (cf. Figure 3).

In Chapter 3, the stability of the fully developed plume-like velocity profile was analyzed using classical linear theory in order to examine the flow conditions under which disturbances should be observed. This analysis predicts that the fully developed flow is unstable at all values of the jet Grashof and Reynolds numbers. However, as noted in analyses by Atherton & Homsy (1973) and Herbolzheimer (1983), in some situations the growth rate is small enough that an unstable disturbance is convected an appreciable distance before it grows to an observable size. Hence, the magnitude of the amplification factor, as well as its sign, is important in determining the conditions under which instabilities are observed. With this interpretation, the stability analysis predicts a distance

at which disturbances can be expected to be observed in terms of the jet Grashof and Reynolds numbers.

The experimental data described in this chapter was collected in order to make quantitative comparisons with the theoretical predictions. This required a flow apparatus that produced a two-dimensional jet flow in a uniformly distributed suspension. A natural choice for this apparatus is a fluidized bed. For a two-dimensional flow field, the interface (i.e., the boundary separating the pure fluid and suspension regions) has the same shape throughout the depth of the flow column, and hence, projects as a single curve in the plane of flow. This is true even if the flow is perturbed provided that the disturbances are two-dimensional. Thus, we obtained the spreading rate of the pure fluid region and the inception distance where a disturbance is first observed from still photographs of the flow region using a microfiche reader to provide an enlarged picture of the film negative. This method allowed quantitative data to be taken without disturbing the flow field.

Before these quantitative experiments were performed, however, initial flow visualization experiments were conducted to verify that the flow in the fluidized bed was two-dimensional and that the initial suspension concentration was uniform. These were followed by additional experiments in which qualitative features of the jet flow were examined.

In the next section, we shall describe the apparatus design, the flow loop, and the flow materials used in the experiments. Next, we present observations made during the flow characterization experiments. Finally, the quantitative experiments are described,

and the values of the spreading rate and inception distance measured experimentally are compared to those predicted by the theory.

4.2 Apparatus and Flow Materials

The experimental apparatus consists of the flow column, its support structure, and the devices required to produce the necessary flow (see Figure 13). The flow column is a rectangular chamber made of lucite, which can be easily dismantled into two sections. The region of flow is in the upper chamber, where changes in the column width, flow distributor, and jet nozzle can be easily made. As a consequence of this design, however, there are many joints which must be sealed to prevent leaks.

4.2a Apparatus

The upper chamber has front and back walls made of 48 x 25.25 x 0.5 in. lucite plates and two sets of side walls made of 48 x 15.24 x 0.75 in. lucite plates (see Figure 14a). The side walls are connected by threaded steel rods, and adjusting the length of these rods allows the width of the flow region to be set at 10, 30, 45, or 60 cm. Both sets of inner and outer side walls have 0.115 in. deep rectangular grooves cut along their sides. In each groove is a single cylindrical strip of 1/8 in. diameter neoprene rubber, which provides a seal in the same fashion as an O-ring. The front and back walls of the column are clamped along the entire length of the outer side walls with aluminum angled bars, which are pulled tight with a series of 4 inch long bolts spaced vertically 6 inches apart. Although these clamps were sufficient in sealing any external leaks

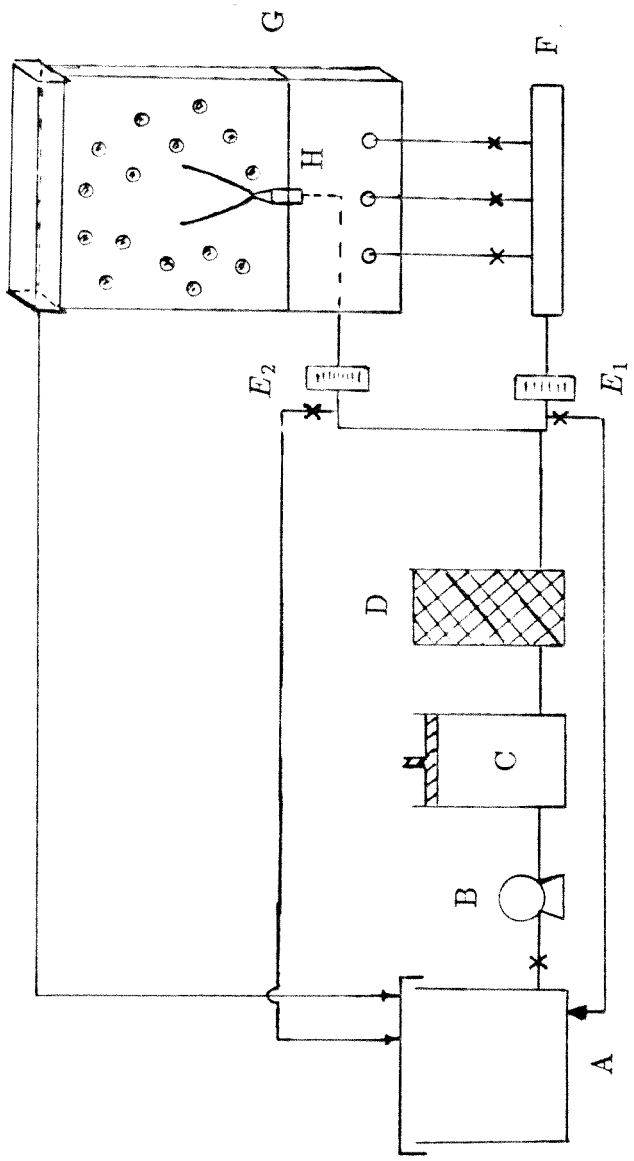

Figure 13 The experimental set up

A) holding tank, B) pump, C) surge tank, D) filter, E_1) jet rotameter, E_2) distributor rotameter, F) manifold, G) flow column, H) nozzle.

Figure 14a The upper column

through the outer side walls, there was a leak around the inner side walls due to hydrostatic pressure causing the front and back plates to bend. This was undesirable not only because of the leak, but also because the curvature of the plates (approximately 1/4 in. maximum displacement) could affect the two-dimensionality of the flow field. Hence, it was necessary to brace these plates using steel channel supports placed at the position of the inner side walls. These supports pushed the front and back plates against the neoprene strips of the inner side walls, simultaneously eliminating the bending and leaking problems.

The lower chamber is a rectangular box made of lucite plates with the inner dimensions 30 x 60 x 6 cm (see Figure 14b). Since it was not necessary to dismantle this section, the four walls and the bottom were glued together. The liquid enters the chamber through three 1/2 in. diameter ports spaced evenly along the bottom of the front plate, and is used to fluidize the particles in the upper chamber. The height of the chamber is chosen large enough to dampen any turbulence due to entrance effects at the ports.

The fluid from the lower chamber passes through the distributor and fluidizes the particles in the upper chamber. The main function of the distributor is to provide a flow with a flat velocity profile so that the particles are uniformly fluidized. Medlin, Wong, and Jackson (1974) performed a linear analysis to determine the effects of distrubutor width and pressure drop on the stability of uniform fluidization in beds of finite height. They found that wide distributors with small pressure drops (relative to the total pressure drop across the bed) caused growth of small disturbances in

Figure 14b The lower column

a uniformly fluidized state. Agarwal, Hudson, and Jackson (1980) later verified experimentally that circulatory flow patterns (where particles rise over one portion of the distributor and fall over another portion) arose for wide distributors with small pressure drops across them, and that these non-uniformities could be eliminated by reducing the distributor width or by increasing the resistance to flow. Specifically, they verified earlier predictions that very thin distributors with a pressure drop of at least 1/10 that of the total pressure drop across the bed would provide a stable, uniformly fluidizing flow.

Following a design similar to that used by Agarwal et al., our distributor consisted of a wire mesh screen supported on a 1/32 in. thick stainless steel plate (see Figure 14b). The support plate for each distributor is 26 in. x 4 3/8 in. and has a rectangular hole 1.9 x 6 cm in the center (for the jet nozzle housing) which is framed by two 1/4 in. wide metal strips. Outside of these strips are two rectangular holes of identical width, which provide the region for flow. Hence, the width of these holes is the only variable in the different distributors (i.e., for the different column widths). The flow resistance across the holes is provided by a 10 micron wire mesh screen cloth (Cambridge Wire Cloth Co., Cambridge, MD). A separate screen cloth covers each of the rectangular holes, and is soldered to the metal plate frame.

The joint between the upper and lower chambers, which holds the distributor, is a potential source of leaks. To prevent these leaks, gaskets made of 1/32 in. thick neoprene were cut and placed both above and below the distributor plate. Thus, the gaskets seal the

joint when the flanges of the upper and lower chambers are clamped together using steel channels with 1/8 in. set screws spaced evenly apart.

The feed for the nozzle enters a rectangular box which is constructed from sheet metal and has a cross section of dimensions 1.9 x 6 cm and a length of 16.5 cm. It is sealed to the center hole of the distributor support using RTV silicone glue (an industrial sealant) thereby providing a leak proof but removable seal. This allows one to use the same nozzle box for the different distributors. Flow enters the nozzle box through a 1/2 in. diameter threaded hole in the base of the nozzle housing. The threaded, brass tube which passes through the front plate of the lower column into this hole, has O-ring seals to prevent the system from leaking. The interior of the nozzle box houses a matrix of cylindrical tubes, which serves as a flow straightening device to remove any disturbances caused by the entry port. The jet issues out of a nozzle which is made from a lucite block of the dimensions 4.1 x 2.06 x 6 cm. The inner dimensions (see Figure 14c) were chosen so that the jet exits the nozzle vertically with a flat velocity profile. The slit of the nozzle (of width 0.1 cm) was chosen to be small with respect to the column width so that the jet flow would be unaffected by the side walls. However we shall see that even for these small slit widths, the effect of the side walls was sometimes very significant. The nozzle, which is sealed into the top of the box with RTV, can be easily removed and replaced.

The column is housed inside a support frame constructed from steel Unistruts. It sits on a base which is adjusted with three

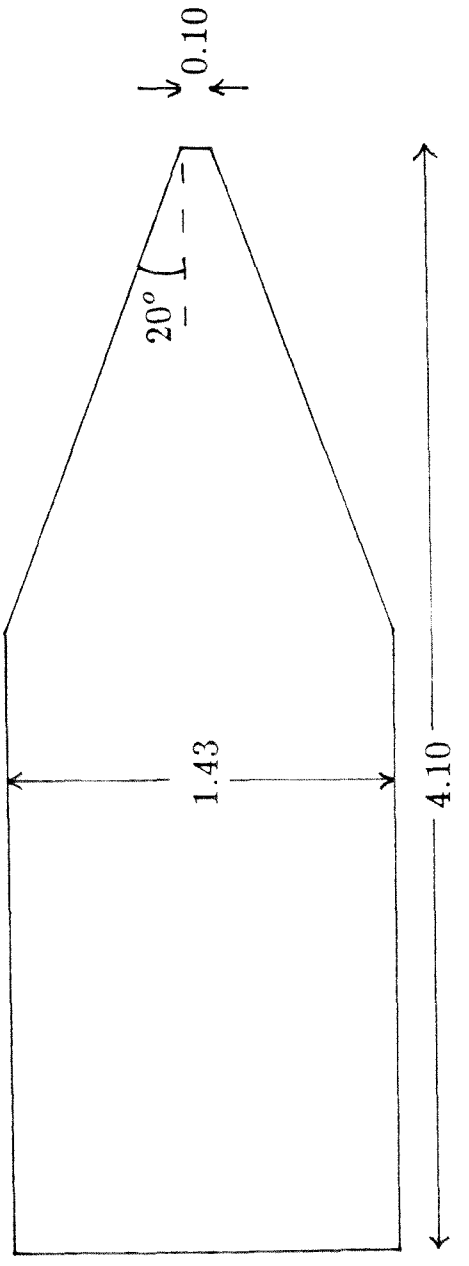

Figure 14c The jet nozzle (units in cm)

leveling screws to keep the system vertical. Variable speed hand drills are used to raise or lower the upper chamber from the lower chamber, and a sliding overhead trolley facilitates moving the upper chamber away, where any necessary modifications may be made. Three cross bar supports are spaced approximately 12 inches apart on the front and back of the superstructure. Threaded steel rods brace the steel channel supports mentioned earlier (i.e., those which prevent the lucite walls from bending) against these cross bar supports.

Assembling the column so that it would not leak was essentially a trial and error process. However, once a satisfactory procedure was established, the column could be repeatedly reassembled without leaks. In this procedure, the inner side walls are placed at the appropriate distance from the outer side walls to give the desired column width, and the threaded steel rods are tightened to hold these positions rigidly. The vaseline lubricated neoprene strips are then laid into the side wall grooves and the entire side wall structure is placed on the front lucite plate. Flanges located at the top and bottom of the outer side walls butt up against the side of the lucite plate thereby fixing the position of the inner side walls, and hence, the width of the flow region. A vernier caliper is used to insure that the inner column width (i.e., flow region width) is constant along the entire length of the column. The back plate is then laid on top of the side walls and the clamps made of the aluminum angled bars are evenly tightened on both sides. The ends of the neoprene strips are cut off flush with the base of the side walls (both inner and outer sets) and sealed into the groove with a small amount of RTV. A small bead of RTV (approximately 1/8 in.

wide) is then placed on the bottom of each side wall and when the upper and lower columns are joined, these beads spread and seal against the top distributor gasket.

The upper column is bolted to the overhead trolley and is then aligned above the lower chamber. The jet nozzle box has already been sealed to the distributor plate using RTV, and the distributor lies on the lower column between the neoprene gaskets. The gaskets are lubricated so that the neoprene material is not kinked or torn by any shifting of the upper chamber. The upper column is then gradually lowered onto the lower chamber with the variable speed hand drills. When the column comes to rest on the distributor gasket, the flanges of the upper and lower column are clamped by the steel channels, and the set screws are gradually tightened. It is important that these screws are evenly tightened on both sides so that there is an even pressure on the gasket.

The flow originates from a 26 gal. capacity reservoir tank which was covered to prevent contamination of the fluid (see Figure 13). A submersible pump (Little Giant catalogue no. 504902) sends the fluid to a surge tank where any pulses in the flow are dampened. The flow then enters an in-line filter with a 5 micron filter cartridge. The filter is necessary to prevent contaminant particles from clogging the screen in the distributor, and disturbing the uniform fluidization. The flow exiting the filter is then split into two streams. One flow stream is sent to the lower chamber of the column, and the other stream is sent to the jet nozzle. Both streams are monitored with needle valve rotameters manufactured by Cole Parmer, Chicago, IL) so that their flow rates may be varied

independently.

The flow stream that is sent to the lower chamber first enters a distributing manifold. This manifold splits the incoming stream into three exiting streams. Valves located on these exiting streams allow one to adjust their flow rates until they are all approximately equal. These streams then feed the three entry ports of the lower chamber. An additional 1/2 in. ID tube exiting the manifold tube passes through a gate valve back to the reservoir tank and serves the dual purpose of draining the fluid from the column, as well as recirculating the flow back to the reservoir tank. This last function allows one to remove any air bubbles from the flow loop, and hence, ensures a two phase flow system. Additional shunt lines located before each rotameter and the jet nozzle box, serve this same purpose.

The fluid then enters the lower chamber, passes up through the distributor, and fluidizes the particles in the upper chamber. The separate flow source entering the nozzle box issues through the nozzle slit forming the pure fluid jet. The fluid from the jet and the distributor exits the upper chamber through an overflow box, and is then recycled into the reservoir tank through 3/4 in. ID tubing.

4.2b Flow Materials

The liquid phase was a mixture of water and a water soluble synthetic oil (UCON oils 50-HB-2000 and 75-H-90,000 manufactured by Union Carbide Long Beach, CA). The UCON oils have larger densities and viscosities than water, so that a wide range of fluid properties, in this case, viscosity, can be obtained. The viscosity and density

of the mixtures were measured (with a Cannon-Fenske viscometer and a Kessler hydrometer, respectively) both before and after each set of experiments and were found to be constant. The particles were spherical glass beads (homogenized glass beads from VWR Norwalk, CA) which were approximately uniform in size with a mean diameter of 105 μm (manufacturer specificies that the particle diameters are within 100 - 110 μm) and a density of 2.55 gm/cm^3.

4.3 Flow Characterization Experiments

Initial experiments were conducted to verify that the distributor fluidized the particles uniformly. A nonuniform distributor is undesirable since it can cause particles to accumulate in different regions. A buoyancy force would then be exerted on the regions of lower particle concentration, which would produce a large scale circulatory motion in the bed (Agarwal et al. (1980)). The inhomogenities, which also took the form of a local spouting flow near the distributor, were best detected by visual observation of the particles in the bed. Any distributor which produced a spouting flow, or circulatory motion in the bed was not used. Figures 15a-15c (see Plate 1) are pictures of the bed taken during the fluidization process with a uniformly fluidizing distributor. Although the interface is somewhat blurred due to the small distribution in the particles' sizes, it is still seen to be quite flat.

The qualitative behavior of the flow from the jet nozzle was observed using dye particles (instead of the glass particles) in the outer fluid. The flow field was observed to be two-dimensional with an inner pure fluid region and an outer dyed fluid region. At lower

jet velocities, the interface between the pure and dyed fluid regions was smooth, i.e., no disturbances were observed. However, as the velocity of the jet was increased, disturbances in the form of two-dimensional waves appeared at the interface and grew with increasing distance from the nozzle. At even larger jet velocities, the flow became turbulent and the dyed fluid was mixed into the pure fluid region. Figures 16a-16f (see Plate 2) show a sequence of flows of the liquid jet in dye where the jet Reynolds number is gradually increased. Note that although disturbances in the flow field are visible in Figures 16b and 16c, the interface is still well defined. However for the turbulent jet, the outer dye becomes mixed into the pure fluid region, and the interface is indistinguishable. In Figures 16d-16f, the onset of turbulence is seen to move closer to the nozzle as the jet Reynolds number is increased.

In general, a reasonably straight jet issued from the nozzle. Further downstream, the jet leaned to one side, although the flow remained two-dimensional. This bend became more pronounced with time until the jet contacted the wall, where it continued to flow up the column. Figures 17a-17c (see Plate 3) show a sequence in time where the jet gradually leans toward a wall. The time has been made dimensionless using the column width divided by the jet velocity at the nozzle. The final position is shown in Figure 17c. For columns of smaller width, the jet contacted the wall at shorter distances. In some flows with larger column widths, the jet traveled vertically over the entire region where the dye could be seen, which suggests that the bending of the jet is caused by interactions with the side walls.

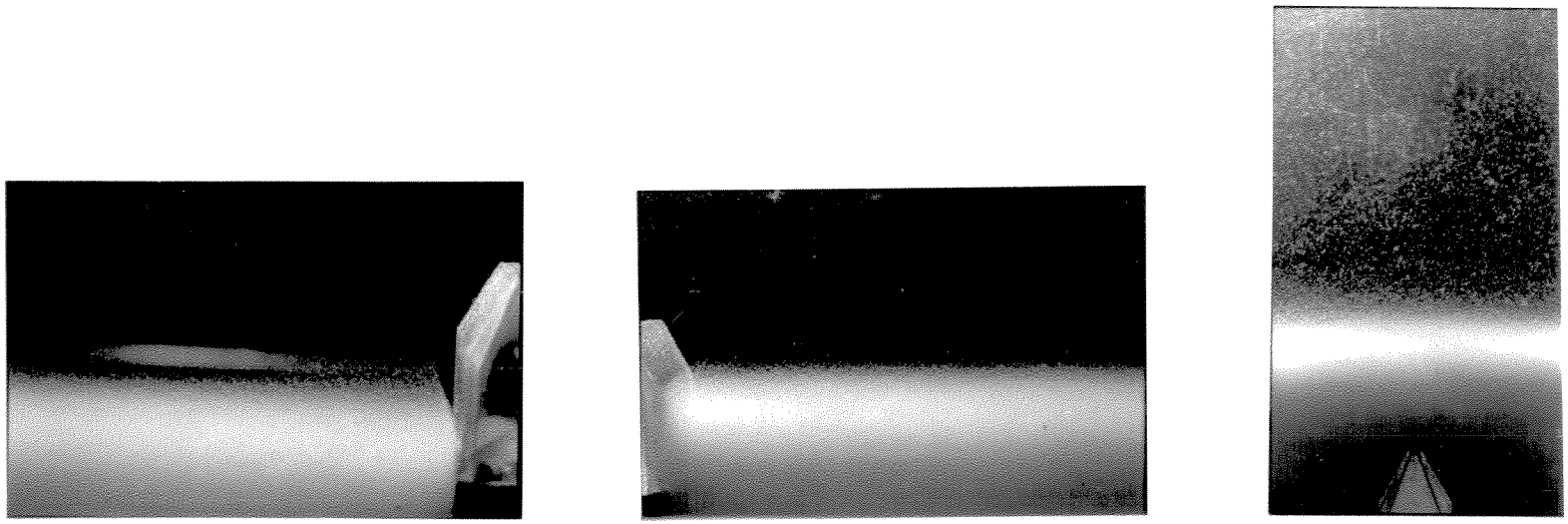

(a) (b) (c)

Figure 15 The fluidization process: a) at one end of the flow chamber; b) at other end of the flow chamber; c) above the nozzle

PLATE 1

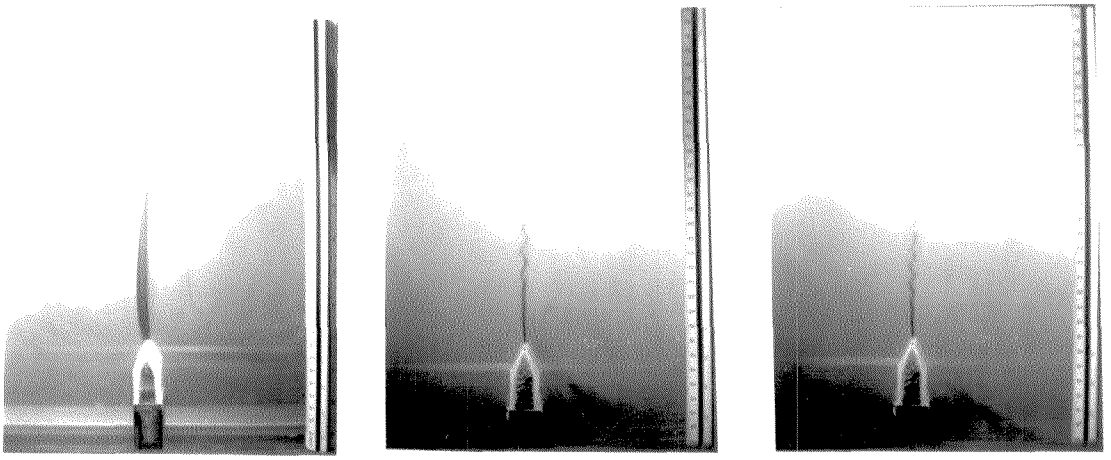

$Re_j = 3.5$ (a)

$Re_j = 37.5$ (b)

$Re_j = 50.3$ (c)

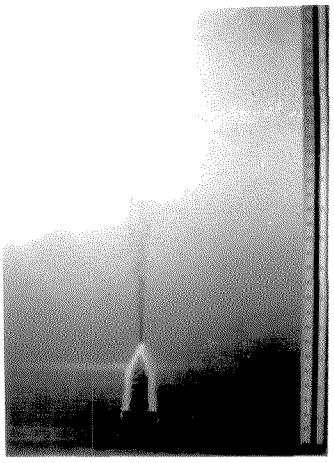

$Re_j = 84.8$ (d)

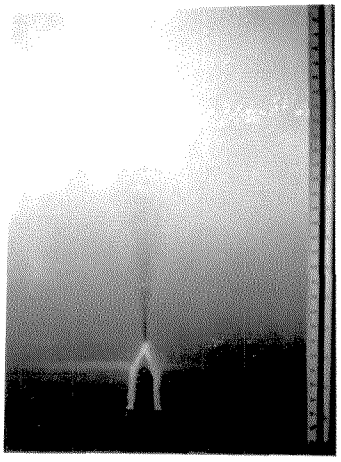

$Re_j = 118.5$ (e)

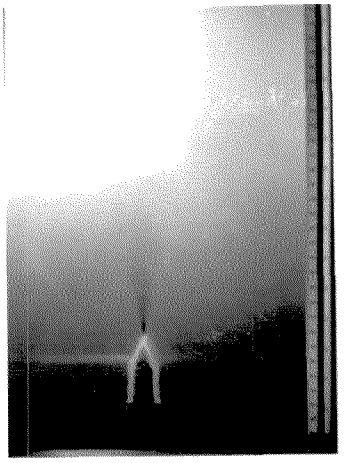

$Re_j = 253.5$ (f)

Figure 16 Transition of a pure fluid jet to turbulent flow.

PLATE 2

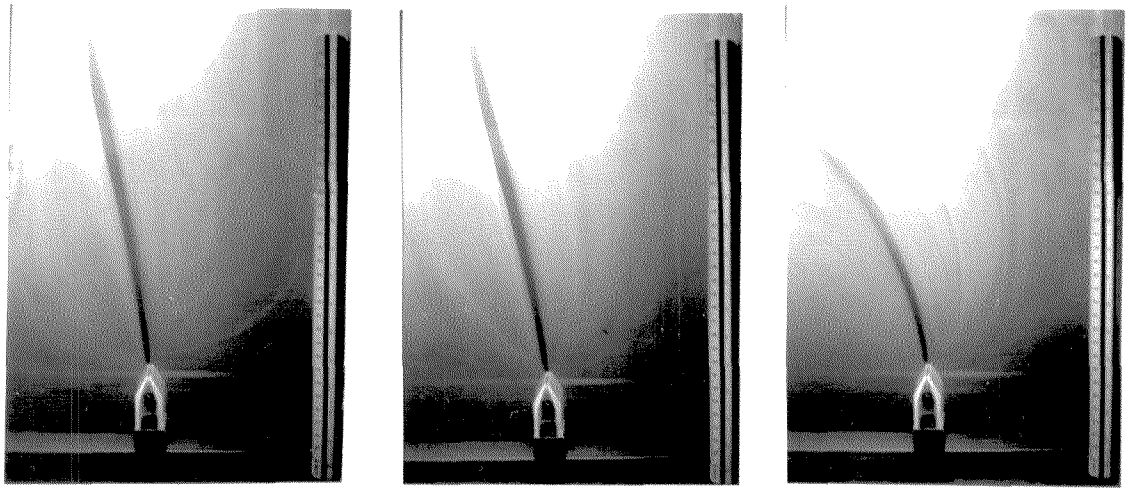

Figure 17 Attachment of a pure fluid jet to the column wall for dimensionless time $t = \frac{t^* u_j}{H}$ where H is the column width.

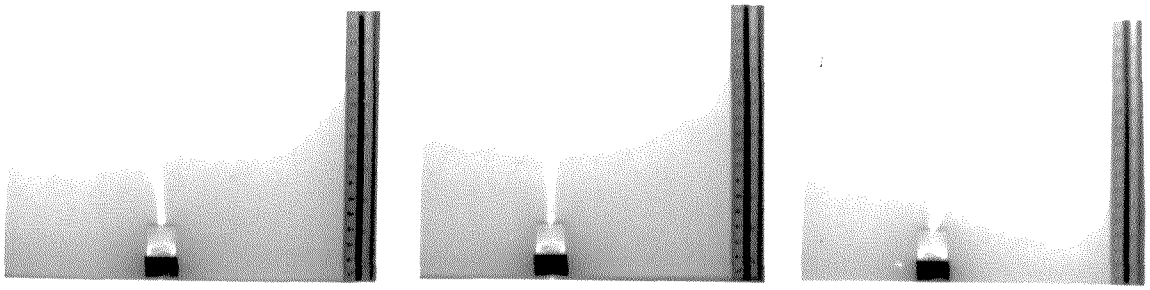

Figure 18 Flow visualization of the oscillating jet in a suspension of glass particles: $Gr_j = 0.02, Re_j = 3.2$.

PLATE 3

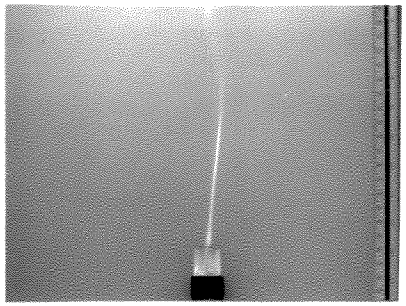

$Gr_j = 0.026 \quad Re_j = 3.3$

(a)

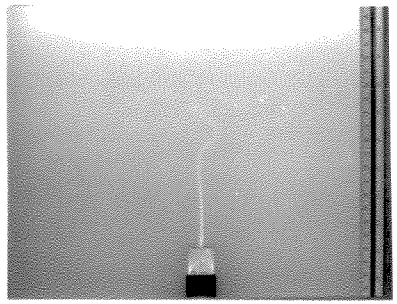

$Gr_j = 0.088 \quad Re_j = 1.8$

(b)

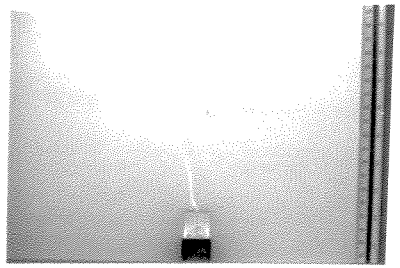

$Gr_j = 0.78 \quad Re_j = 0.60$

(c)

Figure 19 Flows for decreasing nozzle velocity.

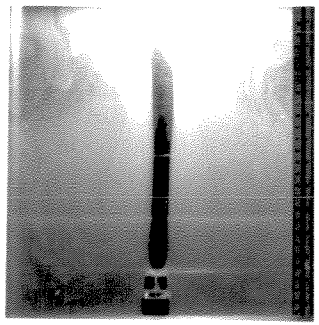

$Re_j = 3.5$

(a)

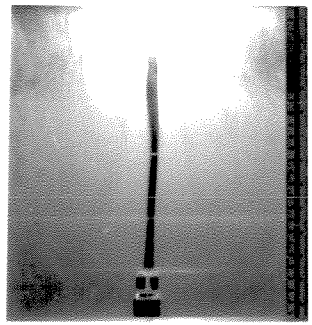

$Re_j = 0.6$

(b)

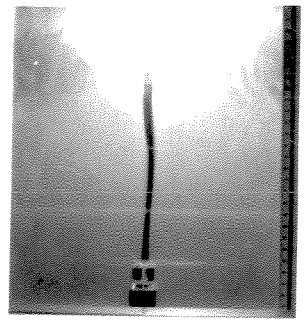

$Re_j = 0.3$

(c)

Figure 20 The flow of a jet with small bouyancy effects.

PLATE 4

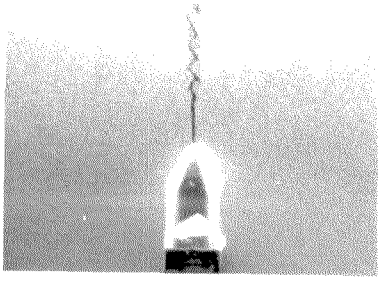

Figure 22 An unstable, high velocity jet in a dilute suspension : $Gr_j = 0.0003 \quad Re_j = 80.8$

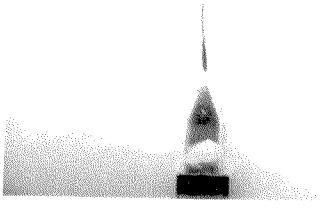

Figure 23 An unstable, bouyant jet in a suspension : $Gr_j = 0.033 \quad Re_j = 7.9$

PLATE 5

This behavior is analogous to the Coanda effect for a turbulent jet, where the jet is deflected towards a nearby wall because of a low pressure region at the surface. Several investigators have observed this phenomenon and attribute the experimentally verified low pressure region near the wall to the acceleration of the entrained fluid there. Pera and Gebhart (1975) observed a similar phenomenon in their experimental study of heated laminar plumes near either a side wall or another plume. They found that a plume was deflected towards a side wall, or another plume of roughly equal or greater buoyancy, and that the plume would attach itself to the other body if it was close enough. They attributed this deflection to the other body's hindrance of the entrainment of fluid into the plume. Their photographs of this behavior show a remarkable similarity to those of our deflected jet.

The jet behavior changed dramatically when the glass particles were added to the column. As in the case of the jet in a dyed fluid, the flow was two-dimensional and the jet leaned towards one side of the flow column. However, the denser particles in the suspension exert a vertical force which counteracts this motion. The jet straightens and then leans to the other side of the flow column, and a steady oscillating motion results, though no particles are mixed into the pure fluid region by this motion.

The frequency of the oscillatory motion increased for columns with narrower widths, but it was nearly constant for those columns with widths greater than 30 cm. Hence, the width of the column was set at 30 cm so that a minimum quantity of fluid and particles was required. A similar oscillatory behavior was observed by Forstrum

and Sparrow (1967) in their experimental study on plumes of heated air . They took particular care to isolate their system from drafts and disturbances, but the oscillations still persisted. They concluded that the oscillations were characteristic of free boundary plume flows.

The buoyancy force also caused the pure fluid region to narrow with increasing distance from the nozzle and eventually this region formed a tip. The tip oscillated at a larger frequency than the lower portion of the jet, causing the pure fluid region to bend in a time-dependent, two-dimensional sinuous shape. Although they were unable to explain it, Fujii, Morioka, and Uehara (1973) observed this same motion in their experimental study on plumes of heated spindle oil. Figures 18a-18c (see Plate 3) show a sequence of pictures taken of the liquid jet in a suspension of glass particles. The whip-like motion of the tip, which caused particles to mix into the pure fluid region, was observed even at very small particle concentratons, e.g. $c \sim 0.001$. Figures 19a-c (see Plate 4) show a sequence of experiments where the jet Grashof number was increased by decreasing the nozzle velocity. For larger jet Grashof numbers and also for smaller jet Reynolds numbers, the distance to where the tip motion occurs decreases.

The flow characterization experiments show that a buoyant jet flow field, which divides into regions of pure fluid and suspension, can be produced in our experimental apparatus. Although the buoyancy force due to the suspension induces an oscillating motion in the jet, the flow remains two-dimensional, and no particles are mixed into the pure fluid region by this motion. Further downstream,

however, disturbances cause the interface to bend in a sinuous shape, and particles are mixed into the pure fluid region. Using still photographs of the experiments, we can make quantitative comparisons of the interfacial spreading rate (measured with respect to the arc distance along the centerline) and the inception distance for instabilities of the jet (i.e., the position of the first bend in the interface) with those predicted by the theory.

4.4 Measurements of Interfacial Spreading Rate

4.4a Experimental Procedure and Flow Conditions

The particles were first fluidized to an initial height (typically 30cm), which together with the known amount of particles in the bed was used to determine the particle concentration in the suspension. In most of the experiments, once the particles were fluidized to the desired height the distributor was turned off and the particles were allowed to settle briefly. The jet flowmeter was then set to a desired flow rate, and 35mm still pictures (ASA 400 film) were taken of the interface between the pure fluid and suspension regions. The column was backlit with a 250w light source and the glass particles in the suspension reflected much of this light so that the interface boundary was sharply defined. The interfacial spreading rate and the inception distance were measured from the photograph negatives using a microfiche reader (magnification 3x). A ruler was placed next to the flow field in each experiment to account for possible distortion effects due to the microfiche reader and the camera. In those flows where the jet oscillated, the values of the interfacial spreading rate and the

inception distance (measured from a sequence of photographs taken at different times) were found to be approximately constant in time. Hence, quantitative comparisons can be made with the predictions from the steady state theory.

By varying the fluid viscosity, particle concentration, and jet velocity, a range of experimental flow conditions was obtained. This was done systematically by performing a series of experiments at a fixed fluid viscosity and particle concentration over a range of jet flow rates. For the same fluid, the particle concentration was then increased by adding more particles to the flow column and new experiments were performed for the same flow rates. In this way, the concentration was varied from $c \sim 0$ to $c \sim 0.05$. At higher concentrations, the instabilities were so strong that the jet oscillated rapidly and the interface became three dimensional (i.e., curved with respect to the depth of the column). This prevented light from passing through the pure fluid region and no quantitative measurements could be made using still photographs.

The fluid viscosity was then decreased by diluting the mixture with water, and the experiments at the various concentrations and flow rates were repeated. The approximate range of kinematic viscosities used was from 0.08 to 0.5 stokes. In all of these cases, the particle Reynolds number (defined in terms of the particle radius, and Stokes velocity), was 0.01 or lower. For the entire set of experiments, the flow conditions are summarized in terms of the parameter Gr_jRe_j, where

$$0 < Gr_jRe_j < 1.2 \ .$$

The lower range of this parameter occurred for essentially pure fluid flows, where dye particles marked the interface position. Although the dye particles were slightly more dense than the pure fluid, no value for the jet Grashof number could be calculated. No meaningful data on the spreading rate or inception distance could be obtained at values of Gr_jRe_j greater than 1.2 because instabilities caused particles to mix with the jet very near the nozzle, and the interface was not observable.

The experiments were grouped in terms of the parameter Gr_jRe_j so that the interfacial spreading rates could be compared with those predicted by the analysis in Chapter 2. For a nozzle width of 1 mm, the entry region described in Chapter 2 (cf. Figures 2 and 3) was very short. Hence, we shall ignore this region and assume that the flow exiting the nozzle is fully developed.

4.4b Spreading Rate Results $Gr_jRe_j \ll 1$

The case where Gr_jRe_j is small occurs for pure fluid flows (with dye particles) and also flows with very small particle concentrations, $c \sim 0.005$. The experimentally measured spreading rates were compared to those predicted by the pure fluid jet solution (cf. 2.60) in Case III. A measure of the fit is given by s, the square root of the variance, where

$$s^2 = \frac{1}{n-1} \sum_{x_i}^{n} [b_e(x_i) - b_t(x_i)]^2 ,$$

n is the number of experimental data points, and $b_e(x_i)$ and $b_t(x_i)$ are respectively, the experimentally measured and theoretically predicted interface positions at the axial distance x_i. The variance is normalized with respect to the quantity (n-1) (as opposed to the quantity n) since the data points are only a sample of the total possible experimental measurements (cf. Kreyszig (1979)). The axial distances were adjusted by a virtual origin which was chosen to give the best fit. However for most cases, the change in the variance for the different virtual origins was small. Some of these comparisons are shown in Table 3, and in general the theoretical predictions show an excellent agreement with the experimental measurements particularly for the flows at large jet Reynolds numbers. However, for those flows of a jet in a dilute suspension, the jet does not travel far downstream before the flow becomes unstable.

For the flows of a pure fluid jet in dye at small jet Reynolds numbers, the fit of the theoretical and experimental spreading rates is much worse. At small distances from the nozzle the theory predicts a slower spreading rate than is experimentally observed, and at larger distances, it predicts a faster spreading rate than is observed.

The pure fluid jet solution assumes that the transverse velocity component is negligible at leading order, which is not true at small jet Reynolds numbers. Hence, the transverse velocity of the experimental jet causes it to spread faster than the theory predicts. However, the presence of the dye in the outer fluid causes a small, but finite buoyancy force to act on the jet as it flows downstream. This accelerating force decreases the spreading rate, and in some

Table 3

Comparison of Experimental, $b_e(x)$, and Theoretical, $b_t(x)$, Spreading Rates for Case III at Different Values of Gr_j and Re_j

Gr_j	Re_j	x	$b_e(x)$	$b_t(x)$	s x 10^4
0.0002	46.7	0.286	0.064	0.062	0.34
		0.467	0.071	0.066	
		1.000	0.079	0.077	
		2.070	0.087	0.092	
		2.762	0.095	0.099	
		4.222	0.103	0.112	
		5.127	0.111	0.119	
0.0003	29.1	0.143	0.064	0.062	0.43
		0.248	0.071	0.068	
		0.698	0.079	0.079	
		0.968	0.087	0.086	
		1.543	0.095	0.097	
		2.476	0.103	0.110	
		3.756	0.111	0.125	
0.0	84.8	0.258	0.064	0.063	0.16
		1.152	0.073	0.073	
		2.032	0.081	0.081	

Table 3 (continued)

Gr_j	Re_j	x	$b_e(x)$	$b_t(x)$	s x 10^4
0.0	37.9	0.413	0.071	0.067	1.20
		0.716	0.079	0.075	
		0.984	0.087	0.080	
		2.324	0.095	0.100	
		2.851	0.103	0.106	
		4.222	0.111	0.119	
		5.756	0.119	0.131	
		8.740	0.127	0.149	
0.0	13.9	0.325	0.089	0.113	4.3
		0.871	0.107	0.126	
		1.221	0.125	0.133	
		1.718	0.143	0.141	
		2.136	0.161	0.148	
		2.996	0.179	0.160	
		4.357	0.196	0.175	
		5.618	0.214	0.188	
		7.461	0.232	0.203	
0.0	1.1	0.471	0.252	0.219	14.0
		0.707	0.269	0.226	
		2.394	0.286	0.266	
		5.626	0.303	0.320	
		8.896	0.320	0.361	
		10.495	0.337	0.378	

cases causes the jet to stop spreading (see Figures 20a-20c, Plate 4). Of course, since the theoretical solution ignores buoyancy effects, it predicts a spreading rate at large distances from the nozzle that is faster than what is observed experimentally.

The experimentally observed spreading rate behavior of the liquid jet in dye is qualitatively predicted by the theory in the flow sequence where $Gr_j Re_j \ll 1$ (cf. Figure 2), i.e., where the pure fluid exhibits mixed plume-jet characteristics as it flows downstream. In this flow sequence, the jet spreading rate decreases to zero at a dimensionless distance of order $H/b_o^* \sim (Re_j^2/Gr_j)^{1/3}$. The theoretical flow solutions which apply in this region are Cases IIa and IIb. However, no solution was obtained for the flow described by Case IIa (i.e., where the initial momentum of the jet is important). Furthermore, the buoyancy force due to the dye particles could not be calculated, and as a result, no quantitative comparisons were made with the theory. The theory predicts that a jet in a suspension of small particle concentration should also exhibit mixed plume-jet characteristics as it flows downstream. However, we experimentally observed that these flows became unstable before the mixed plume-jet state was reached.

4.4c Spreading Rate Results $Gr_j Re_j \sim 1$

For the case of larger values of the parameter, $Gr_j Re_j \sim 1$, the theory predicts that the laminar plume solution will occur immediately after the entry region flow. As in the jet case, the entry region was ignored (since it occurs over a small distance) and the flow exiting the nozzle was assumed to be fully developed. In

the plume solution, the interface position has a simple dependence on the axial distance given by

$$b \sim x^{-1/5} .$$

In order to compare the experimental measurements with this prediction, the spreading rate data is plotted in log-log form. A linear regression analysis is then used to determine the best fitting line through the transformed data, and the slope of this line gives the exponent of the power law. The amount of scatter in the data is measured by the deviation of the correlation coefficient, r, from a value of 1.0.

A few examples of the log-log plots of the data are given in Figures 21a-21d. The solid lines on the graphs represent the theoretical predictions for the spreading rate. In general, these predictions agree very well with the experimental results. In each plot, the slope is approximately equal to the predicted value of -0.20, and the correlation coefficients are near 1.0. A summary of the experimental results is given in Table 4 (see Appendix C). The slopes range from -0.18 to -0.28 and in general exhibit fairly high correlation coefficients.

4.4d Inception Distance Results

The inception distance, where disturbances are first observed, was measured experimentally at various jet Grashof and jet Reynolds numbers, and compared to the values predicted by the theory (cf. 3.51). The instabilities were of a wave-type form, and the inception

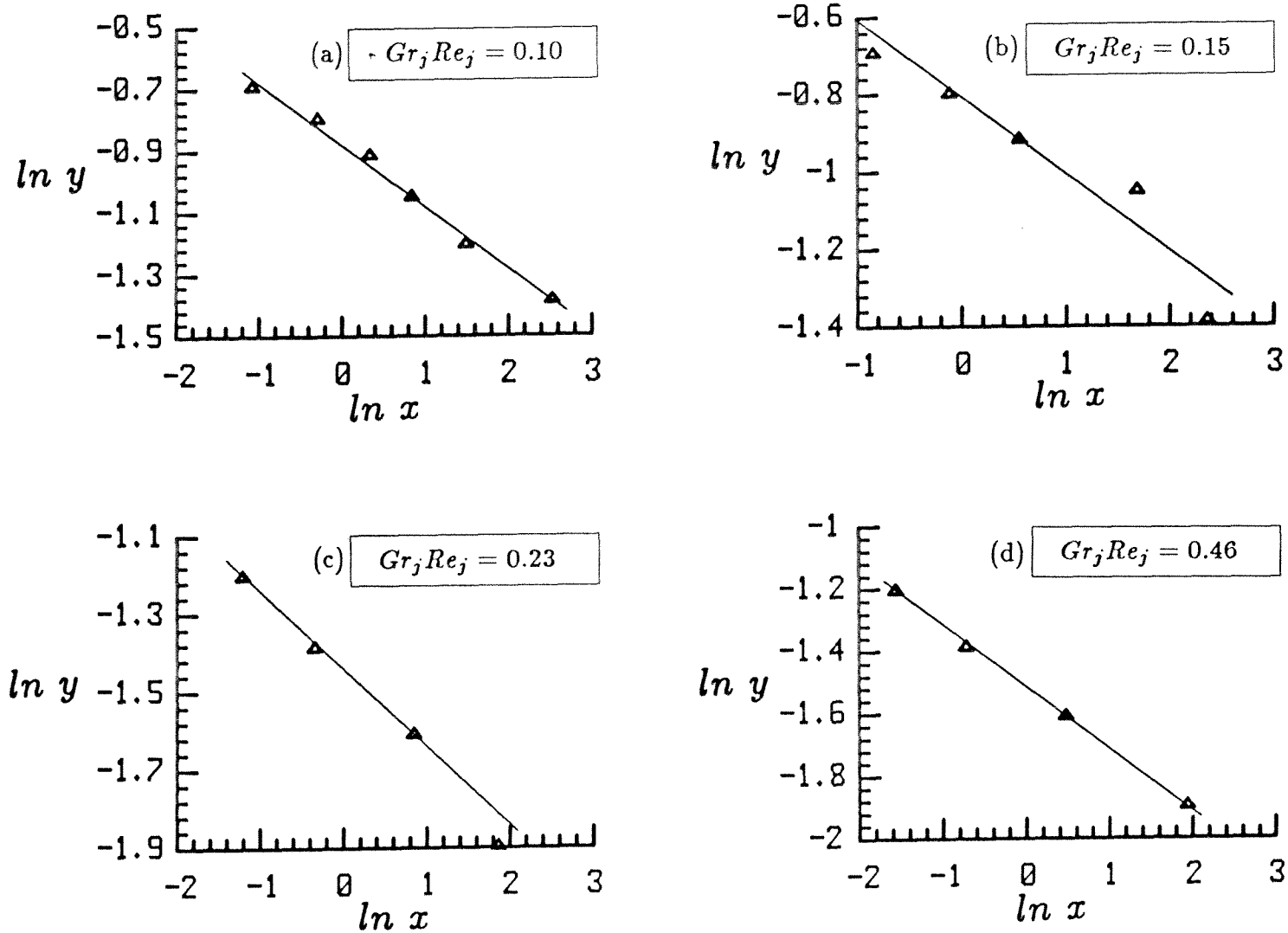

Figure 21 Experimentally measured spreading rates : *a)* $Gr_jRe_j = 0.10$ *b)* $Gr_jRe_j = 0.15$ *c)* $Gr_jRe_j = 0.23$ *d)* $Gr_jRe_j = 0.46$. The solid line is the prediction from Case I.

distance was measured from the tip of the nozzle to the position of the first bend in the interface. As the amplitude of the disturbance grew, an increasing number of particles were mixed into the pure fluid region until it could no longer be seen. In the jet-like flow, the growth of the disturbance could be seen for three or more disturbance wavelengths before the pure fluid region was obscured by particles (see Figure 22, Plate 5). In the buoyant plume-like flow, the lower portion of the jet oscillated steadily, but no particles were mixed into the pure fluid region. However, once disturbance growth occured, the pure fluid region was quickly obscured by particles, approximately 1/2 to 1 disturbance wavelengths downstream from the inception point (see Figure 23, Plate 5).

The linear stability analysis of the base flow solution in Case I predicts that for a given amplification of a disturbance (e.g. that at which a disturbance is seen) the inception distance, H_i/b_o^*, multiplied by the quantity $Gr_j^{1/3}Re_j$ is a constant (cf. 3.51). Hence, a plot of $Gr_j^{1/3}Re_j\ H_i/b_o^*$ versus the flow parameter, Gr_jRe_j, should give a horizontal line. This plot is shown in Figure 24. It appears that there is little correlation of the experimental data with the theoretical prediction. In addition to the large scatter of the data, the general trend shows that $Gr_j^{1/3}Re_j\ H_i/b_o^*$ decreases with increasing Gr_jRe_j. The comparison of the data and the theoretical predictions at small values of Gr_jRe_j may be questionable, since the theory predicts that the base flow solution applies for $Gr_jRe_j \sim 1$. However in the last section it was found that the theoretically predicted interfacial spreading rate of the plume solution agreed quite well with the experimental data, even at values of $Gr_jRe_j = 0.1$. At

larger values of $Gr_j Re_j$, where the base flow solution is expected to apply, there is still a large scatter of the data. Furthermore, using a typical experimental value for the constant

$$c = \frac{H_i}{b_o^*} Gr_j^{1/3} Re_j = 50,$$

the linear stability analysis predicts that the magnitude of the interface perturbation is only 3.4 times its original size (cf. 3.51). It appears that the disturbances grow much faster than the theory predicts, and hence there is a discrepancy.

A plausible explanation for the discrepancy between the results of the stability theory and the experiments, is that the disturbances which are observed experimentally are initially finite in size. These disturbances require a smaller amplification (compared to that for the infinitesimal disturbance assumed by the linear theory) to reach a magnitude which can disrupt the flow field. Furthermore, nonlinear interactions of finite disturbances can cause a larger growth rate than that predicted by the linear theory. Hence, a finite disturbance would destabilize the flow at a shorter distance than that predicted by the linear theory, which is what we observed experimentally.

These finite amplitude disturbances may result from vibrations of the experimental apparatus, or more probably, from the oscillations of the plume. Although the oscillating motion is steady in the lower portion of the plume, buoyancy (which forces the pure fluid to flow vertically) causes a whip-like motion at the tip of the

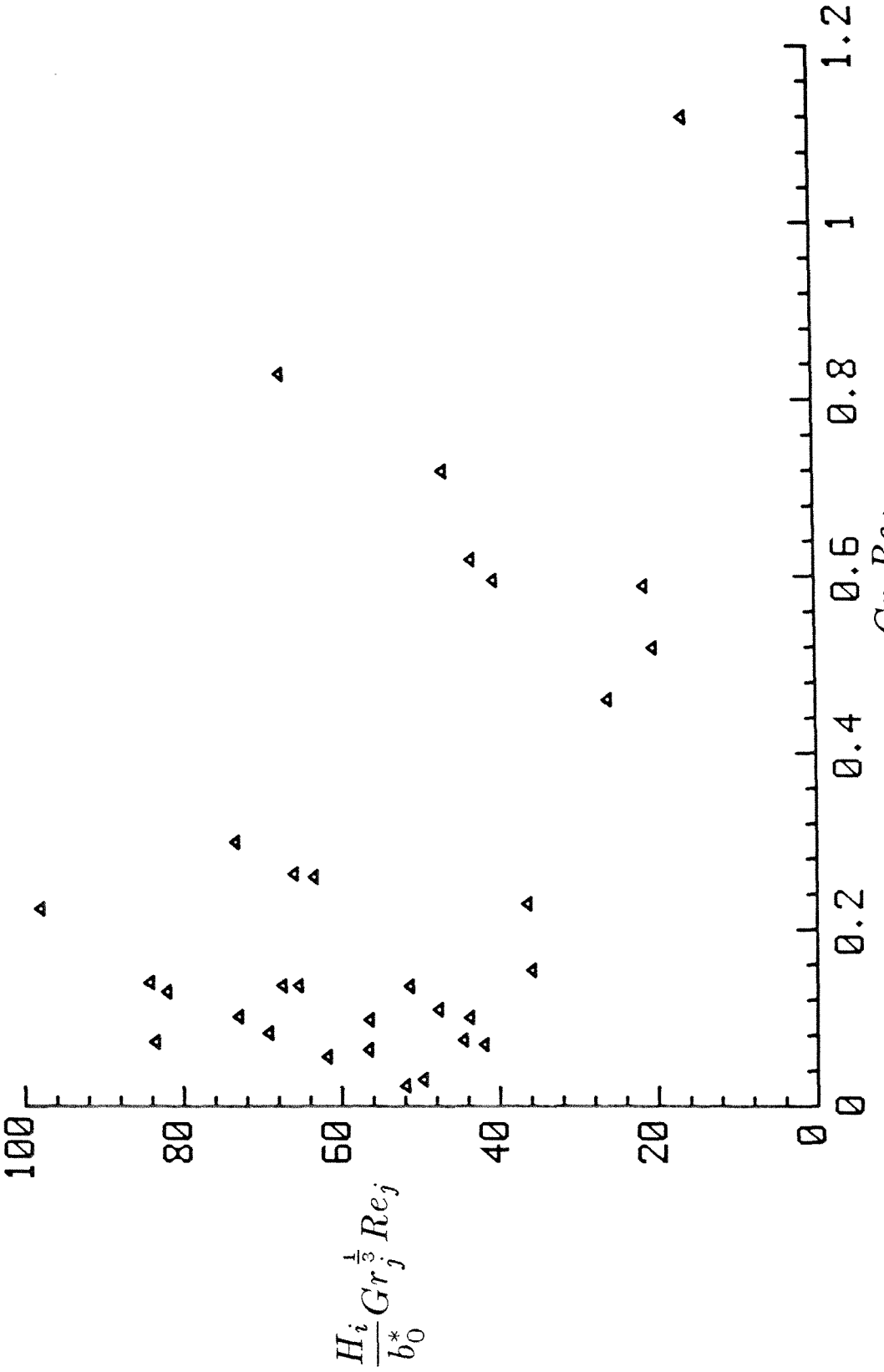

Figure 24 Experimentally measured inception distances.

pure fluid region. This finite amplitude disturbance motion is also periodic, however, the frequency of oscillation is larger than that of the lower portion of the plume. Hence, the whip-like motion of the tip causes a sharp bend in the interface (relative to the lower portion of the plume) and results in particles mixing into the pure fluid region. The size of the disturbance motion depends on the size of the buoyancy force, where the flows at larger jet Grashof numbers exhibit larger amplitudes in the oscillating motion of the tip. This qualitatively explains the downward trend observed in Figure 24, as the flows at larger values of the parameter $Gr_j Re_j$ have smaller inception distances.

In order to quantify the instability region, local Grashof and Reynolds numbers can be defined as

$$Gr_x = \frac{(\rho_p - \rho_f) c_o g x^*}{\rho_f (u^*_{pl})^2} , \quad \text{and} \quad Re_x = \frac{b^* u^*_{jet}}{\nu} ,$$

where u^*_{pl} and u^*_{jet} are the local velocities at the centerline for the plume and jet solutions, respectively. These velocities, along with the width of the jet flow region, b^*, are given by the expressions

$$u^*_{pl} = 1.2317 \, (Gr_j Re_j / b^*_o)^{1/5} \, u_j \, x^{*^{1/5}} ,$$

$$u^*_{jet} = 0.4543 \, (b^*_o Re_j)^{1/3} \, u_j \, x^{*^{-1/3}} ,$$

$$b^* = 10.880 \left(\frac{\mu_f \nu}{M_o}\right)^{1/3} x^{*2/3}.$$

Hence, the local Grashof and Reynolds numbers are defined in terms of the dimensional distance, x^*, and the experimental data can then be used to calculate the values of these parameters at which the flow becomes unstable. A plot of the local Grashof number versus the local Reynolds number at instability is shown in Figure 25. Although there is still some scatter in the experimental data, the regions of stability and instability are fairly well defined. This figure shows that increasing the Grashof number slightly from zero results in a large decrease in the local Reynolds number of transition. Hence, for the laminar flow of a two-dimensional jet, the presence of the particles in the outer fluid is highly destabilizing, as the jet becomes unstable at much shorter distances than the corresponding single phase flow.

4.5 Discussion

As predicted by the analysis developed in Chapter 2, the two-dimensional flow field of a jet in a homogeneous suspension divides into regions of pure fluid and suspension (at uniform concentration), and because of the heavier particles in the suspension, a constant buoyancy force is exerted on the pure fluid region. The experimental results indicate that this buoyancy force has a significant effect on the laminar flow of a jet.

Based on the experimentally measured interfacial spreading rates, the theory accurately predicts a variety of flow behaviors for

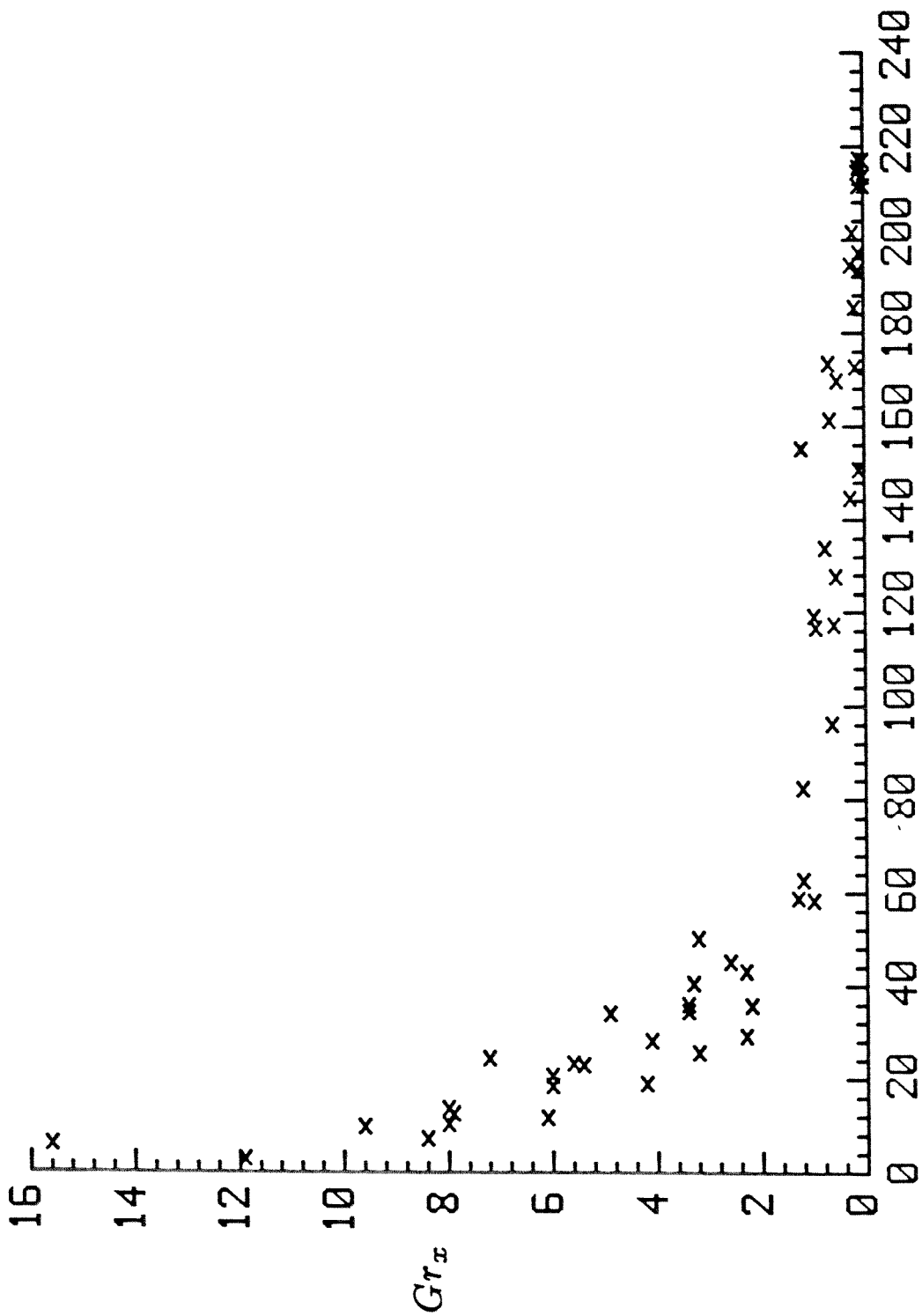

Figure 25 Experimentally observed region of instability, local Grashof and Reynolds numbers of transition.

the jet, ranging from that of a single phase jet to that of a plume. The asymptotic limits where the theoretical flow solutions apply are also in agreement with the experimental conditions, as the jet-like flow occurs at very small values of the parameter Gr_jRe_j, while the plume-like flows occur at larger values of this parameter, where $Gr_jRe_j > 0.1$. In the flows which exhibited mixed plume and jet characteristics (i.e., the jet in the slightly heavier dyed fluid) no quantitative comparisons could be made with the theory. However, the small buoyancy force due to the dye particles was observed to decrease the interfacial spreading rate to zero. This behavior indicates that the jet flow is extremely sensitive to buoyancy effects.

A steady oscillating motion was observed in the jet flows with a significant amount of buoyancy. The oscillations were induced by interaction forces with the side walls of the apparatus, which tended to make the jet lean to one side, and the buoyancy force, which tended to make the jet flow vertically. In the flows of the jet in a dyed fluid, the buoyancy force was not strong enough to cause the jet to flow vertically. Hence, the jet contacted the side wall, where it continued to flow up the column.

The buoyancy force also has a significant effect on the stability of the two-phase flow. In all of our experiments for which $0 < Gr_jRe_j < 1.2$ the flow became unstable at some distance downstream from the nozzle. For those experiments with Gr_jRe_j greater than 1.2, the flow became unstable almost immediately as it exited the nozzle. Hence, the buoyancy force is highly destabilizing, as the corresponding single phase flows of a jet and a plume are

stable below critical Reynolds and Grashof numbers of 21.6 and 6.7, respectively (cf. Garg (1981) and Wakitani (1985)). The destabilizing effect of the buoyancy force on the jet-like flow is evident from Figure 25, where the Reynolds number of transition decreases drastically when a few particles are added to the flow. Although buoyancy is present in both the single phase and two-phase plume-like flows, the latter is less stable because the buoyancy force is constant.

For the single phase flow of a plume above a line source of heat, the buoyancy force, and hence the energy fed to the disturbance flow, is strongest at the origin, and decreases with increasing distance from the source. Thus, if the source is not strong enough, the viscous forces will dissipate the energy fed to the disturbance, and the flow will be stable. However, in the two-phase plume-like flow, the buoyancy force is constant with increasing distance from the nozzle. Since the viscous forces in the suspension cannot dissipate this constant supply of energy, the disturbance grows and the flow is unstable.

Although the lineary theory was unable to successfully predict the inception distances that were observed experimentally, we believe that the discrepancy is due to finite disturbances which were caused by the oscillating motion of the plume. Qualitatively, the theory predicts that increases in the jet Grashof number (i.e., the buoyancy force) and the jet Reynolds number (i.e., the rate at which buoyancy is fed into the flow) are both destabilizing, which is what we observed experimentally.

REFERENCES

Abramowitz, M. and Stegun, I. 1964 Handbook of Mathematical Functions, Dover Publications, Inc., New York, NY.

Acrivos, A., and Herbolzheimer E. 1979 Enhanced sedimentation in settling tanks with inclined walls. J. Fluid Mech., 92, 435-457.

Agarwal, G.P., Hudson, J.L., and Jackson, R. 1980 Fluid mechanical description of fluidized beds. Experimental investigation of convective instabilities in bounded beds. Ind. Eng. Chem. Fund., 19, 59-66.

Anderson, T.B., and Jackson, R. 1967 A fluid mechanical description of fluidized beds. Equations of motion. Ind. Eng. Chem. Fund., 6, 527-539.

Anderson, T.B., and Jackson, R. 1968 Fluid mechanical description of fluidized beds. Stability of the state of uniform fluidization. Ind. Eng. Chem. Fund., 7, 12-21.

Andrade, E.N. da C. 1939 The velocity distribution in a liquid into liquid jet. Part 2: the plane jet. Proc. Phys. Soc. London, 51, 784-793.

Atherton, R.W., and Homsy, G.M. 1973 A note on wave inception in film flow. Chem. Eng. J., 6, 273-275.

Baines, W., and Turner, J. 1969 Turbulent buoyant convection from a source in a confined region. J. Fluid Mech., 37, 51-80.

Benjamin, T.B. 1957 Wave formation in laminar flow down an inclined plane. J. Fluid Mech., 2, 554-574.

Bickley, W.G. 1937 The plane jet. Philos. Mag., 23, 727-731.

Bill, R.G. and Gebhart, B. 1975 The transition of plane plumes. Int. J. Heat Mass Transfer, 18, 513-526.

Bouthier, M. 1973 Stabilite lineaire des ecoulements presque paralleles. Prtie II. La couche limite de Blasius. J. Mec., 12, 75-95.

Brooks, H. and Koh, R. 1965 Discharge of sewage effluent from a line source into a stratified ocean. XI Congr Int. Assoc. for Hydraul. Res., Paper No. 2.19.

Clenshaw, C.W. and Elliott, D. 1960 A numerical treatment of the Orr-Sommerfeld equation in the case of a laminar jet. Quart. J. Mech. Applied Math., 13, 300-313.

Curle, N. 1957 On hydrodynamic stability in unlimited fields of viscous flows. Proc. Roy. Soc. A, 238, 489-501.

Didwania, A.K., and Homsy, G.M. 1982 Resonant sideband instabilities in wave propagation in fluidized beds. J. Fluid Mech., 122, 433-438.

Forstrum, R.J., and Sparrow, E.M. 1967 Experiments on the buoyant plume above a heated horizontal wire. Int. J. Heat Mass Transfer, 10, 321-331.

Fujii, T. 1963 Theory of the steady laminar natural convection above a horizontal line heat source and a point heat source. Int. J. Heat Mass Transfer, 6, 597-606.

Fujii, T., Morioka, I., and Uehara, H. 1973 Buoyant plume above a horizontal line heat source. Int. J. Heat Mass Transfer, 16, 755-768.

Gadala-Maria, F., and Acrivos, A. 1980 Shear-induced structure in a concentrated suspension of solid spheres. J. of Rheology, 24, 799-814.

Garg, V.K. 1981 Spatial stability of the non-parallel Bickley jet. J. Fluid Mech., 102, 127-140.

Gaster, M. 1962 A note on the relation between temporally-increasing and spatially-increasing disturbances in hydrodynamic stability. J. Fluid Mech., 14, 222-224.

Gaster, M. 1974 On the effects of boundary-layer growth on flow stability. J. Fluid Mech., 66, 465-480.

Gebhart, B., Pera, L., and Schorr, A.W. 1970 Steady laminar natural convection plumes above a horizontal line heat source. Int. J. Heat Mass Transfer, 13, 161-171.

Germeles, A. 1975 Forced plumes and mixing of liquids in tanks. J. Fluid. Mech., 71, 601-623.

Haaland, S.E., and Sparrow, E.M. 1973 Stability of buoyant boundary layers and plumes, taking account of nonparallelism of the basic flows. Trans. ASME J. Heat Transfer, 95, 295-301.

Herbolzheimer, E. 1983 Stability of the flow during sedimentation in inclined channels. Phys. Fluids, 26, 2043-2054.

Hieber, C.A., and Nash, E.J. 1975 Natural convection above a line heat source: higher order effects and stability. Int. J. Heat Mass Transfer, 18, 1473-1479.

Hinch, E.J. 1977 An averaged-equation approach to particle interactions in a fluid suspension. J. Fluid Mech., 83, 695-720.

Homsy, G.M., El-Kaissy, M.M., and Didwania, A. 1980 Instability waves and the origin of bubbles in fluidized beds - II. Comparisons with theory. Int. J. Multiphase Flow, 6, 305-318.

Jackson, R. 1963 The mechanics of fluidized beds: Part I: The stability of the state of uniform fluidization. Trans. Inst. Chem. Eng., 41, 13-21.

Koh, R. and Brooks, N. 1975 Fluid Mechanics of waste-water disposal in the ocean. Ann. Rev. Fluid Mech., 7, 187-211.

Kotsovinos, N.E. 1975 A study of the entrainment and turbulence in a plane buoyant jet. PhD thesis, California Institute of Technology, Pasadena, CA.

Kreyszig, E. 1979 Advanced Engineering Mathematics 4th ed., Jogn Wiley and Sons, Inc., New York, NY.

List, E. 1982 Turbulent jets and plumes. Ann. Rev. Fluid Mech., 14, 189-212.

Lynch, E.D. 1985 Sedimentation in quiescent and sheared suspensions. Ph.D. Thesis, California Institute of Technology, Pasadena, CA.

Medlin, J., Wong, H., and Jackson R. 1974 Fluid mechanical description of fluidized beds. Convective instabilities in bounded beds. Ind. Eng. Chem. Fundam., 13, 247-259.

Mih, W.C., and Hoopes, J.A. 1972 Mean and turbulent velocities for a plane jet. J. Hydraul. Div. Proc. ASCE, 98, 1275-1294.

Mollendorf, J.C. and Gebhart, B. 1973a Thermal buoyancy in round laminar vertical jets. Int. J. Heat Mass Transfer, 16, 735-745.

Mollendorf, J.C. and Gebhart, B. 1973b An experimental and numerical study of the viscous stability of a round laminar vertical jet with and without thermal buoyancy for symmetric and asymmetric disturbances. J. Fluid Mech., 61, 367-399.

Morris, P.J. 1981 Stability of a two-dimensional jet. AIAA J., 19, 857-862.

Morton, B., Taylor, G., and Turner, J. 1956 Turbulent gravitational convection from maintained and instantaneous sources. Proc. Roy. Soc. A, 234, 1-23.

Nachtsheim, P.R. 1963 Stability of free convection boundary layer flows. NASA TN D-2089.

Pai, S.I. 1951 On the stability of two-dimensional laminar jet flow of gas. J. Aero. Sci., 18, 731-742.

Pera, L., and Gebhart, B. 1971 On the stability of laminar plumes: some numerical solutions and experiments. Int. J. of Heat Mass Transfer, 14, 975-984.

Pera, L., and Gebhart, B. 1975 Laminar plume interactions. J. Fluid Mech., 68, 259-271.

Plapp, J.E. 1957 The analytic study of laminar boundary stability in free convection. J. Aero. Sci., 24, 318-319.

Ricou, F.P., and Spalding, D.B. 1961 Measurements of entrainment by axisymmetrical turbulent jets. J. Fluid Mech., 11, 21-32.

Sato, H., and Sakao, F., 1964 An experimental investigation of the instability of a two-dimensional jet at low Reynolds numbers. J. Fluid Mech., 20, 337-352.

Savage, S.B., and Chan, G.K.C. 1970 The buoyant two-dimensional laminar vertical jet. Quart. J. Mech. Applied Math., 23, 413-430.

Schlichting, H. 1933 Laminare strahlausbreitung. ZAMM, 13, 260-263.

Schorr, A.W., and Gebhart, B. 1970 An experimental investigation of natural convection wakes above a line heat source. Int. J. Heat Mass Transfer, 13, 557-571.

Schubauer, G.B., and Skramstad, H.K., 1943. Laminary boundary-layer oscillations and transition on a flat plate. N.A.C.A. W-8 ACR.

Smith, F.T. 1979 On the non-parallel flow stability of the Blasius boundary layer. Proc. Roy. Soc. A, 366, 91-109.

Squire, H.B. 1933 On the stability for three-dimensional disturbances of viscous fluid flow between parallel walls. Proc. Roy. Soc. A, 142, 621-628.

Tatsumi, T., and Kakutani, T. 1958 The stability of a two-dimensional jet. J. Fluid Mech., 4, 261-275.

Tollmein, W. 1929 Ueber die Entstehung der Furbulenz. Nachr. Ges. Wiss., Goettingen, Math-Phys. Klasse, 2, 21-44. (Translated by N.A.C.A. Tech. Memo. 609).

Wakitani, S. 1985 Non-parallel flow stability of a two-dimensional buoyant plume. J. Fluid Mech., 159, 241-258.

Yih, C-S. 1952. Laminar free convection due to a line source of heat. Trans. Amer. Geophys. Union, 33, 669-672.

Yih, C-S. 1963 Stability of liquid flow down an inclined plane. Phys. Fluids, 6, 321-334.

APPENDIX A

The Stability of Short Wavelength Disturbances

Let us investigate the stability of the plume-like flow in Case I to small amplitude disturbance waves with wavelengths that are approximately the same as the pure fluid width, i.e.,

$$\ell_x \sim \delta = \frac{\epsilon^2}{Re_j} , \tag{A.1}$$

where ϵ is an asymptotically small parameter (cf. 2.42). Since the effects of the disturbance only penetrate a distance comparable to its wavelength into the suspension, ϕ decays to zero over a very thin region. On this scale, the leading order base flow velocity appears to be uniform, as given by the Taylor series expansion about $\tilde{y} = 0$. In terms of the sublayer variables this is written as

$$U^S = 1 + \frac{\ell_y}{\Delta} U^S_{\tilde{y}}|_o \hat{y} + (\frac{\ell_y}{\Delta})^2 \frac{1}{2} U^S_{\tilde{y}\tilde{y}}|_o \hat{y}^2 + \cdots \quad .$$

The sublayer thickness can not be larger than the wavelength of the disturbance, hence, $\ell_y = \delta$, which implies that $\hat{y} = \bar{y}$. The leading order pure fluid velocity is also equal to unity (cf. 2.24), and hence the leading order equations for the pure fluid and suspension streamfunctions are identical

$$(\psi'' - \alpha^2\psi)'' + [iR(\omega-\alpha) - \alpha^2](\psi'' - \alpha^2\psi) =$$

$$- \varepsilon i\alpha R\left[b^3(\frac{1}{2}\bar{y}^2 + \bar{y})(\psi'' - \alpha^2\psi) + \overline{U_{\bar{y}\bar{y}}}\psi\right] + O(\varepsilon^2) , \tag{A.2a}$$

and

$$(\phi'' - \alpha^2\phi)'' + [iR(\omega-\alpha) - \alpha^2](\phi'' - \alpha^2\phi) =$$

$$- \varepsilon i\alpha R\, U^S_{\tilde{y}}|_O\, \bar{y}\, (\phi'' - \alpha^2\phi) + O(\varepsilon^2) , \tag{A.2b}$$

where the dilute limit has been taken so that $\rho_O = \mu_O = 1$. The boundary conditions are

$$\psi'(-1) = \psi'''(-1) = 0 , \tag{A.3a}$$

or

$$\psi(-1) = \psi''(-1) = 0 , \tag{A.3b}$$

with

$$\phi, \phi' \to 0 \qquad \text{as } y \to \infty , \tag{A.3c}$$

$$\psi(0) = \phi(0) = 1 , \tag{A.3d}$$

$$\psi'(0) = \phi'(0) , \tag{A.3e}$$

$$\psi'''(0) = \phi'''(0) , \tag{A.3f}$$

and

$$(\frac{\omega}{\alpha} -1)\psi''(0) + \varepsilon\, \overline{U_{\bar{y}\bar{y}}}|_o = (\frac{\omega}{\alpha} -1)\phi''(0) + \varepsilon^2\, U^s_{\bar{y}\bar{y}}|_o \ . \qquad (A.3g)$$

Note that in the tangential stress condition (A.3g), the term through which energy is transferred from the base flow to the disturbance flow, i.e., U_{yy}, is of a size $O(\varepsilon)$ and hence does not appear in the leading order balance.

The general solutions for the leading order streamfunctions have the form

$$\psi,\phi \sim e^{-\alpha\bar{y}} + e^{\alpha\bar{y}} + e^{-\theta\bar{y}} + e^{\theta\bar{y}} \ ,$$

where

$$\theta^2 = \alpha^2 - iR(\omega-\alpha) \ ,$$

and the solutions for ψ and ϕ differ only in the integration constants. However, upon substituting these solutions into the boundary conditions, we find that the only nontrivial solution occurs when

$$(\omega-\alpha) = \frac{1}{iR}\,(\alpha^2 - \theta^2) = 0 \ .$$

Hence, to leading order the disturbance wave speed is equal to the base flow interfacial velocity, as is the case for the longer waves.

Setting $(\omega-\alpha) = \varepsilon(\overline{\omega-\alpha})$, and $\overline{U_{\bar{y}\bar{y}}} = b^3$, where the terms with the overbar term are $O(1)$, the rescaled equations are

$$\psi^{iv} - 2\alpha^2\psi'' + \alpha^4\psi = -\varepsilon iR\left[(\overline{\omega-\alpha}) + b^3(\frac{1}{2}\bar{y}^2 + \bar{y})(\psi''-\alpha^2\psi) - b^3\psi\right] + O(\varepsilon^2) , \quad (A.4a)$$

and

$$\phi^{iv} - 2\alpha^2\phi + \alpha^4\phi = -\varepsilon iR\left[(\overline{\omega-\alpha}) + b^3\bar{y}(\phi''-\alpha^2\phi)\right] + O(\varepsilon^2) . \quad (A.4b)$$

The general solution to these equations is of the form

$$\psi = (A_0 + A_2\bar{y})e^{-\alpha\bar{y}} + (A_1 + A_3\bar{y})e^{\alpha\bar{y}} + \varepsilon\bar{\psi}_p(\bar{y}) , \quad (A.5a)$$

and

$$\phi = (B_0 + B_2\bar{y})e^{-\alpha\bar{y}} + (B_1 + B_3\bar{y})e^{\alpha\bar{y}} + \varepsilon\bar{\phi}_p(\bar{y}) , \quad (A.5b)$$

where $\bar{\psi}_p$ and $\bar{\phi}_p$ are the rescaled particular solutions to (A.4). In order that the disturbance in the suspension is confined to the sublayer, both B_1 and B_3 must vanish. Applying the centerline conditions for antisymmetric disturbances, in addition to the conditions in (A.3d - 3f), gives the remaining integration constants for the homogeneous solution

$$A_0 = 1 - \varepsilon \frac{1}{4\alpha^3}\Delta_3 , \quad (A.6a)$$

$$A_1 = \varepsilon \frac{1}{4\alpha^3}\Delta_3 , \quad (A.6b)$$

$$A_2 = \frac{1}{2} - \varepsilon \frac{1+e^{-2\alpha}}{8\alpha^3}\Delta_3 - \varepsilon \frac{e^{-\alpha}}{4\alpha^3}\left[(\alpha-1)\bar{\psi}_p'''(-1) + \alpha^3(3-\alpha)\bar{\psi}_p'(-1)\right] , \quad (A.6c)$$

$$A_3 = -\frac{e^{2\alpha}}{2} + \varepsilon \frac{1+e^{2\alpha}}{8\alpha^3}\Delta_3 - \varepsilon \frac{e^{\alpha}}{4\alpha^3}\left[(\alpha+1)\bar{\psi}_p'''(-1) - \alpha^2(3+\alpha)\bar{\psi}_p'(-1)\right] , \quad (A.6d)$$

$$B_0 = 1 , \quad (A.6e)$$

$$\begin{aligned} B_2 = -\frac{1}{2}(e^{2\alpha} - 1) + \varepsilon \frac{1}{8\alpha^3}\Big[& (e^{2\alpha} - e^{-2\alpha} + 4\alpha)\Delta_3 \\ & - 2\alpha(e^{\alpha} + e^{-\alpha})\{\bar{\psi}_p'''(-1) - \alpha^2\bar{\psi}_p'(-1)\} \\ & - 2(e^{\alpha} - e^{-\alpha})\{\bar{\psi}_p'''(-1) - 3\alpha^2\bar{\psi}_p'(-1)\}\Big] , \end{aligned} \quad (A.6f)$$

where

$$\Delta_3 \equiv \bar{\psi}_p'''(0) - \bar{\phi}_p'''(0) . \quad (A.6g)$$

The remaining boundary condition which must be satisfied is the shear stress balance. Since the disturbance stream functions in both the pure fluid and suspension are completely specified, this condition determines the eigenvalue α as a function of ω. Expanding the eigenvalue in the form

$$\alpha = \alpha_0[1 + \alpha_1 + \alpha_2 + \ldots] = \omega[1 + \varepsilon\tilde{\alpha}_1 + \alpha_2 + \ldots] , \quad (A.7)$$

gives the eigenvalue condition

$$\tilde{\alpha}_1 + \frac{1}{\varepsilon}\alpha_2 = \frac{b^3}{2\omega e^{2\omega}} + \varepsilon \frac{U^S_{\bar{y}\bar{y}}|_0}{2\omega e^{2\omega}} - \varepsilon \frac{b^3}{4\omega^4 e^{4\omega}} [(\frac{1+e^{2\omega}}{2} + \omega)\Delta_3$$

$$+ \omega^2\{\bar{\psi}_p''(0) - \bar{\phi}_p''(0)\} - e^{\omega}\{(\omega+1)\bar{\psi}_p'''(-1) - \omega^2(3+\omega)\bar{\psi}_p'(-1)\}] + O(\varepsilon^2) . \tag{A.8}$$

Hence the first correction to the wavenumber, i.e.,

$$\alpha_1 = \varepsilon \frac{b^3}{2\omega e^{2\omega}} \tag{A.9}$$

is real and gives a slight correction to the wave speed. However, we still have no information as to whether these short waves grow or decay.

At the next order, the inertial terms of the differential equations governing the disturbance flow in both regions are important. The particular solutions are of the form

$$\bar{\psi}_p = iR[pe^{-\alpha\bar{y}} + qe^{\alpha\bar{y}}] , \tag{A.10a}$$

and

$$\bar{\phi}_p = iR\, re^{-\alpha\bar{y}} , \tag{A.10b}$$

where p,q, and r are polynomial functions of $\bar{y}$. Substituting (A.10) and the homogeneous solutions for ψ and ϕ (cf. A.5) into the governing equations (A.4) gives these polynomials as

$$p(\bar{y}) = \frac{b^3 A_2}{48}\,\bar{y}^4 + \frac{(3+2\omega)b^3 A_2}{24\omega}\,\bar{y}^3$$

$$+ \frac{b^3}{8\omega^2}\,\bar{y}^2\left[\left(\frac{5}{2} + 2\omega\right)A_2 + \omega A_0 + \frac{2\omega}{b^3}(\omega-\alpha)A_2\right], \tag{A.10c}$$

$$q(\bar{y}) = -\frac{b^3 A_3}{48}\,\bar{y}^4 + \frac{(3-2\omega)b^3 A_2}{24\omega}\,\bar{y}^3$$

$$+ \frac{b^3}{8\omega^2}\,\bar{y}^2\left[\left(-\frac{5}{2} + 2\omega\right)A_3 + \omega A_1 - \frac{2\omega}{b^3}(\omega-\alpha)A_3\right], \tag{A.10d}$$

and

$$r(\bar{y}) = \frac{b^3 B_2}{12}\,\bar{y}^3 + \frac{b^3 B_2}{4\omega}\,\bar{y}^2\left[1 + \frac{1}{b^3}(\omega-\alpha)\right], \tag{A.10e}$$

where the integration constants are given in (A.6). Taking the appropriate derivatives of the particular solution and substituting them into the tangential stress condition (A.8) gives the second correction to the eigenvalue, which is complex

$$\alpha_2 = \varepsilon^2\,\frac{U^S_{\tilde{y}\tilde{y}}|_o}{2\omega e^{2\omega}} - \varepsilon^2\, i\,\frac{b^6 Re_j}{8\omega^4}\left[1 - \frac{9}{16\omega}\,(1-e^{-4\omega}) + \frac{5}{4}\,e^{-4\omega}\right.$$

$$\left. - \frac{\omega}{2}\,(e^{-2\omega} - 2e^{-4\omega}) + \frac{2}{3}\,\omega^3 e^{-2\omega} + \frac{\omega+2\omega^2}{2}\,e^{-4\omega}\right]. \tag{A.11a}$$

The imaginary part of α_2 is always negative, and hence, all antisymmetric disturbances with wavelengths on the same order as the pure fluid thickness grow. As the frequency increases, corresponding to shorter waves, the amplification factor goes to zero like

$$\alpha_I \sim -\varepsilon^2 \frac{b^6 Re_j}{8\omega^3} \qquad \text{as } \omega \to \infty \,. \tag{A.11b}$$

In the limit of longer wavelengths, the imaginary part of α asymptotes to

$$\alpha_I \sim -\varepsilon^2 \frac{b^6 Re_j}{16\omega^2} \qquad \text{as } \omega \to 0 \,. \tag{A.11c}$$

The analysis for symmetric disturbances follows that for the antisymmetric disturbances, the only difference being the boundary condition at the centerline. Hence applying the centerline condition (A.3b) as well as the conditions in (A.3d - 3f) gives the integration constants for the homogeneous solution

$$A_0 = 1 - \varepsilon \frac{1}{4\alpha^3}\Delta_3 \,, \tag{A.12a}$$

$$A_1 = \varepsilon \frac{1}{4\alpha^3}\Delta_3 \,, \tag{A.12b}$$

$$A_2 = \frac{1}{2} - \varepsilon \frac{1-e^{-2\alpha}}{8\alpha^3}\Delta_3 + \varepsilon \frac{e^{-\alpha}}{4\alpha}\left[\bar{\psi}_p''(-1) + \alpha(2-\alpha)\bar{\psi}_p(-1)\right] \,, \tag{A.12c}$$

$$A_3 = \frac{e^{2\alpha}}{2} + \varepsilon \frac{1 - e^{2\alpha}}{8\alpha^3}\Delta_3 - \varepsilon \frac{e^{\alpha}}{4\alpha}\left[\bar{\psi}_p''(-1) - \alpha(2+\alpha)\bar{\psi}_p(-1)\right] \,, \tag{A.12d}$$

$$B_0 = 1 \,, \tag{A.12e}$$

and

$$B_2 = \frac{1}{2}(e^{2\alpha} + 1) + \varepsilon \frac{1}{8\alpha^3}[(e^{-2\alpha} - e^{2\alpha} + 4\alpha)\Delta_3$$

$$+ 2\alpha^2(e^{-\alpha} - e^{\alpha}) \{\bar{\psi}_p''(-1) - \alpha^2\bar{\psi}_p(-1)\} + 4\alpha^3(e^{\alpha} + e^{-\alpha})\bar{\psi}_p(-1)] . \tag{A.12f}$$

Since the governing differential equations for the symmetric and antisymmetric disturbances are identical, the particular solutions for the streamfunctions in the pure fluid and suspension are of the same form as those in (A.10). The difference between the antisymmetric and symmetric solutions is, of course, in the integration constants for the homogeneous solution (cf. A.6 and A.12).

Substituting the solutions for ψ and ϕ into (A.3g) gives the wavenumber-frequency relationship

$$\tilde{\alpha}_1 + \frac{1}{\varepsilon}\alpha_2 = -\frac{b^3}{2\omega e^{2\omega}} - \varepsilon \frac{U^S_{\tilde{y}\tilde{y}}|_o}{2\omega e^{2\omega}} - \varepsilon\, i\frac{b^6 Re_j}{8\omega^4}\left[1 - \frac{9}{16\omega}(1-e^{-4\omega})\right.$$

$$\left. + \frac{5}{4}e^{-4\omega} + \frac{\omega}{2}(e^{-2\omega} + 2e^{-4\omega}) - \frac{2}{3}\omega^3 e^{-2\omega} + \frac{\omega+2\omega^2}{2}e^{-4\omega}\right] . \tag{A.13}$$

Thus the first correction to the eigenvalue is real and is given by

$$\alpha_1 = -\varepsilon \frac{b^3}{2\omega e^{2\omega}} . \tag{A.14}$$

However, the second correction is complex and the imaginary component is always negative. Hence, all short wavelength symmetric disturbances will grow. In the limit of very short wavelengths, the amplification factor for the symmetric disturbances decreases to zero in the same way as for the antisymmetric disturbances (cf.

A.11b), i.e.,

$$\alpha_I \sim -\varepsilon^2 \frac{b^6 Re_j}{8\omega^3} \quad \text{as } \omega \to \infty . \tag{A.15a}$$

However, in the limit of large wavelengths, the symmetric disturbance is less stable than the antisymmetric disturbances (cf. A.11c)

$$\alpha_I \sim -\varepsilon^2 \frac{3b^6 Re_j}{16\omega^2} \quad \text{as } \omega \to 0 . \tag{A.15b}$$

APPENDIX B

The Asymptotic Matching of the Short and Long Wavelength Stability Solutions

In order to check the results of the numerical solutions in the long wavelength analysis, the eigenvalues are asymptotically matched to those from the short wavelength analysis. This requires expanding and solving the eigenvalue conditions in (3.35) and (3.37) (for the antisymmetric and symmetric disturbances, respectively) in the limit as $\omega \to \infty$. The solutions are then matched to the corresponding eigenvalues from the short wavelength analysis, which are evaluated in the limit as $\omega \to 0$.

The small frequency asymptotic behavior of the eigenvalues from the short wave analysis is given by

$$\lim_{\omega\to 0} \alpha_S = \omega_S + \varepsilon \frac{b^3}{2} + \varepsilon^2\left(\frac{1}{2}U^S_{\tilde{y}\tilde{y}}\Big|_o - i\frac{b^6 Re_j}{16\omega_S^2}\right) , \qquad \text{(B.1a)}$$

and

$$\lim_{\omega\to 0} \alpha_S = \omega_S - \varepsilon \frac{b^3}{2} + \varepsilon^2\left(-\frac{1}{2}U^S_{\tilde{y}\tilde{y}}\Big|_o - i\frac{3b^6 Re_j}{16\omega_S^2}\right) , \qquad \text{(B.1b)}$$

(cf. A.11 and A.15), where the subscript s refers to the short wavelength variables. In the above and the rest of this appendix, we shall present the antisymmetric and symmetric results simultaneously, using equation labels a and b to differentiate between the two. Thus (B.1a) represents the small frequency

asymptotic behavior of the antisymmetric eigenvalue from the short wavelength analysis. Similarly, (B.1b) represents the small frequency behavior of the symmetric eigenvalue. In order that the eigenvalues from the long and short wavelength analyses can be compared in the same set of variables, we rewrite the short wavelength wavenumber and frequency in terms of the corresponding long wavelength variables, i.e.,

$$\omega_S = \left(\frac{\varepsilon Re_j}{\nu_o}\right)^{1/2} \omega \ ,$$

and

$$\alpha_S = \left(\frac{\varepsilon Re_j}{\nu_o}\right)^{1/2} \alpha \ ,$$

which gives

$$\alpha = \omega + \left(\nu_o \frac{\varepsilon}{Re_j}\right)^{1/2} b^3\left(\frac{1}{2} - i\frac{b^3}{16\omega^2}\right) + \ldots + O(\varepsilon^3/Re_j)^{1/2} \ , \qquad (B.2a)$$

and

$$\alpha = \omega + \left(\nu_o \frac{\varepsilon}{Re_j}\right)^{1/2} b^3\left(-\frac{1}{2} - i\frac{3b^3}{16\omega^2}\right) + \ldots + O\left(\frac{\varepsilon^3}{Re_j}\right)^{1/2} \ . \qquad (B.2b)$$

These expressions are simplified by writing them in terms of the reduced variables s and β (cf. 3.43a and 3.44) to give

$$\beta = \frac{1}{2} + \frac{1}{16s^3} \ , \qquad (B.3a)$$

and

$$\beta = -\frac{1}{2} + \frac{3}{16s^3} . \qquad \text{(B.3b)}$$

The eigenvalues from the short wavelength analyses must match the solutions of the long wavelength eigenvalue conditions, which are evaluated in the limit of large frequencies, i.e., we must solve

$$(\beta-1)Ai'(z_o) - s^2 f(s,z_o) = 0 , \qquad \text{(B.4a)}$$

and

$$\beta Ai(z_o) + sf(s,z_o) = 0 , \qquad \text{(B.4b)}$$

where

$$f(s;z_o) = e^{(\frac{2}{3}s^3-\beta)} \left[\frac{1}{3} - \int_0^{z_o} Ai(t)\, dt + Ai(z_o)\int_0^s m\, e^{(\frac{m^3}{3}-mz_o)}\, dm \right. \qquad \text{(B.5)}$$

$$\left. + Ai'(z_o)\int_0^s e^{(\frac{m^3}{3}-mz_o)}\, dm \right] ,$$

in the limit as $\omega \to \infty$, (i.e., $s, z_o \to \infty$). Hence, the asymptotic behaviors of the Airy function and its derivative are required. These are given by Abramowitz and Stegun (1964), where for large $|z|$

$$Ai(z) \sim \frac{1}{2}\pi^{-1/2} z^{-1/4} e^{-\zeta} \sum_{k=0}^{\infty} (-1)^k c_k \zeta^{-k} \qquad |\arg z| < \pi ,$$

and

$$\mathrm{Ai}'(z) \sim -\frac{1}{2}\pi^{-1/2} z^{1/4} e^{-\zeta} \sum_{k=0}^{\infty} (-1)^k d_k \zeta^{-k} \qquad |\arg z| < \pi ,$$

where

$$\zeta = \frac{2}{3} z^{3/2} ,$$

$$c_0 = d_0 = 1 ,$$

$$\left.\begin{aligned} c_k &= \frac{\Gamma(3k+\frac{1}{2})}{\Gamma(k+\frac{1}{2})\, 54^k\, k!} , \\ d_k &= -\frac{6k+1}{6k-1} c_k . \end{aligned}\right\} \quad k=1,2,3, \ldots$$

Dividing the two power series, and expanding the coefficients of the resulting sum gives

$$\mathrm{Ai}(z_0) = -\frac{1}{s}\mathrm{Ai}'(z_0)\left[1 + \frac{1}{2s^3}(\beta - \frac{1}{2}) + O(s^{-6})\right] . \qquad (B.6)$$

The major difficulty in expanding the eigenvalue conditions in (B.4) for large $|z|$ occurs in evaluating the integrals in $f(s,z_0)$. The integral of the Airy function is evaluated using the Airy equation to substitute for Ai(t) and integrating by parts to give

$$\int_{z_0}^{\infty} \mathrm{Ai}(t)\, dt = -\frac{1}{z_0}\mathrm{Ai}'(z_0) - \frac{1}{z_0^2}\mathrm{Ai}(z_0) + 2\int_{z_0}^{\infty} \frac{1}{t^3}\, \mathrm{Ai}(t)\, dt .$$

The last term can be repeatedly integrated by parts, and is expressed in terms of the recurrence relation

$$\int_{z_o}^{\infty} \frac{1}{t^k} \, Ai(t) \, dt = - \frac{Ai'(z_o)}{z_o^{k+1}} - \frac{(k+1)Ai(z_o)}{z_o^{k+2}}$$

$$+ (k+1)(k+2) \int_{z_o}^{\infty} \frac{1}{t^{k+3}} \, Ai(t) \, dt \, .$$

Hence, the integral of the Airy function is written as

$$\int_{z_o}^{\infty} Ai(t) \, dt = - \frac{Ai'(z_o)}{z_o} \left[1 + \frac{2}{z_o^3} + \frac{40}{z_o^6} + \ldots \right]$$

$$- \frac{Ai(z_o)}{z_o^2} \left[1 + \frac{8}{z_o^3} + \frac{280}{z_o^6} + \ldots \right] . \qquad (B.7)$$

In order to evaluate the behavior of the exponential integrals in (B.5) at large values of s, a saddle point method was used. We shall first examine the asymptotic behavior of the integral,

$$I = \int_0^s e^{(\frac{m^3}{3} - m z_o)} \, dm \, . \qquad (B.8)$$

This is rewritten using the new variables

$$t = \frac{m}{s} \quad , \quad sz_o = s^3 - \beta \quad , \quad \text{and} \quad s^3 = i\gamma^{-2} \, , \tag{B.9}$$

to give

$$I = s \int_0^1 e^{\beta t} \, e^{-i\gamma^{-2}(t-\frac{t^3}{3})} \, dt \, .$$

This integral is broken up into two parts, where the path of integration is chosen so that the integrand decreases rapidly away from the endpoints 0, and 1, i.e.,

$$I = I_1 + I_2 \, ,$$

where

$$I_1 = s \int_0^a e^{\beta t} \, e^{-i\gamma^{-2}(t-\frac{t^3}{3})} \, dt \, , \tag{B.10}$$

and

$$I_2 = s \int_a^1 e^{\beta t} \, e^{-i\gamma^{-2}(t-\frac{t^3}{3})} \, dt \, . \tag{B.11}$$

We shall first evaluate the integral I_1. We determine the integration path by defining the variable $r = -\frac{1}{i} \gamma^{-2} t$, so that the integrand decays exponentially away from the origin. Then since the integrand is very small at the other limit of integration, we may let $a \to \infty$ to give

$$I_1 = - is\gamma^2 \int_0^\infty e^{-r}\, e^{-(i\beta\gamma^2 r + \gamma^4 \frac{r^3}{3})}\, dr \ . \qquad (B.12)$$

The second exponential function in the integrand may be expanded about $r = 0$, and integrating the resulting series term by term gives

$$I_1 = - is\gamma^2 [1 - i\beta\gamma^2 - \beta^2\gamma^4 - 2\gamma^4 + O(\beta\gamma^6)] \qquad (B.13)$$

where from (B.9), $\gamma \sim O(s^{-3/2})$ and hence is small for large s.

The integral I_2 is evaluated by redefining the variable $t = n+1$ to give

$$I_2 = - s\, e^{(\beta - \frac{2}{3} i\gamma^{-2})} \int_0^{a-1} e^{\beta n}\, e^{i\gamma^{-2} n^2 (1 + \frac{n}{3})}\, dn \ . \qquad (B.14)$$

As in the previous case for I_1, we define a new variable $re^{i\theta} = n/\gamma$ so that the integrand decreases exponentially away from the origin. This requires θ to be chosen such that

$$ie^{2\theta} = - 1 \ ,$$

and hence the solution is $\theta = - 3\pi/4$. Thus we set $n = \gamma A r$ where $A = e^{-i3\pi/4} = \sqrt{i}$, and since the integrand is approximately zero away from the origin, we extend the other integration limit to infinity to give

$$I_2 = - A\gamma s e^{(\beta - \frac{2}{3} i\gamma^{-2})} \int_0^\infty e^{-r^2} e^{A\gamma(\beta r - \frac{r^3}{3})} \, dr \, . \qquad (B.15)$$

Expanding the second exponential function in the integrand about the origin and integrating term by term gives,

$$I_2 = -A\gamma s e^{(\beta - \frac{2}{3} i\gamma^{-2})} \left[\frac{\pi^{1/2}}{2} + \frac{1}{2} A\gamma(\beta - \frac{1}{3}) + \frac{\pi^{1/2}}{2} (\alpha\gamma)^2 (\frac{1}{4}\beta^2 - \frac{1}{4}\beta + \frac{5}{48}) \right. \qquad (B.16)$$

$$\left. + \frac{1}{6}(A\gamma)^3 (\frac{1}{2}\beta^3 - \beta^2 + \beta - \frac{4}{9}) + O(\gamma^4) \right] .$$

The procedure for evaluating the other exponential integral in f (cf. B.5), i.e.,

$$J = \int_0^s m e^{(\frac{m^3}{3} - m z_o)} \, dm \, ,$$

follows the identical steps used to evaluate I. Hence the analogous integral of I_1 in (B.12), i.e.,

$$J_1 = -s^2\gamma^4 \int_0^\infty r e^{-r} \, e^{-(i\beta\gamma^2 r + \gamma^4 \frac{r^3}{3})} dr \, ,$$

is evaluated to give

$$J_1 = -s^2\gamma^4 \left[1 - 2i\beta\gamma^2 + O(\gamma^4) \right] . \qquad (B.17)$$

Similarly, the analogous integral of I_2 in (B.15) is

$$J_2 = -s^2 A\gamma \, e^{(\beta - \frac{2}{3}i\gamma^{-2})} \int_0^\infty (1+A\gamma r) e^{-r^2} \, e^{A\gamma(\beta r - \frac{r^3}{3})} \, dr \, .$$

This is evaluated in the same way as I_2 and gives

$$J_2 = -s^2 A\gamma e^{(\beta - \frac{2}{3}i\gamma^{-2})} \left[\frac{\pi^{1/2}}{2} + A\gamma(\frac{1}{2}\beta + \frac{1}{3}) + \frac{\pi^{1/2}}{8} A^2\gamma^2(\beta^2 + \beta - \frac{7}{12}) \right. \tag{B.18}$$

$$\left. + \frac{1}{6} A^3\gamma^3(\frac{1}{2}\beta^3 - \frac{1}{2}\beta^2 - \beta - \frac{5}{9}) + O(\gamma^4) \right] .$$

The results from (B.6), (B.13), and (B.16 - 18) are then substituted into (B.5) and (B.4) and the conditions simplify to

$$\beta = \frac{1}{2} + \frac{1}{16s^3} \, , \tag{B.19a}$$

and

$$\beta = -\frac{1}{2} + \frac{3}{16s^3} \, . \tag{B.19b}$$

A comparison of (B.19) with the expressions in (B.3) confirms that both antisymmetric and symmetric eigenvalues match, and hence the long and short wavelength analyses are consistent.

APPENDIX C

Table 4

Summary of the Linear Regression Analyses of ℓn y vs. ℓn x Plots with Slope m and Correlation Coefficient r

Gr_jRe_j	m	r
0.017	-0.182	0.991
0.035	-0.273	0.967
0.042	-0.220	0.985
0.062	-0.225	0.997
0.068	-0.181	0.988
0.083	-0.208	0.994
0.097	-0.198	0.992
0.101	-0.187	0.990
0.114	-0.200	0.991
0.143	-0.222	0.987
0.230	-0.221	0.996
0.243	-0.280	0.974
0.460	-0.221	0.993